Atomic Scale STEM/EELS and First Principles

Studies of Oxide – Semiconductor Interfaces

BY

QIAO QIAO
B.S., Nanjing Univerisity, 2006
M.S., University of Illinois at Chicago, 2009

THESIS

Submitted as partial fulfillment of the requirements
for the degree of Doctor of Philosophy in Physics
in the Graduate College of the
University of Illinois at Chicago, 2013

Chicago, Illinois

Defense Committee:

Robert F Klie, Chair and Advisor
Serdar Ogut
Andreas W Schroeder
Christoph Grein
Zheng Yang, Eletrical and Computer Engineering

This thesis is dedicated to my parents and grandparents for their support and love.

Acknowledgement

First and foremost I would like to thank my Ph.D. advisor, Dr. Robert F Klie, for his continuous guidance, patience, and encouragement during my graduate studies. Dr. Klie not only showed me how fascinating the microscopy and spectroscopy can be, but also taught me how to be persistent in science and think independently. He supported me to attend many conferences, where I had opportunities to practice public speaking and discover new research perspectives. I can never overstate my gratitude to my co-advisor, Dr. Serdar Ogut, who also taught me quantum mechanics and solid state physics in my first and second year. Dr. Ogut is the most knowledgeable and inspiring theoretical physicist that I know, who gives excellent lectures and does state of the art theoretical condensed matter physics research. It was a great pleasure to work with him, since I not only reaped valuable advises but also joyful conversations. I am also grateful to my thesis committee: Dr. Andreas W Schroeder, Dr. Christoph Grein, and Dr. Zheng Yang, for their insightful comments and questions.

This work could never be done without the help from Dr. Alan W Nicholls, who kept the research resources center to be a highly efficient facility. The cautiousness I learned from Alan would greatly benefit me in my future research. I will forever be grateful to Dr. Kebin Low, who trained me on every piece of instrument in the lab and provided professional assistance. Kebin is also a faithful friend of mine, who shared his experience with me when I was in struggle.

I would also thank everyone in the nanoscale physics group: Runzhe Tao, thank you for being the best and funniest office mate, you made my life colorful; Canhui Wang and Zhao Guo, thank you for all the happiness you shared with me, those are unforgettable

memories; Ahmet Gulec, Tadas Paulauskas, and Patrick J Phillips, thank you for your company and help, you made it fun to work in the group. Last but not least, I would like to thank the physics department and every professor who taught me and talked to me, for their advises and encouragements.

TABLE OF CONTENTS

LIST OF FIGURES

CHAPTER 1

PEROVSKITE OXIDE – COMPOUND SEMICONDUCTOR INTERFACES

1.1 Introduction

The semiconductor research has greatly benefited the present information technology in an extensive scale. The scaling of silicon-based devices has increased the density of transistors on a microchip, increased the speed of operation and has lowered the operating voltage. Compound semiconductors, RF power amplifiers and laser diodes are essential for the improvement of devices such as cellular products and home entertainment systems. While the semiconductor industry has been responsible for much of the world's extraordinary economic expansion over the past fifty years, the industry is facing major challenges in continuing to scale silicon-based devices because of inherent material limitations, such as the breakdown of the gate dielectric and degraded channel mobility. In addition, there is a need to add more functionality to the basic complementary metal–oxide–semiconductor (CMOS) devices for a "more-than-Moore" approach to device scaling to address the future limitations for Moore's law. The recent introduction of high-k dielectrics to Si processing appears to be a short-term solution to solve the gate leakage issue due to undesired tunneling in thin layers of conventional SiO_2 gate dielectric.

Compound semiconductors are being considered not only as the material basis for novel device architectures and structures, but also as a replacement for the silicon channel

itself. Because of their low electron effective mass, compound semiconductors have electron mobilities and velocities that are much greater than silicon. A successful incorporation of III-V materials onto silicon can also result in the integration of new functionalities with silicon devices, such as high speed optoelectronic and communication platforms on the same chip. However, the implementation of III-V semiconductors as the channel in silicon CMOS devices faces many hurdles that are being actively investigated. Among the hurdles for such integration is the development of a gate dielectric on III-V semiconductors that can unpin the Fermi level needed for enhancement-mode operation. Various amorphous oxides deposited by atomic layer deposition (ALD) are being explored.

Currently, oxides are being explored as gate dielectrics for III-V semiconductors similar to those currently used in Si CMOS devices. A unique dual oxide layer $Ga_2O_3/GaGdO_3$ has been developed by the Droopad et al. using molecular beam epitaxy (MBE) that successfully led to the fabrication of enhancement mode GaAs-based metal-oxide semiconductor field-effect transistors (MOSFET) devices [1, 2]. MBE deposition processes are ideal for further development of a crystalline oxide films that, in addition to being used as a gate dielectric, can also be exploited for additional functionalities such as ferroelectricity, ferromagnetism, piezoelectricity and pyroelectricity.

These properties – not found in silicon-based devices – are important for applications such as non-volatile memory, sensors or room temperature tunable dielectrics for RF devices and filters. For instance, the use of a ferroelectric layer as the gate dielectric on a compound semiconductor could lead to a one-transistor, non-volatile memory element. In addition, it has been predicted that inclusion of a thin ferroelectric layer as part of a gate

dielectric stack in a MOSFET device can reduce the subthreshold slope below 60 mV/decade [3]. Thus it is an intriguing and promising concept to utilize epitaxial oxides in monolithically integrated hybrid oxide/compound semiconductor systems. These systems present an ideal platform to explore the synthesis of a set of materials with diverse properties and investigate the growth processes involved during their heterointegration. The integration of oxides with compound semiconductors can potentially have far reaching technological applications in advanced electronics, memories, sensors, persistent surveillance and radar technologies. The development of oxide based multilayers involving ferroelectric and ferromagnetic properties on compound semiconductors would open up novel device applications that utilize the coupling between the ferroelectric and ferromagnetic properties of the structure [4]. This, in combination with the high mobility and optical properties of compound semiconductors oxide heterostructures, would create a potential for new device architectures. New physical phenomena emerge when interfaces between different oxides are created with atomic-scale precision [5] as afforded by the MBE deposition technique.

The aim of this thesis is to develop an atomic-scale understanding of hybrid multifunctional oxide-compound semiconductor systems, based on exploring the synthesis, interfaces, atomic structure and material properties of these heterostructures. The effect of the crystal and interface structures on the electrical and magnetic properties of the compound semiconductors will also be explored. In addition, controlling the ferroic response of the thin oxide films will be investigated through the growth of multilayer test structures, atomic-resolution imaging and spectroscopy, as well as first-principles materials modeling. Unexpected discoveries, such as the 2-d electron gas in the

interface between oxides such as $LaAlO_3$(LAO)/$SrTiO_3$(STO) [6] have led to reports of magnetism and superconductivity in these interfaces that can now be considered for integration with semiconductor logic and optoelectronic devices.

It is, therefore, of crucial importance to develop an atomic-scale understanding of the structure-property relationships of the semiconductor-oxide heterointerface using first-principles modeling combined with state-of-the-art analytical transmission electron microscopy.

1.2 Background

The study of epitaxial, crystalline oxides on semiconductors has been ongoing for many decades [7-12], and the ability to control the crystallinity of the thin film is essential for achieving lower defect density and better electronic properties than amorphous oxides [12-15]. While the primary motivation for oxides on GaAs has been the development of a gate dielectric for GaAs-based MOSFETs [16], hetero-epitaxy of crystalline oxides on III–Vs also provides new opportunities for integration of various functional oxides with III–Vs. Among all the oxides, $SrTiO_3$ (STO) is arguably the best-understood material, which exhibits a wide range of properties and can be used as a substrate for growing various functional oxides [17-23]. In 1998, the first successful growth of epitaxial STO on Si using MBE was reported, as shown in Figure 1.1 [8]. It has shown desirable interfacial structural and electronic properties [24, 25] that have yet to be replicated by any other deposition technique. Epitaxial STO on Si was also used as a virtual substrate for the integration of various functional oxides such as PZT and the multiferroic $BiFeO_3$ with Si [26, 27].

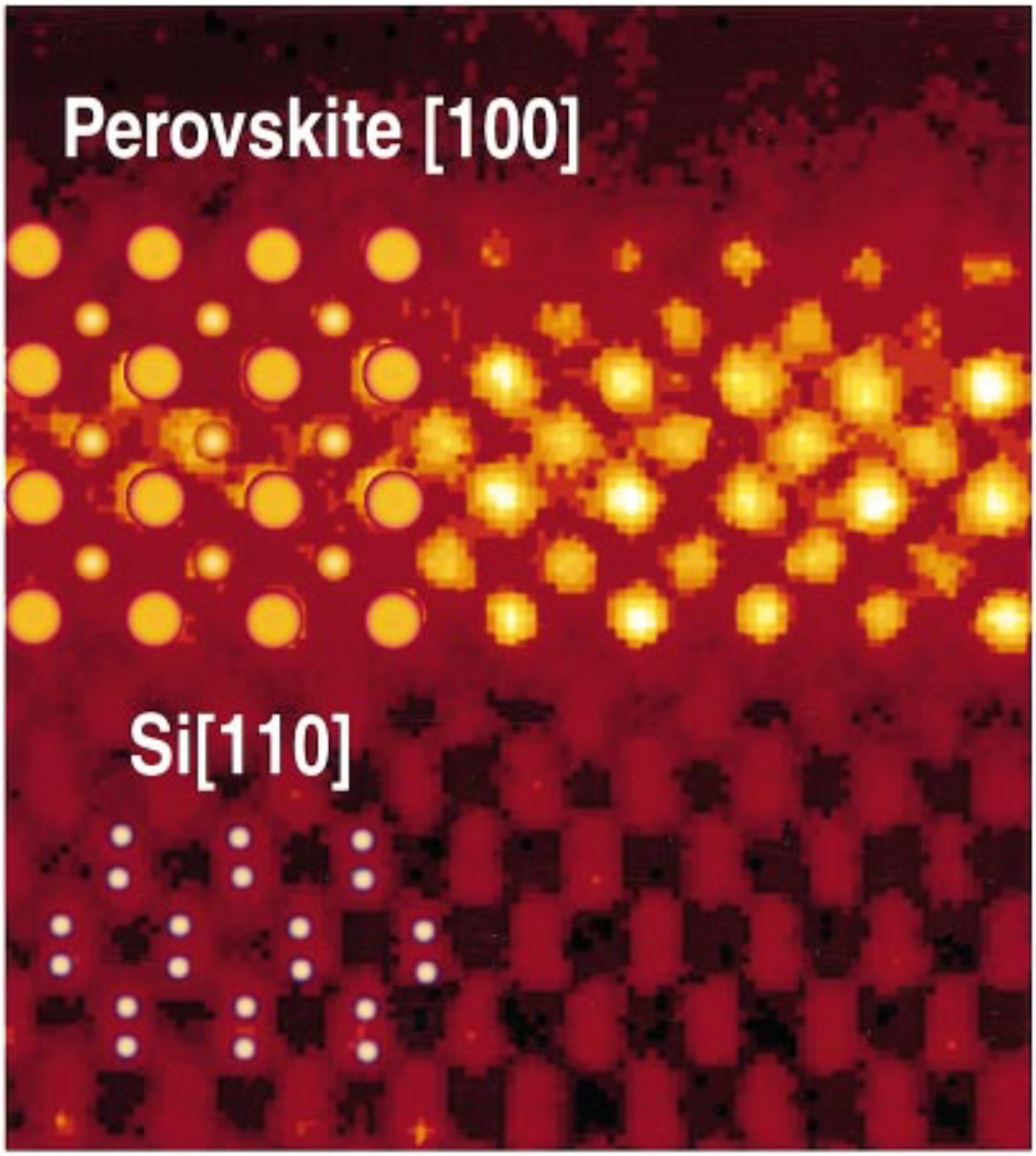

Figure 1.1 Z-contrast image of $SrTiO_3$ on Si (001). The epitaxy is $SrTiO_3$(001) || Si(001) and $SrTiO_3$[110] || Si[100]. Taken from [8]

The compound semiconductor GaAs has much better electron mobility compared to Si, and can serve as a better substrate to bring superior optical or electronic properties into the semiconductor industry. Successful growth of ultrathin STO film on GaAs substrate has been reported by Liang *et. al* in 2004 [28], followed by a series of studies to address interfacial atomic and electronic properties such as interfacial registry, band alignment, and Fermi level pinning [29, 30]. The interfaces between STO and polar oxides have attracted a great deal of attention, after Ohtomo *et al.* [31] discovered an electronic reconstruction in the $LaAlO_3/SrTiO_3$ heterostructure and then a high mobility electron gas at the $LaAlO_3/SrTiO_3$ heterointerface [6]. Other emerging interfacial phenomena include the paramagnetic metal on an anti-ferromagnetic insulator in the $CaRuO_3/CaMnO_3$ system [32], the giant thermoelectric coefficient at the STO/TiO_2 interface[33], and switching of the electrical resistance in an STO crystal [34]. Through the design of superlattices and metastable structures, material properties can also be tailored and synthesized by MBE to atomic-scale precision. Understanding these phenomena requires consideration of oxygen vacancies, transition metal valence change, and interfacial charge transfer [21, 35]. The integration of functional oxides however, necessitates precisely controlled growth procedure, which can be realized by MBE.

Studies on such interfaces are not limited only to experimental, but also performed by theoretical calculations. As a semiconductor with surface dangling bonds, GaAs has been reported to have several types of surface reconstructions [36-40]. Figure 1.2 shows the proposed models for the GaAs(001)-(2x4) surface reconstructions, where we see As and Ga vacancies and surface dimers forming to compensate the dangling bonds. The GaAs(001)-(2x4) surface reconstruction is often called the “technologically important”

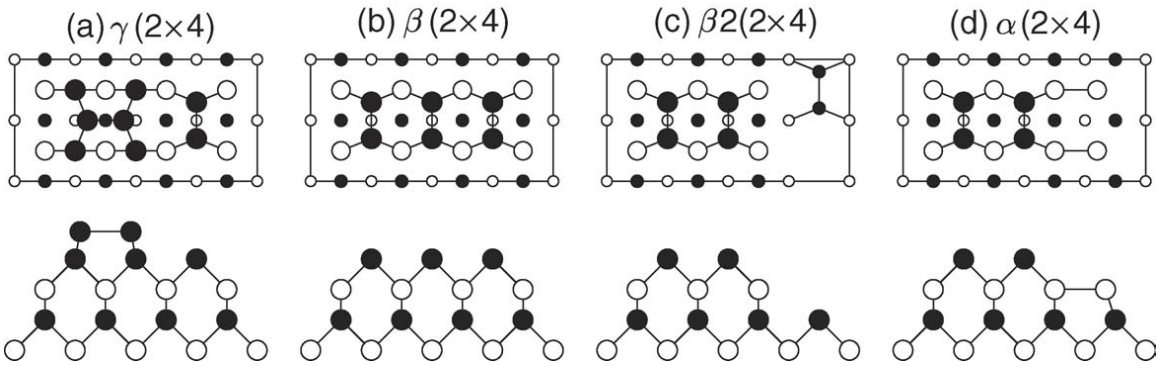

Figure 1.2 Structural models of GaAs(001)-(2x4) surface reconstruction, top view (above) and side view (below) are shown for each model. Filled circles represent As, and empty circles represent Ga. Larger circles represent atoms closer to the surface. Taken from [41]

reconstruction, since it is utilized as the starting surface for growing high-quality GaAs epilayers for commercial optoelectronic devices [42]. Ga-rich GaAs(001)-(2x1) and As-rich GaAs(001)-(2x4) were predicted by considering the electron counting model [43, 44], and observed by utilizing experimental techniques including reflection high-energy electron diffraction (RHEED) and scanning tunneling microscopy (STM) [41, 45-47]. Another low-energy surface reconstruction for GaAs(100) is the c(4x4) reconstructions. Figure 1.3 and 1.4 show ball-and-stick models for this reconstruction [48-50], where an additional As layer is found on top of the As-terminated GaAs surface, and the top layer As atoms are found to be dimerizing. RHEED pattern and STM images confirmed the existence of such reconstructions [46, 48-52]. First principles density functional theory (DFT) was implemented in calculating the total energy of the surface reconstructions [37, 38, 41, 53-56], and it was found that within most of the allowed anion or cation chemical potential, β2-(2x4) surface reconstruction is the lowest energy configuration. As shown in Figure 1.5, with the increase of As chemical potential, the β2-(2x4) surface reconstruction gradually evolves to the c-(4x4) surface reconstruction [57-59], as observed by STM images by Bastiman in 2009 [60]. Other than surface reconstructions of the substrate, theoretical computations were also carried on to study the film growth procedure and the interface between metal (oxide) and semiconductor [61-68]. Given its importance in help interpreting the system energetics, first principles calculations will be utilized in this work.

1.3 Thin Film Growth

In this work, all the thin films I study are grown in the MBE system, which is now located at Texas State University. The system, partly shown in Figure 1.6, consists of

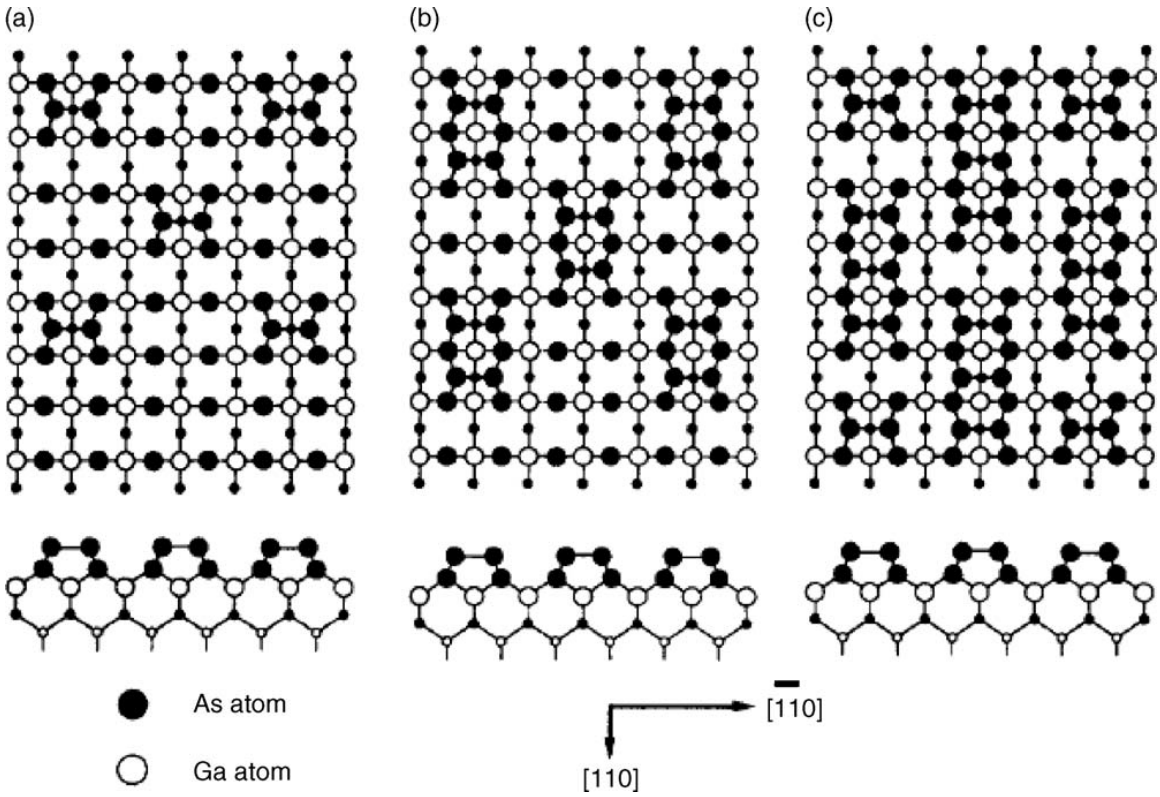

Figure 1.3 Ball-and-stick models proposed for the GaAs(001)-c(4x4) surface. Taken from [48]

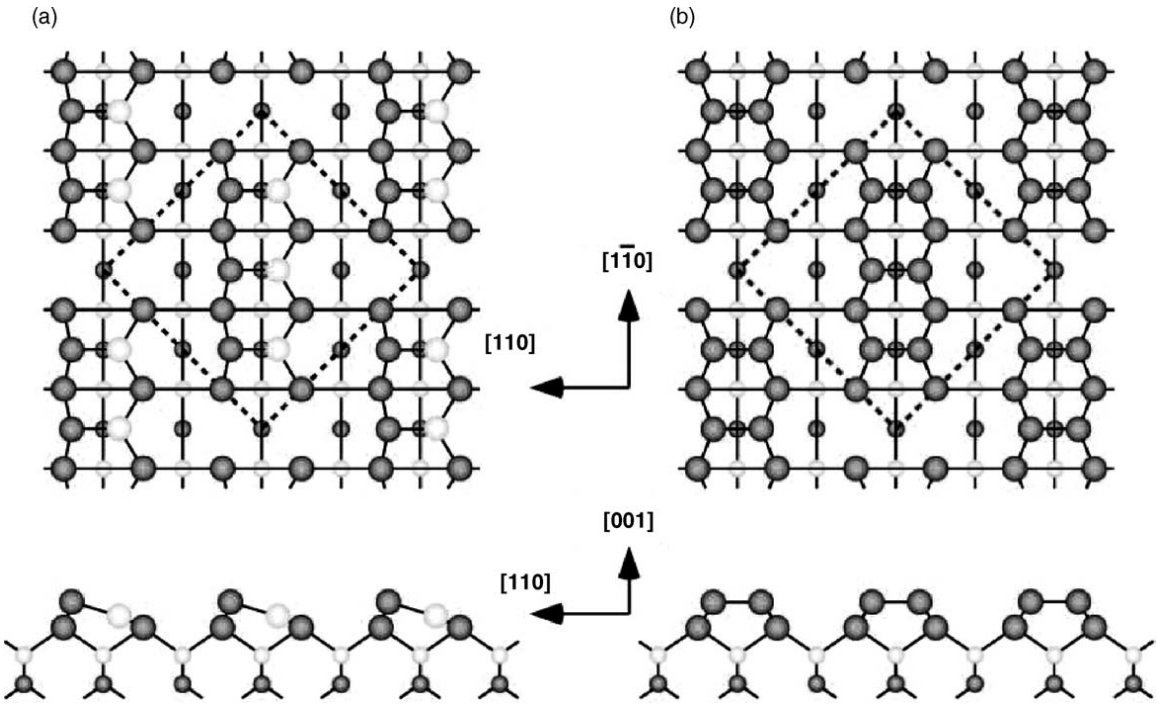

Figure 1.4 Top and side views of α (Ga-As dimer) and β (As-As dimer) structures for As-stabilized GaAs(001)-c(4x4) surface. Close circles denote As, and open circles denote Ga atoms. Taken from [49]

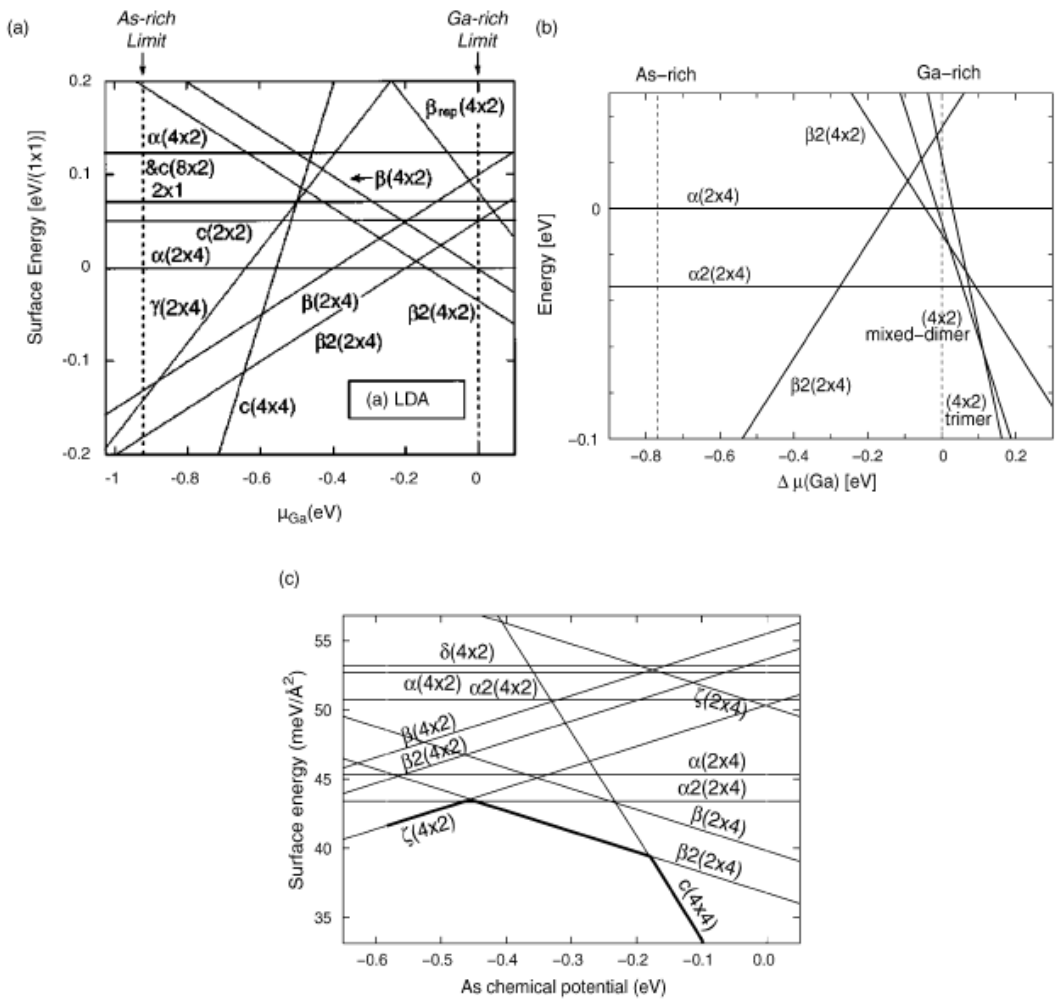

Figure 1.5 Three independently computed phase diagrams of the relative surface energy vs. anion or cation chemical potential. Taken from (a) [57], (b) [58] and (c) [59]

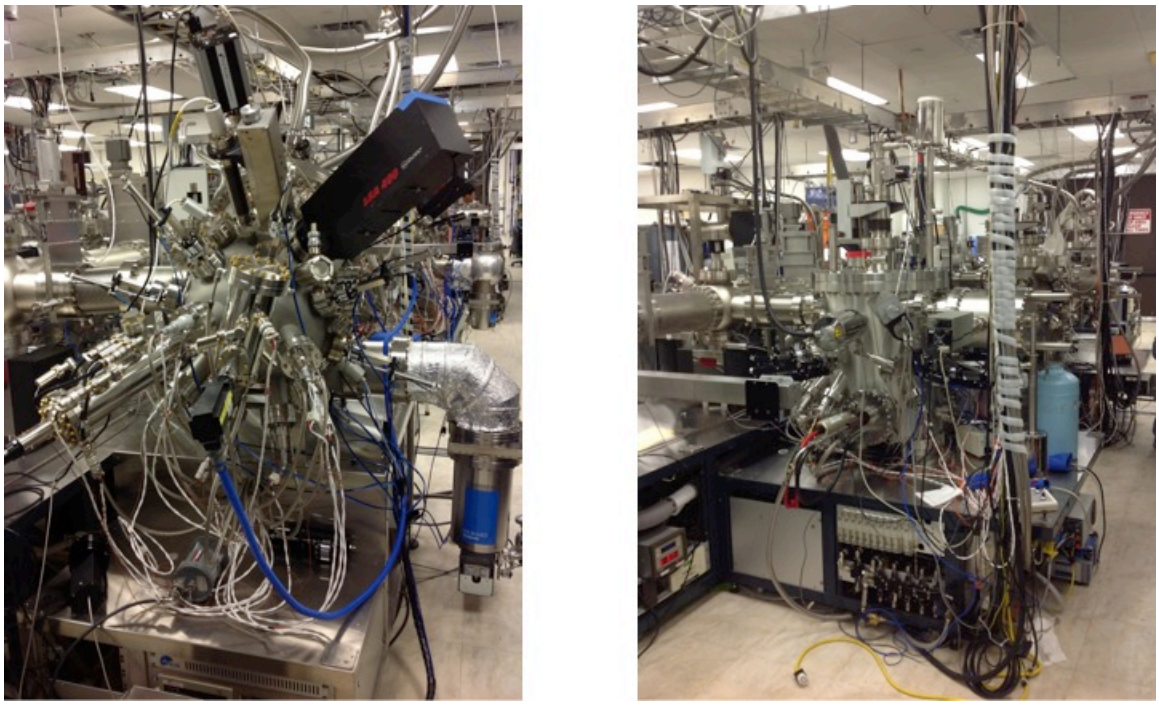

Figure 1.6 MBE growing chambers for semiconductors (left) and complex oxides (right) located at Texas State University

seven inter-connected deposition chambers as well as in-situ analysis and scanning probe spectroscopy chambers that were previously installed at Motorola Labs / Freescale. All deposition chambers are equipped with in-situ RHEED that is used for determining surface morphology, stoichiometry and crystal quality of the growing films. In addition, chambers for x-ray photoelectrons (XPS), x-ray photoelectron diffraction (XPD) and ultra-violet photoelectron spectroscopy (UPS), ion scattering spectroscopy (ISS) and scanning probe microscopy (SPM) allow for the probing of interfaces and surfaces during heteroepitaxial layer growth without exposure to the atmosphere. In-situ measurements are critical to enable direct observation of surface structure of the nucleation layer, providing information on the evolution of interface between the oxide layer and the semiconductor.

Oxide deposition was carried out on both 3 inch diameter Si and GaAs using a multi-chamber molecular beam epitaxy system. In the case for the growth on III–V substrates, an epitaxial layer of GaAs was first deposited in a solid source chamber dedicated for the growth of arsenic containing compounds. After cooling in a flux of As, the epitaxial GaAs layer was then transferred via the UHV buffer to the oxide chamber ensuring a III–V surface that is free of any oxide. Elemental sources and molecular oxygen were used for the growth of the oxide film. On the GaAs substrate, a two unit cell $SrTiO_3$ nucleation layer was used as the buffer layer before the growth of the $BaTiO_3$ layer which was carried out at a substrate temperature of 500 °C in an oxygen flux of $1x10^{-7}$ mbar. The STO nucleation on GaAs uses a ½ ML Ti on a c-(4x4) reconstructed surface using a process described in Ref. [69]. No post growth annealing was used for the BTO film.

1.4 Preliminary Sample Characterization

The surface crystallinity and stoichiometry of the oxide layer were monitored during growth using RHEED, where the flux can be interrupted to ensure a Ba:Ti ratio of unity. The crystalline properties were determined using XRD, and ferroelectric properties of the structures were investigated using PFM.

The as grown layers were determined to be commensurate with GaAs that has an extremely small lattice mismatch with BTO. RHEED pattern along the BTO[110] azimuth after the growth shows streaky features with low background intensity indicative of a high quality commensurate crystalline layer throughout the growth. X-ray diffraction determined that the oxide layers were grown with the c-axis oriented in the growth direction with the oxide layer grown commensurate on GaAs, which has an eligible lattice mismatch with BTO. The oxide layer was found to be ferroelectric with piezo-response amplitude ~5pm/V, and a coercive voltage of V_c = 1-2 V.

1.5 Summary

In this thesis, I will present studies on the perovskite oxide – compound semiconductor interfaces using scanning transmission electron microscopy (STEM) and first principles density functional theory (DFT). In STEM, atomic-resolution Z-contrast imaging, annular bright field (ABF) imaging, and atomic-column resolved electron energy loss spectroscopy (EELS) will be implemented to observe the atomic and electronic structures of the interfaces. DFT calculations are performed to predict and understand the interfacial structures, including atomic registry, surface reconstruction, spontaneous polarization, and electron density of states. A detailed overview of STEM and DFT techniques is given in Chapter 2. This work will be dealing with two systems:

ultrathin $SrTiO_3$ film on GaAs, and ferroelectric $BaTiO_3$ film on $SrTiO_3$/GaAs. Chapter 3 is a study on the STO/GaAs interfaces combining both STEM and DFT. I will show Z-contrast images of two types of STO/GaAs interfaces grown with different conditions of Ti pre-deposition. EELS data will be presented to differentiate the interfaces, which exhibit identical atomic registries. Further understanding of the interfaces can be realized by utilizing DFT calculations, which reveals difference in the electronic structures induced by Ti pre-deposition. Following the experimental findings, I will perform a series of DFT calculations to probe the STO/GaAs interface in Chapter 4. I will first investigate the system energetics given by the thin film stoichiometry, then study the adsorption and diffusion of Ti adatoms on GaAs (001) β2-(2x4) reconstructed surface. Guided by the energy profile of the Ti adatoms, I will further explore the Ti impurities in bulk GaAs. These computational results will help me understand the experimental findings, justifying the atomic registry at the interface and electronic structural changes with respect to Ti pre-layer coverage. After obtaining a fundamental understanding of the STO/GaAs interface, I will apply the experimental and computational methods to the $BaTiO_3$/$SrTiO_3$/GaAs heterointerfaces. In Chapter 5, both Z-contrast and ABF imaging techniques will be included to study the interfacial atomic structure. ABF imaging allows one to observe heavy and light elements simultaneously, hence enables direct observations of oxygen defects and cation-anion displacement. DFT total energy calculation, structural relaxation, and density of states calculation are used to examine the interfacial defects, and predict the occurrence of ferroelectric switching in the BTO film. In Chapter 6, I will summarize and discuss the presented results, and provide directions for future research.

CHAPTER 2

EXPERIMENTAL AND COMPUTATIONAL METHODS

2.1 Scanning Transmission Electron Microscopy

The development of scanning transmission electron microscopy (STEM) dates back to 1937 when Manfred von Ardenne demonstrated a 40 nm spatial resolution of ZnO crystals. In a STEM, electron beam is focused to a small probe and scanned across the specimen in raster as shown in Figure 2.1.

2.1.1 Probe Formation

The electron probe formation begins with accelerating electrons from the source. According to the wave-particle duality of matter, proposed by de Broglie, faster electrons exhibit shorter wavelength, and, if used to image the crystal structure of materials, should therefore also enable better image resolution. As a result, high voltages (usually between 60 kV and 300 kV) are used to accelerate electrons and generate a highly coherent beam of high energy electrons. Although the wavelength of 300 keV electrons is approximately 1.97 pm, the best spatial resolution every achieved in a 300 kV TEM or STEM is only 50 pm [70]. Similarly, the wavelength of 60 keV electron is approximately 5 pm, a probe size of 1 Å can be realized after fifth-order aberration correction [71-73].

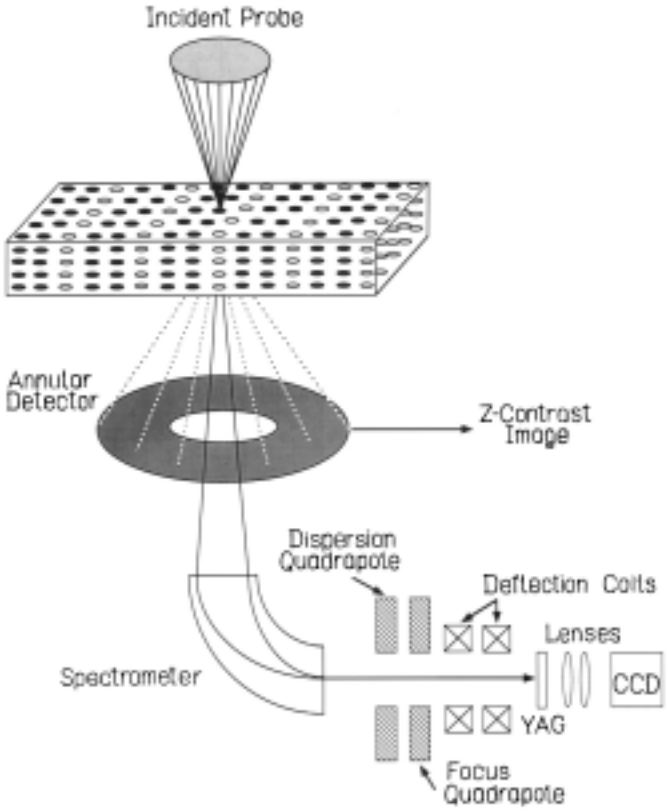

Figure 2.1 Schematic of the detector geometry for a general STEM. Adapated from [74]

Nowadays, the selection of primary electron energy is governed by the need to resolve certain spatial frequencies in the sample materials and the desire to minimize sample damage induced by the electron beam. Beam damage becomes nontrivial when high voltages are implemented, including knock-on damage and ionization damage. For knock-on damage, atoms are knocked out by incoming electrons, and it can be reduced by lowering beam energy. For ionization damage, incident electrons are inelastically scattered. This electron-electron interaction transfers energy to excite the electrons in the sample, and is enhanced by the decrease of electron mean free path due to lower beam energy.

The electron sources used in the electron gun also affect the probe size significantly. Thermionic emission sources heat up filament and provide electrons with energy to overcome the work function energy barrier. The source used in thermionic emission is relatively blunt due to the temperature necessary to overcome the work function. On the other hand, field emission sources pull out electrons with an electric field, which is further enhanced in the presence of a sharp tip. Since the electron probe is a demagnified image of the emission source, field emission gun (FEG) would provide a smaller source and render better spatial resolution. In recent years, the usage of cold-field emission (CFEG) guns has seen a resurgence due to improved gun vacuum and emission current stability. The advantage of CFEG sources over conventional FEG sources is the improved energy resolution and thermal broadening of the source size, since CFEG sources are operated at room temperature.

Once electron beam is generated in the gun chamber, it gets demagnified by a set of condenser lenses C1 and C2, as shown in Figure 2.2. The highest demagnification was

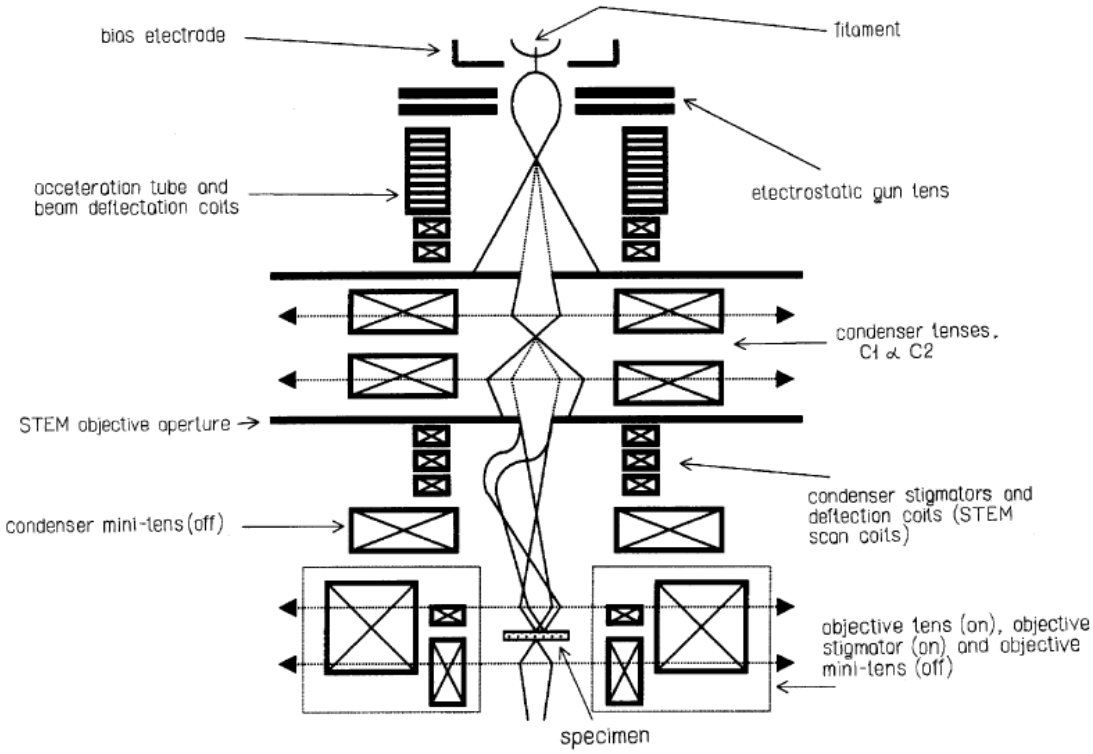

Figure 2.2 Schematic of probe forming optics in the JEOL 2010F STEM. Taken from [74]

achieved when C1 is at its maximum excitation. The C2 lens is used to generate a fixed cross-over for the objective lens located below, which projects the electron gun tip image onto the specimen. Large demagnification, although forming a small probe, reduces the beam current at low angles in the electron probe. Before reaching the objective lens, electron beam also goes through a set of two scanning coils, which deflects the beam to be rastered across the sample. The first layer deflector shifts the beam, and the second layer deflector brings the beam back to parallel with optic axis. The objective lens converges the electron beam and forms the final electron probe to scan the specimen.

2.1.2 Aberration Correction

In an ideal lens, all the rays coming from same origin focus at the same point. In a real lens, due to the inevitable aberrations, it is impossiblefor all the electron to focus electron onto the same point. The upper panel in Figure 2.3 shows angular dependence of the focal plane due to spherical lens aberration, also called C_3. Rays travelling through the lens system away from the optic axis are refracted more than those travelling close to the optic axis. The upper panel in Figure 2.3 shows the effects of chromatic aberration C_c. Rays entering the lens system are deflected differently depending on their wavelength. In an uncorrected STEM, C_3 typically dominates the aberrations. With the development of C_s correctors, C_c now becomes a limiting factor in determining the resolution.

Since the spatial resolution is restricted mostly by spherical aberration, which increase dramatically as a function of distance from the optical axis, aperture are commonly used to limit the range of angles of the incoming electron probe. However, the diffraction limit starts become a limiting factor in achieving the best possible resolution when small apertures are used. Due to the angular dependence of Airy disks, radius of a

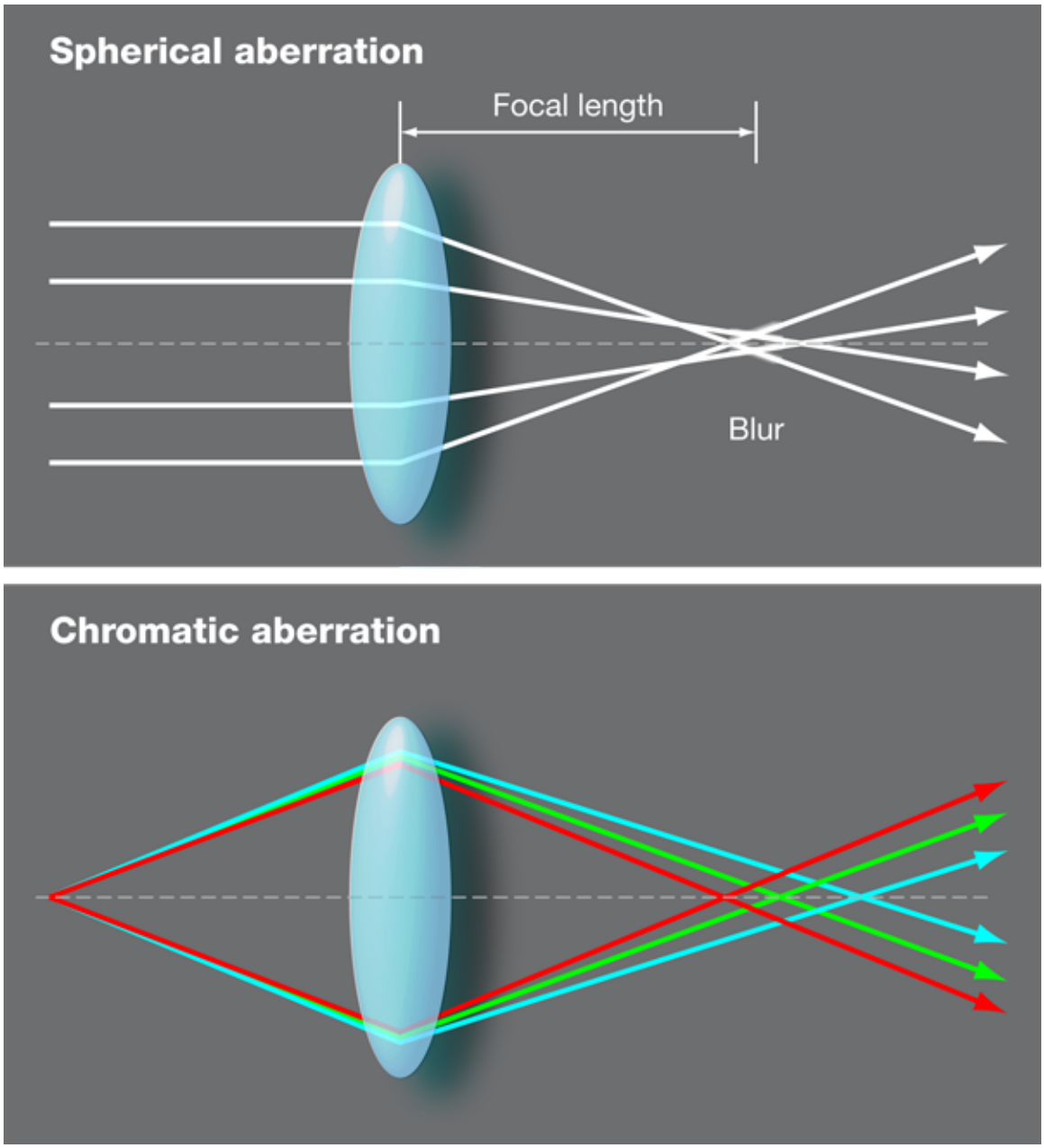

Figure 2.3 Schematic of lens aberrations: (a) Spherical aberration; (b) Chromatic aberration. Taken from [75]

diffraction disk is inversely proportional to the outermost semiangle of the aperture. Using a small aperture may reduce spherically aberration somewhat, but enhances diffraction to compromise the resolution.

It is conventional to express the aberration function as a power series. In a spherical coordinate system with α = 0 on the optic axis, the aberration is expected to be proportional to the magnitude of the α regardless of its sign. Thus, the aberration function can be written as

$$\chi = \frac{2\pi}{\lambda}\gamma = \pi C_1 \lambda \mathbf{K}^2 + \frac{\pi}{2} C_3 \lambda^3 \mathbf{K}^4 + \frac{\pi}{3} C_5 \lambda^5 \boldsymbol{K}^6 + \frac{\pi}{4} C_7 \lambda^7 \mathbf{K}^8 + \cdots \tag{2.1}$$

where λ is the wavelength of the electron, γ is the deviation of aberrated wavefront from the ideal spherical wavefront. **K** is the transverse wave vector and the magnitude $K = \alpha/\lambda$.

C_i is the aberration coefficient, where C_1 is the distance between sample and the Gaussian focal point of the lens. Adjusting specimen stage height along the optic axis or changing focal length of the objective lens could both compensate first order aberration. Third order and fifth order aberrations can be adjusted using hexapole doublet [76-81] or quadropole-octupole pairs [71, 82-85], as implemented in CEOS and Nion aberration correctors, respectively. Table 2.1 shows the residual aberrations of the CEOS corrector installed on JEOL JEM-ARM200CF, under 200 kV, 120 kV, and 80 kV operating voltages.

The probe amplitude can be written as a function of position in the front focal plane [86]

$$P(\mathbf{R}) = \int A(\mathbf{K}) e^{-i\chi(\mathbf{K})} e^{2\pi i \boldsymbol{K}\cdot\boldsymbol{R}} d\mathbf{K} \tag{2.2}$$

where $A(\mathbf{K}) = 1$ inside and 0 outside the aperture. Hence, the diameter of the probe due to aberrations can be determined as a function of defocus, which can be used to determine

	200 kV	120 kV	80 kV
C_1 (nm)	7.927	4.477	-0.9922
C_3 (nm)	-548	73.34	-6.159

Table 2.1 Residual aberrations of the CEOS corrector on the JEOL JEM-ARM200CF.

the optimal aperture size.

Other than C_1, the higher order aberration coefficients are always positive, as shown by Scherzer in 1949 [87]. He also pointed out that higher order aberrations could not be compensated with rotationally symmetric lenses, leading to the development of multipole corrector systems that are used today. It took 50 year for Scherzer's work to be realized due to the required mechanical stability of corrector systems and computational capability of fast CPUs. Nonetheless, Scherzer realized that spatial resolution of microscopes operating at 100-200 kV cannot be less than 2 Å without aberration correction, and a negative C_3 correction should be used to compensate C_5. Before the success of C_3/C_5 corrector, C_3-only correctors were developed and achieved 1.23 Å point-to-point resolution [82, 84].

2.1.3 Z-contrast Imaging

After the electron beam gets through the specimen, there are numerous detectors to collect the elastically and inelastically scattered electron, including a bright field (BF), an

annular bright field (ABF), a low-angle dark-field (LAADF), a medium angle dark-field (MAADF) and a high-angle annular dark field (HAADF) detector. The HAADF detector is used to form a so-called Z-contrast image, where the image intensity I is proportional to Z^n where Z is the atomic number of the constituent atoms and n is a constant ranging from 1.6 to 2 for different collection conditions [88, 89]. During high angle scattering, the incident electrons undergo Rutherford scattering when they pass close to the nucleus of an atom and see the full nuclear potential. Due to the incoherency of the scattered electrons, Z-contrast images are not affected by the phase of the electron beam, giving a much higher image resolution.

The intensity of the image can be mathematically interpreted as

$$I(\boldsymbol{R}) = O(\boldsymbol{R}) \otimes P^2(\boldsymbol{R}) \tag{2.3}$$

where $O(\boldsymbol{R})$ is the object function which is sharply peaked at the atomic columns and $P^2(\boldsymbol{R})$ is the probe intensity profile. The width of the object function is usually around 0.1 Å, which implies that the resolution is dependent only on the electron probe size. Since changing sample thickness or defocus does not reserve the image contrast, Z-contrast imaging is a useful technique to examine various structures such as bulk, surface, interface, and defects [29, 90-92].

2.1.4 ABF Imaging

The lower angle scattered electrons are more coherent hence interfere with each other when forming bright field image. Due to the origin of the bright field image, sample thickness and electron beam defocus play an important role in changing the image contrast. Atoms can appear dark on a bright background when in focus, or bright on a dark background when out of focus. However, the low angle scattered electron beam also

contains incoherent electrons, which are overwhelmed by the high intensity of the coherent signals. In order to sort out the incoherent signals, the ABF technique was introduced by Okunishi *et. al* in 2009 [93]. As illustrated in Figure 2.4, an outer-angle-limiting aperture (also known as bright field aperture) and an inner-angle-limiting disc (also known as beam stopper) are inserted to limit the transmitted electron beam so that the bright field detector at the bottom would receive small angle scattered electrons and avoid most of the diffraction signals. The advantage of this technique is that ABF images are composed of incoherently scattered electrons, so that more non-periodic features would be visible [94]; the ABF detector is more sensitive to light elements, since small angle scattering occurs at the outer shells of the atoms, where all atoms have comparable charge density, as shown in Figure 2.5. Although it has been pointed out that a model calculation is necessary to confirm the qualitative arguments, ABF imaging enables simultaneous observation of light and heavy elements and provides an effective way of studying compounds with complex compositions [93-97].

2.1.5 Electron Energy Loss Spectroscopy

When electrons travel through the specimen, they undergo both elastic and inelastic scattering. Elastically scattered electrons are collected by high angle annular detectors and form Z-contrast image, while inelastically scattered electrons are collected by various spectrometers and used for chemical analysis. Figure 2.6 shows the energy-level diagram of the primary and secondary inelastic processes probing various energy levels of the spectrometers and used for chemical analysis. Figure 2.6 shows the energy-level diagram of the primary and secondary inelastic processes probing various energy levels of the electrons in the specimen. Inner-shell electrons interact with fast incident electrons and

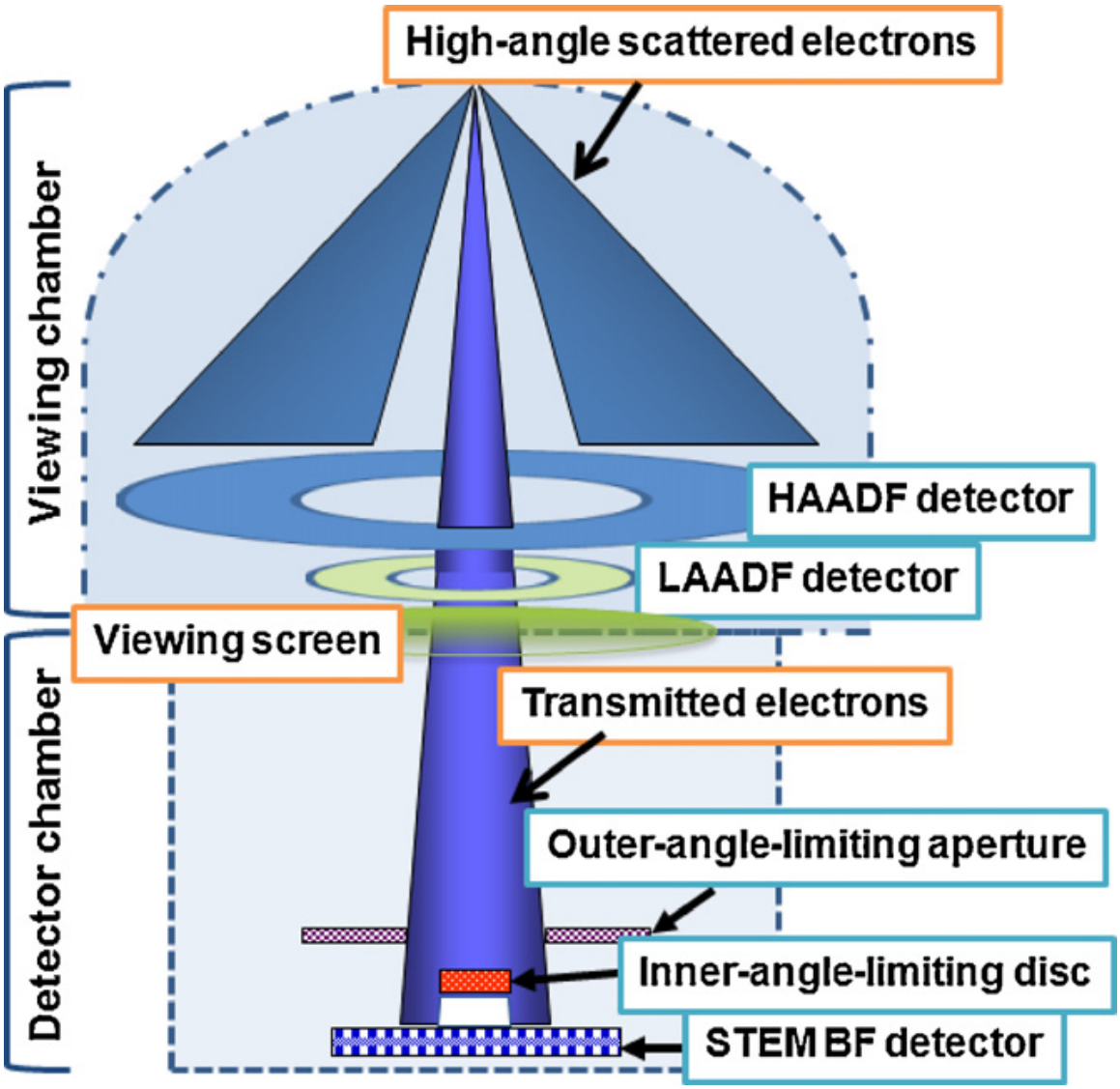

Figure 2.4 Schematic of the detector geometry for JEOL JEM-ARM200CF STEM. Taken from [98]

result in transitions from occupied core-level states to unoccupied states above the Fermi level. In the de-excitation process, an outer-shell electron or an inner-shell electron of lower binding energy undergoes a downward transition to the vacant "core hole" and generate x-rays or Auger electrons. Outer-shell electrons can undergo both single-electron excitations and plasmon excitations induced by incident electrons. For an insulator or semiconductor, valence electrons make interband transitions across the energy gap; for a metal, conduction electrons make transitions to higher states, possibly within the same energy band. If the final state of these transitions lies above the solid vacuum level and the excited electron has sufficient energy to reach the surface, it might be emitted as a secondary electron. In the de-excitation process, there might be electromagnetic radiation emitted as visible cathodoluminescence, or radiationless energy such as heat. The collective phenomenon, although observed mostly in metals, especially the ones with large Fermi surfaces, can occur also in insulators.

Electron energy loss spectroscopy (EELS) is primarily used for measuring the distribution of energies lost by the incident electrons. As shown in Figure 2.7, a typical EEL spectrum can be divided into three regions: Zero-loss peak, low-loss and core-loss regions, each carrying characteristic information of the sample. The zero-loss peak comprises of transmitted electrons without measurable energy loss, including elastically scattered electrons and those that excite phonon modes with energy loss less than the experimental energy resolution. The width of the zero-loss peak is usually used to characterize the energy resolution of the microscope, which is limited by the energy spread of the emission source. After the zero-loss until up to 50 eV is the region called low-loss, corresponding to the interaction of incident electrons with the outer-shell

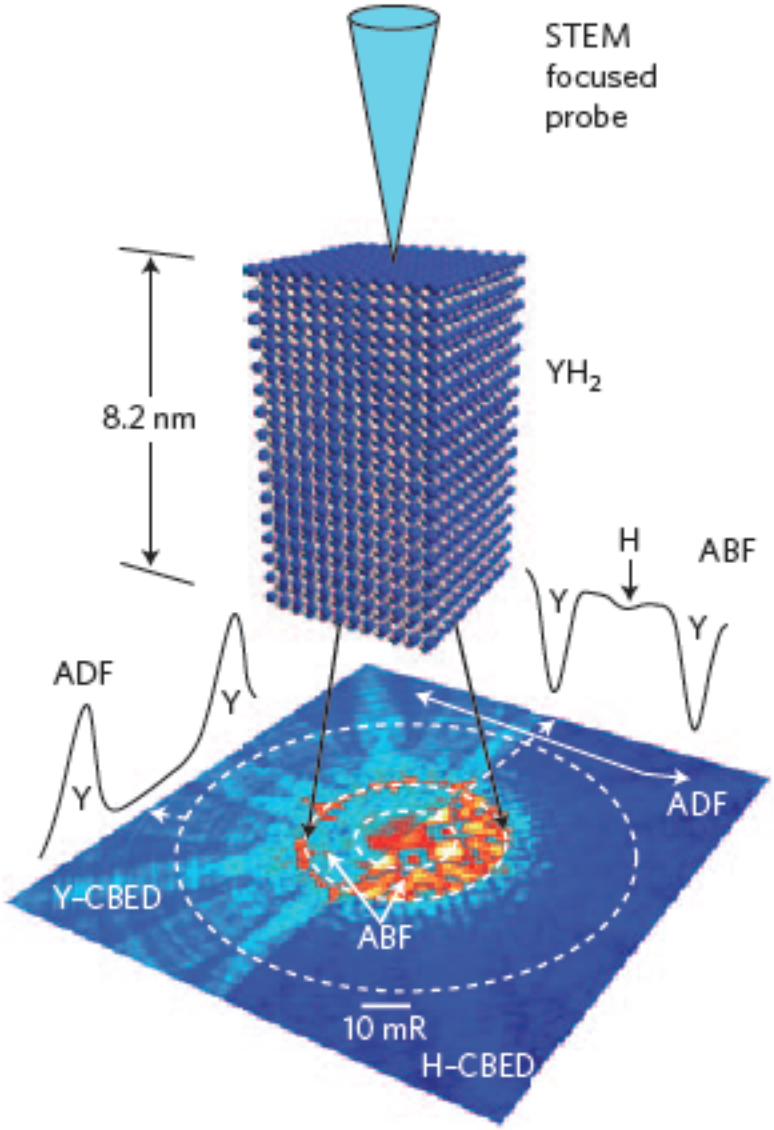

Figure 2.5 Schematic illusion of annular bright field imaging technique. Taken from [94]

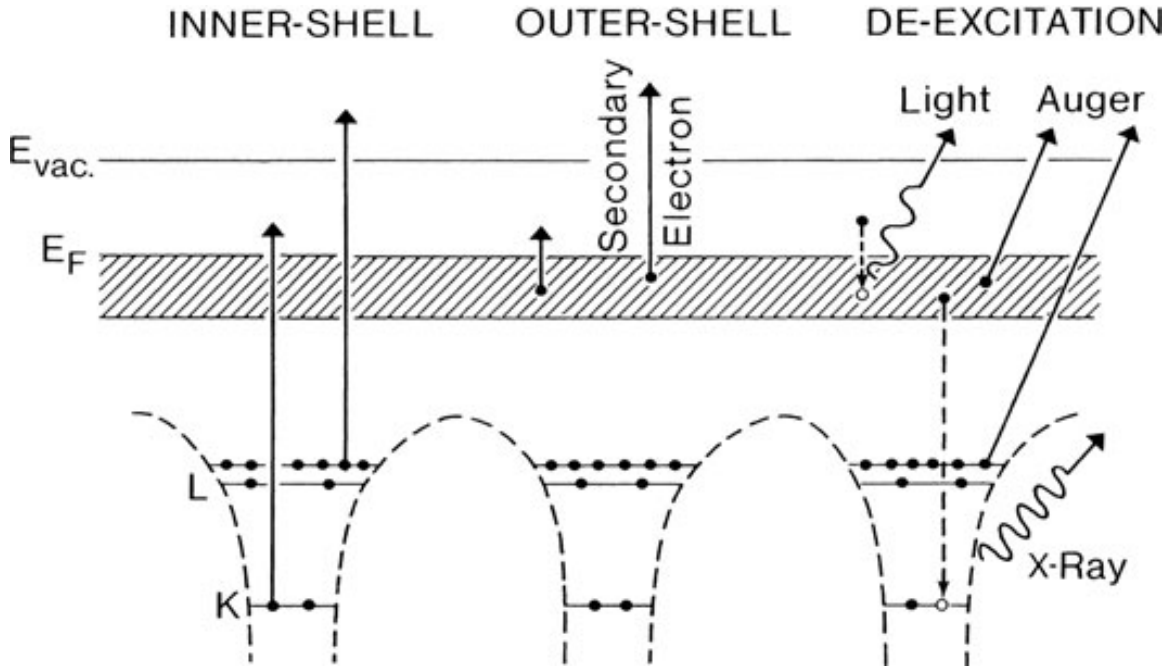

Figure 2.6 Energy level diagram of a solid, demonstrating interaction between incident electron beam and the specimen. Taken from [99]

electrons. Low-loss with good enough resolution can be used to study band gap of a material. The dominant feature in this region is known as plasmon peaks, and the ratio of zero-loss peak and the integrated plasmon peaks is usually used to estimate the sample thickness. The core-loss region is typically studied for recognizing elements included in the specimen and understanding bonding states of each element. These higher energy loss features take the form of edges rather than peaks, the inner-shell intensity rises rapidly and falls slowly into higher energy loss. Edges corresponding to transitions from core levels with principal quantum number n = 1, 2, 3, 4 are called K, L, M and N edges, respectively. A numerical subscript is added to denote the different angular momentum of the same quantum number of the core level. For instance, transitions from *2s* orbitals are called L_1 edge, whereas $2p$ orbitals usually split into two different levels, depending on the angular momentum, $2p_{1/2}$ (where the total angular momentum $j = 1 - 1/2 = 1/2$) and $2p_{3/2}$ (where the total angular momentum $j = 1 + 1/2 = 3/2$). Transitions from $2p_{1/2}$ levels are called L_2 edge, and L_3 edge refers to transitions from $2p_{3/2}$ levels. Since the splitting due to angular momentum is small comparing to the energy loss range, people usually refer to the L_2 and L_3 edges together as the L_{32} edge.

Transmitted electrons are collected by a spectrometer at the end of the column, entering a magnetic prism that deflects, disperses, and focuses them according to their kinetic energy in the plane of an energy-selecting slit. Collecting spectroscopic features as a function of position then produces EELS spectrum image. The application of EELS can be used to compensate the shortage of Z-contrast imaging that cannot extract chemical information about the material, such as identifying or locating certain elements. Using CFEG emission sources also benefits EELS, in the sense that CFEG sources

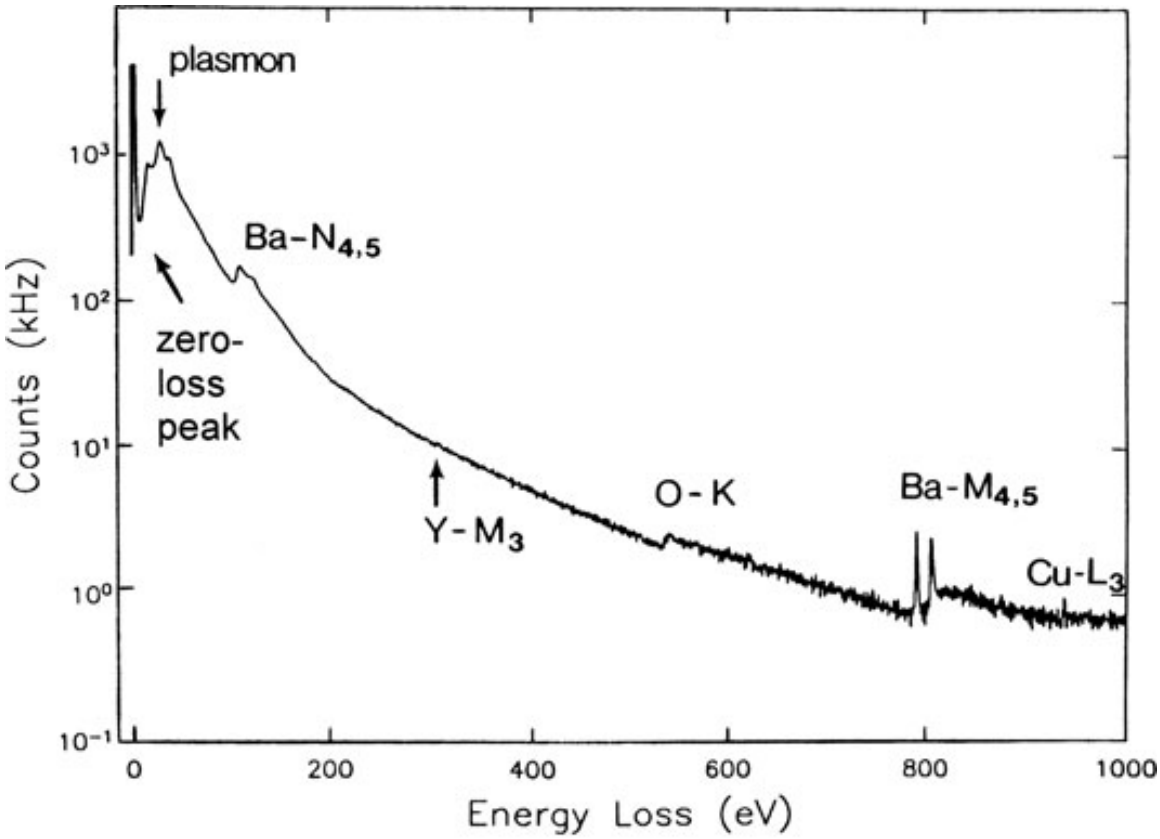

Figure 2.7 Electron energy loss spectrum of high T_c superconductor ($YBa_2Cu_3O_7$) showing zero loss, plasmon peaks, and ionization edges arising from each element. Taken from [99]

generate electrons with much smaller energy spread, allowing for a 0.35 eV energy resolution in the aberration corrected JEOL JEM-ARM200CF.

2.1.6 Spectrum Imaging and Multivariate Statistical Analysis

EELS spectrum imaging technique allows one to obtain a three-dimensional elemental and compositional mapping of the sample. In a spectrum image, spectra are acquired at each pixel as the probe scans across the specimen, creating a three-dimentional data set of energy loss intensity $I(x, y, E)$, as shown in Figure 2.8 [100, 101]. Comparing to the conventional point and line scan approaches, spectrum images provide more detailed information about the sample but suffer a low signal to noise ratio due to shorter acquisition time. Therefore, small fluctuations in the energy loss near-edge and extended fine structures can easily be misinterpreted, leading to a misunderstanding of the electronic structure and bonding states in the specimen. To circumvent this problem, an advanced technique called Multivariate Statistical Analysis (MSA) is developed to analyze large spectrum image datasets [102]. This technique enables automatic extraction of statistically significant and dominant features without bias, followed by the reconstruction of the noise-reduced data after subtracting random noise components. This noise-reduction procedure is achieved by recognizing the most meaningful basis, assumed to be a linear combination of the original basis, to re-express a given dataset. In the new basis, the redundancy is measured by the magnitude of the covariance, while the signal is measure by the variance. Using MSA, the signal to noise ratio is prominently enhanced by minimizing the redundancy and maximizing the signal. In this thesis, MSA will be applied to analyze data acquired from the $SrTiO_3$/GaAs as well as the $BaTiO_3$/$SrTiO_3$/GaAs interfaces.

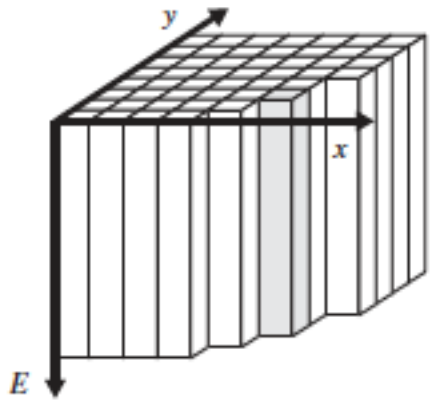

Figure 2.8 Spectrum-imaging acquires it serially in the spatial directions and in parallel in the spectral direction. Taken from [100]

2.1.7 JEOL JEM-ARM200CF at UIC

The JEOL JEM-ARM200CF (Figure 2.9), equipped with a Gatan Enfina EELS spectrometer and a Oxford X-Max80 SDD EDS detector, was delivered to the University of Illinois at Chicago (UIC) in early July 2011, replacing the JEOL JEM-2010F that had been producing atomic-resolution imaging results since late 1998 [103, 104]. The new ARM200CF was the first significant upgrade to the Electron Microscopy Services East laboratory at UIC since 1998, and at the time was the first aberration-corrected, cold-field emission TEM/STEM in the United States.

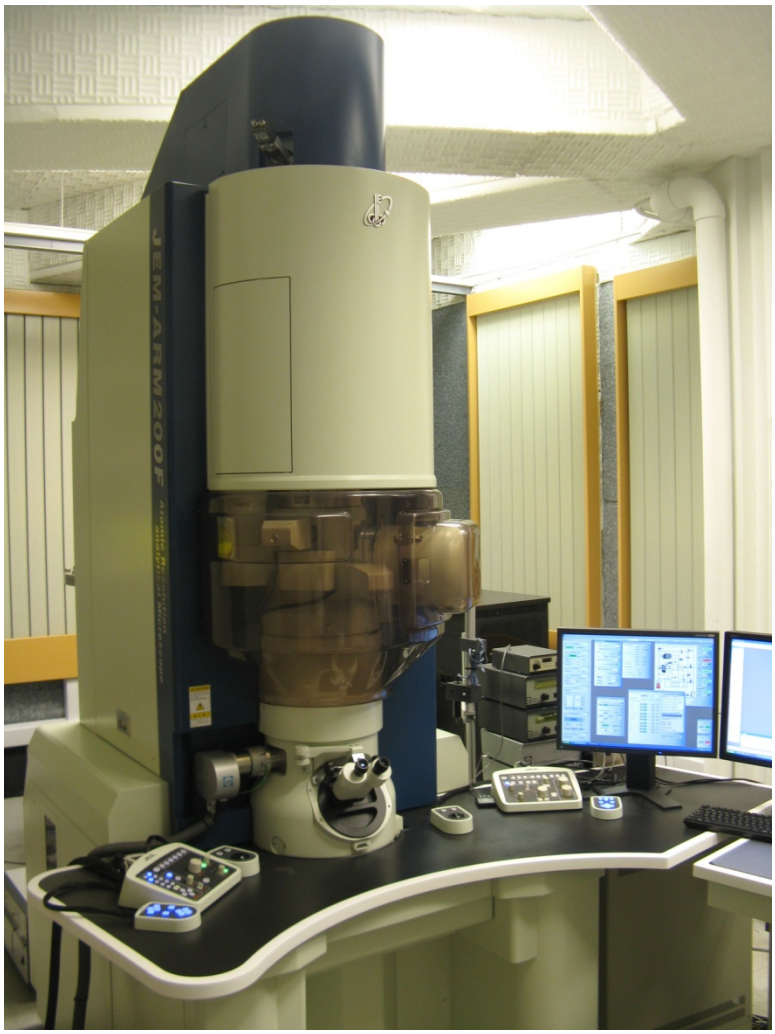

Figure 2.9 The JEOL JEM-ARM200CF at the University of Illinois at Chicago

Prior to installation of this new instrument, we needed to upgrade the laboratory environment to comply with the required temperature and air-flow parameters. Since the laboratory had been used for the JEOL 2010F for the last 13 years, the electric-field and mechanical vibrations were sufficiently low to comply with the installation requriements. However, the temperature control necessary for the JEOL2010F was previously achieved using the air-handling system only, resulting in significant air-movement in the TEM room (>3 ft/min). The new ARM200CF required even stricter temperature and air-flow controls, which were not achieveable using the existing air-condition system. We therefore chose radiant cooling panels controlled by four temperature sensors in the TEM room and a closed-loop chiller to control the air temperature, while reducing the air-flow to significantly less than 1 ft/min. The resulting temperature control is shown in Figure 2.10, demonstrating that over a 14 hour period, the temperature remains stable within 0.1 °C.

In less than 3 months from the delivery of the ARM200CF, we had achieved atomic-resolution imaging capabilities with sub-Å resolution and in late 2011, less than 6 months after the initial delivery, we accepted the installation. The spatial resolution that can now be routinely achieved in the JEOL ARM200CF exceeds 70 pm at 200 kV primary energy (see Figure 2.11a) and 100 pm at 80 kV primary energy. The energy resolution of the EEL spectra at any energy between 80 and 200 kV is 350 meV (see Figure 2.11b). The stability of the instrument was measured using a long-exposure HAADF image without drift correction, and was determined to better than 150 pm/min.

In addition to the double tilt holders, we also took delivery of a Gatan double-tilt liquid He cooling stage, a Protochips Aduro double tilt heating stage, a Fischione

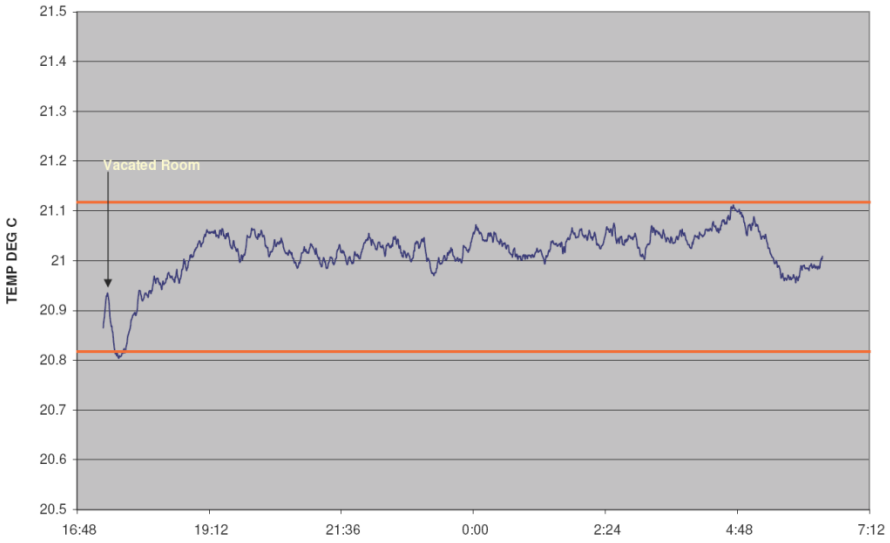

Figure 2.10 Room temperature measure over 14 hours showing stability of better than 0.1 °C

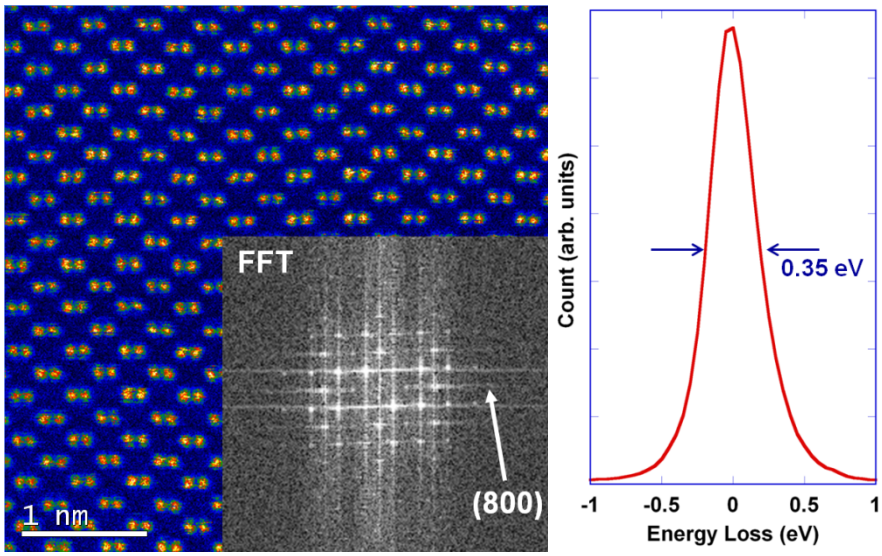

Figure 2.11 a) HAADF image at 200 kV of Si (110) with Fourier transform shown as insert. b) Zero-loss peak with indicated full width at half maximum.

tomography stage, and over the following two years a Nanofactory STM-TEM stage and a Protochips Poseidon liquid flow cell. In addition, we have still access to the Gatan double tilt heating and the double tilt LN_2 cooling stage, which were purchased in 1998 for use in the JEM-2010F. At this point, it is important to note that switching between TEM and STEM mode can be done without disturbing the alignment or stability of the instrument significantly. For example, when switching from TEM to STEM mode, it is possible to achieve atomic resolution nearly immediately after the coma and astigmatism have been manually corrected. At the highest imaging resolution, we notice that during the first 60-120 minutes after entering STEM mode, some adjustment of the focus and stigmator is necessary. Once the ARM200CF has been in STEM mdoe for two hours, the instrument is completely stable.

The ARM200CF is located in an open-access user-facility, which allows qualified users to use the instrument 24 hours, 7 days per week on an hourly user-charge basis [105]. It is, therefore, crucial that any of the experimental setups required by the user are not affecting the performance of the instrumentation for the subsequent users. To date, we have not experienced any significant influence of any in-situ experiments or low-voltage measurements on the vacuum column or energy-stability performance for more than a few hours after the completion of the experiments.

2.2 First Principles Density Functional Theory

2.2.1 Born Oppenheimer Approximation

The interpretation of the diverse effects observed in complex materials needs help from quantum mechanical theories. For a many-body system such as a crystal, the

Hamiltonian, which involves both electronic and ionic degress of freedom and the electron-electron, electron-ion interactions, is too complicated to solve even computationally unless some justifiable approximations are made. The first such approximation is the Born-Oppenheimer approximation, which allows one to treat electrons and nuclei of a system separately as a result of the large mass difference between them. Based on the fact that electrons are much lighter than ions, they can move quickly into an instantaneous ground state given a certain configuration of ions. In practical terms, the Born-Oppenheimer approximation implies that the ionic degress of freedom can simply be viewed as parameters in the many-body Hamiltonian. In this way, the ionic positions are assumed to be fixed when calculating the wavefunction of a system. The most energetically favorable structure can be found by computing the forces on the ions and moving them accordingly, until a minimum-energy ionic configuration is found.

Taking into consideration the electron-electron, ion-electron, and ion-ion interactions, the Hamiltonian can now be written as

$$\widehat{H} = -\frac{\hbar^2}{2m_e}\sum_i \vec{\nabla}_i^2 + \frac{1}{2}\sum_{i\neq j}\frac{e^2}{|\mathbf{r}_i-\mathbf{r}_j|} + \frac{1}{2}\sum_{i,I}\frac{Z_I e^2}{|\mathbf{r}_i-\mathbf{R}_I|} + \frac{1}{2}\sum_{I\neq J}\frac{Z_I Z_J e^2}{|\mathbf{R}_I-\mathbf{R}_J|} \tag{2.4}$$

where m_e is the electron mass, e is the charge of an electron, $\mathbf{r}_i$ is the position of the electrons, $\mathbf{R}_i$ is the ionic position, and Z_I is the nuclear charge. The last term becomes a constant when determining the electronic degrees of freedom. However, this Hamiltonian is still too hard to work with for systems with many electrons, hence, further approximations are needed to simplify the problem.

2.2.2 Density Functional Theory

In 1964, Hohenberg and Kohn demonstrated that for an interacting electron gas under an external potential $V_{\text{ext}}(\mathbf{r})$, the ground state charge density $n(\mathbf{r})$ uniquely determines $V_{\text{ext}}(\mathbf{r})$ (up to a constant) [106]. Since the external potential determines the wavefunction of the system, the relationship between density and the potential implies that the wavefunction, hence all properties of the system, can be determined from the ground state density.

The second Hohenberg-Kohn theorem then states that a universal functional of the energy $E[n(\mathbf{r})]$ in terms of the density can be defined for any external potential $V_{\text{ext}}(\mathbf{r})$ and that this functional assumes its minimum for the exact ground state density $n(\mathbf{r})$. The functional whose existence can be easily proven is given by

$$E[n(\mathbf{r})] = F[n(\mathbf{r})] + \int n(\mathbf{r})\, V_{\text{ext}}(\mathbf{r}) d^3\mathbf{r} \tag{2.5}$$

where $F[n(\mathbf{r})]$ is the expectation value of the many-body kinetic energy T and electron-electron interaction U operators in the ground state wavefunction. The Hohenberg-Kohn theorem allows one to assert the existence of this functional of density without having to know the many-body wavefunction. However, no explicit expression for this functional is known to date.

In 1965, Kohn and Sham developed a set of equations using an auxiliary system consisting of non-interacting particles with the same density as that of the real many-body system [107]. They started by writing the functional $F[n(\mathbf{r})]$ as

$$F[n(\mathbf{r})] = T_s[\mathbf{r}] + \frac{e^2}{2}\int \frac{n(\mathbf{r})n(\mathbf{r}')}{|\mathbf{r}-\mathbf{r}'|} d\mathbf{r}d\mathbf{r}' + E_{xc}[n(\mathbf{r})], \tag{2.6}$$

where the kinetic energy

$$T_s[\mathbf{r}] = \sum_i \left\langle \psi_i \middle| -\frac{\hbar^2}{2m_e}\nabla^2 \middle| \psi_i \right\rangle \tag{2.7}$$

comes from the single particle states $\{\psi_i(\mathbf{r})\}$ that gives rise to the density $n(\mathbf{r})$ through

$$n(\mathbf{r}) = \sum_{j=1} \left|\psi_j(\mathbf{r})\right|^2 \tag{2.8}$$

where the sum is over all occupied states. The last term $E_{xc}[n(\mathbf{r})]$ in Eq. 2.6 is called the exchange-correlation energy functional, which accounts for the differences between the non-interacting fictitious system and the real interacting one, collecting the contributions from the non-classic electrostatic interaction and the difference in their corresponding kinetic energies. Since the $E_{xc}[n(\mathbf{r})]$ term is a small fraction of the total energy and can be approximated surprisingly well, using Kohn-Sham approach can successfully solve the interacting electron gas problem.

If the energy functional defined in Eq. 2.5 and Eq. 2.6 is varied with respect to the wavefunction subject to the orthonormality constraint, Schrödinger-like equations (for non-interacting electrons) can be written as

$$\left[-\frac{\hbar^2}{2m_e}\nabla^2 + v_{\text{eff}}\big(\mathbf{r}, n(\mathbf{r})\big)\right]\psi_i(\mathbf{r}) = \epsilon_i \psi_i(\mathbf{r}) \tag{2.9}$$

where the effective potential $v_{\text{eff}}(\mathbf{r}, n(\mathbf{r}))$ is given as

$$v_{\text{eff}}\big(\mathbf{r}, n(\mathbf{r})\big) = V_{\text{ext}}(\mathbf{r}) + e^2 \int \frac{n(\mathbf{r}')}{|\mathbf{r}-\mathbf{r}'|} d\mathbf{r}' + \frac{\delta E_{xc}[n(\mathbf{r})]}{\delta n(\mathbf{r})} \tag{2.10}$$

Equations 2.8, 2.9 and 2.10 are known as the Kohn-Sham equations and have to be solved self-consistently due to the dependence of $v_{\text{eff}}(\mathbf{r})$ on $n(\mathbf{r})$.

2.2.3 Approximations for the Exchange-Correlation Energy Functional

The exchange-correlation functional $E_{xc}[n(\mathbf{r})]$, as mentioned before, is not known exactly given a general $n(\mathbf{r})$. Therefore, approximations are necessary to proceed further. To date, various approximation methods have been used. The simplest and most extensively tested approximation is the local density approximation (LDA), in which

$E_{xc}[n(\mathbf{r})]$ for the inhomogeneous system is constructed from a parameterized form of exchange-correlation energy density of the homogeneous electron gas $\varepsilon_{xc}^{hom}[n(\mathbf{r})]$,

$$E_{xc}[n(\mathbf{r})] = \int \varepsilon_{xc}^{hom}[n(\mathbf{r})]n(\mathbf{r})d\mathbf{r} \tag{2.11}$$

Several parameterization methods based on Monte Carlo simulations and many-body perturbation theory are used for the exchange-correlation energy of a homogeneous electron gas [108-112]. The exchange-correlation interaction should be nonlocal in principle, however, it is surprising that LDA works remarkably well [113-115]. In order to portray $E_{xc}[n(\mathbf{r})]$ more accurately, a slightly less local approximation called the generalized gradient approximation (GGA) was developed [116, 117]. In GGA, $E_{xc}[n(\mathbf{r})]$ depends not only on the density at **r** but also its gradient. This approximation usually gives better description than LDA on some of the structural energetics properties of real materials, such as cohesive and adsorption energies.

2.2.4 Pseudopotentials and Projector Augmented Wave Method

From Bloch's Theorem, the wavefunctions of a crystal can be written as the product of a cell-periodic function and a plane wave part. The cell-periodic function can be expanded as a series of plane waves in terms of the reciprocal lattice vectors. Using periodic boundary conditions, the infinitely large number of electrons in a crystal are represented by a finite set of electronic states at an infinite number of k-points. Methods have been derived to take advantage of the crystal symmetry, and only a small set of special k-points are needed for an accurate interpretation [118].

When plane waves are used as a basis set, the Kohn-Sham equations can be simplified as

$$\sum_{\mathbf{G}'}\left[\frac{\hbar^2}{2m_e}|\mathbf{k}+\mathbf{G}|^2\delta_{\mathbf{GG}'} + v_{\mathrm{eff}}(\mathbf{G}-\mathbf{G}')\right]c_n(\mathbf{k}+\mathbf{G}') = \varepsilon_{\mathrm{k}n}c_n(\mathbf{k}+\mathbf{G}) \tag{2.12}$$

The completeness of the plane wave basis set is broken when only a finite number of plane waves are considered. However, assuming a large enough basis set, the sum over **G** vectors can still provide an adequate representation of the cell-periodic part of the wavefunctions. Typically, the size of the basis set is determined at each **k**-point by including only those **G** vectors with kinetic energies $\frac{\hbar^2}{2m_e}|\mathbf{k}+\mathbf{G}|^2$ less than a chosen energy cutoff E_{cut}.

Since the core electrons do not usually contribute significantly to the physical properties of solids, and their inclusion would require a very large number of **G** vectors due to their rapid oscillations and spatial localization, their effect can be combined with that of the nucleus to create a weaker potential, called the pseudopotential, that acts on the valence electrons [119-121]. This approximation allows the electronic wavefunctions to be expanded with a much smaller plane wave basis set. As shown in Figure 2.12, pseudopotentials are designed to match the full ionic potential outside of a cutoff radius r_c, and produce a smooth wavefunction inside that radius. The smoothness of the wavefunction allows one to use a lower planewave energy cut-off, and to significantly reduce the computational cost of the calculation.

The calculations mentioned in the later chapters of this work, are performed by using the projector augmented wave (PAW) method of Blöchl [122]. PAW method is a generalization of the pseudopotentials and full potential augmented plane wave approach. It combines the advantages of both methods by keeping the nodal structure of the wavefunctions inside the core and while exhibiting the simplicity and numerical efficiency of pseudopotentials. The method is based on a linear transformation T,

between the true valence wavefunctions with their complete nodal structure and the smooth auxiliary wavefunctions with a rapidly convergent plane wave expansion

$$|\psi_n\rangle = \hat{T}|\tilde{\psi}_n\rangle \tag{2.13}$$

The transformation is assumed to be unity except for a sphere centered on the nucleus (augmentation region), whose cutoff radius should be chosen to avoid overlap between neighboring augmentation spheres. Then transformation T can then be written as

$$\hat{T} = 1 + \sum_a \hat{T}^a \tag{2.14}$$

where a is the atom index. All physical quantities such as $\langle\psi_n|A|\psi_n\rangle$ can be calculated in the pseudo Hilbert space representation $\langle\tilde{\psi}_n|\tilde{A}|\tilde{\psi}_n\rangle$ with $\tilde{A} = \hat{T}^\dagger A\hat{T}$ rather than directly from the true wavefunctions. Similarly, using variational principles for the total energy, one could write Kohn-Sham equations for the pseudopotentials as

$$\frac{\partial E[\hat{T}|\tilde{\psi}\rangle]}{\partial\langle\tilde{\psi}|} = \varepsilon\hat{T}^\dagger\hat{T}|\tilde{\psi}\rangle \tag{2.15}$$

Hence, ground state calculations can now be performed in the pseudo Hilbert space, which can be efficiently expanded by the plane waves.

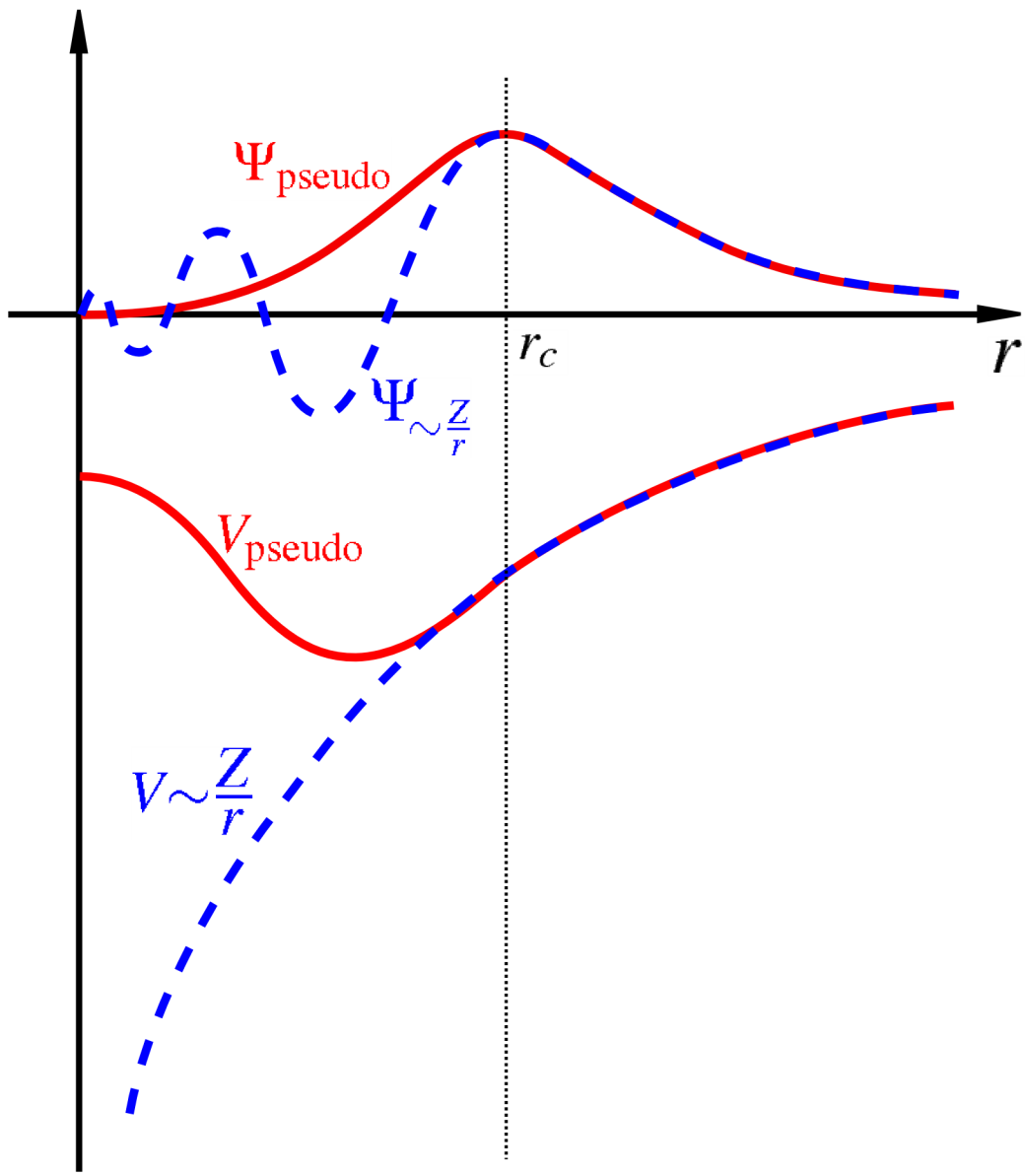

Figure 2.12 Schematic representation of the pseudopotential and pseudowavefunction comparing to the full ionic potential and all-electron wavefunction

CHAPTER 3

ATOMIC AND ELECTRONIC STRUCTURES OF $SrTiO_3$/GAAS HETERO-INTERFACES: A 80 KV ATOMIC-RESOLUTION ELECTRON ENERGY-LOSS SPECTROSCOPY STUDY

3.1 Introduction

Crystalline complex oxide thin films on semiconductor substrates have emerged as an alternative to SiO_2 based technologies in fabricating the metal-oxide-semiconductor field-effect transistors (MOSFETs). This is due to fact that such complex oxides can act as effective insulators without compromising the thickness of the film. Moreover, these materials can be studied with a variety of experimental and theoretical tools.[15] Compound semiconductors have also been considered for replacing silicon channel due to better electron mobilities and velocities.[123] In addition, over the last few years, ultrathin metal-oxide films on polar semiconductor surfaces have received much attention due to the emergence of novel interfacial phenomena, including ferroelectricity, superconductivity and the presence of an interfacial 2-dimensional electron gas.[5, 6, 18, 124-126] For more than two decades now, various techniques have been used to achieve a layer-by-layer crystalline oxide film deposition, including pulsed laser deposition and molecular beam epitaxy (MBE), in an effort to avoid the formation of the amorphous layer at the interface.[7, 127]

The synthesis of single crystalline $SrTiO_3$ films on polar semiconducting GaAs using MBE was first reported by Liang et al.[28, 30] These $SrTiO_3$/GaAs interfaces were then characterized using atomic-resolution Z-contrast imaging and X-ray photoemission spectroscopy (XPS),[29] as well as preliminary first principles density functional theory (DFT) calculations in an effort to obtain a fundamental understanding of the structural and electronic properties.[128-130] It has been reported that the film prefers to be SrO terminated at the interface, regardless of the growth conditions, and a submonolayer of Ti between the oxide and semiconductor can relieve the Fermi level pinning after the completion of the thin film deposition. However, due to the sensitivity of the $SrTiO_3$/GaAs interface to the high-energy electron beam, it was not possible to perform atomic resolution electron energy-loss spectroscopy (EELS) at the time.[29] Accordingly, a detailed understanding of the electronic structures at the interface is still missing. Until recently, atomic resolution imaging and spectroscopy at primary energies less than 100 kV was not possible. However, advances in instrumentation design now allow for such characterization to be performed at electron energies as low as 60 kV.[131, 132] In this chapter, I report atomic-scale studies of $SrTiO_3$/GaAs interfacial structures by utilizing atomic-resolution Z-contrast imaging in combination with atomic column resolved EELS at 80 kV. I combine these experimental results with first-principles computations for O *K*-edges to help understand the interfacial atomic and electronic structures.

3.2 Methods

As reported by Klie et al,[29] the $SrTiO_3$ thin films were grown on the As-terminated p-GaAs (001) by MBE with atomic-layer precision using two types of growth method. In the first method, one half-monolayer of Ti was deposited on the GaAs substrate before

the $SrTiO_3$ deposition (sample 1); in the second method, the As stabilized GaAs surfaces were exposed to the evaporated Sr and Ti under a controlled oxygen pressure (sample 2).[28] The experimental data were obtained using the JEOL ARM200CF scanning transmission electron microscopy (STEM), equipped with a cold field emission source resulting in 0.3 eV energy resolution when operated from 80-200 kV, and a probe spherical aberration corrector allowing for 1.2 Å spatial resolution in HAADF imaging at 80 kV.[133] The atomic-resolution Z-contrast images were acquired at 80 kV, with a collection semiangle from 90 to 170 mrad and convergence semiangle of 22 mrad. For EELS at 80 kV, a convergence angle of 30 mrad and a collection angle with 35 mrad were used. Using a primary voltage of 80 kV, the interfaces were found to exhibit no damage even after repeated exposure to the electron beam. First principles calculations were performed within the framework of density functional theory using the projector augmented wave method as implemented in VASP.[122, 134] The exchange-correlation term were treated with local density approximation. Plane waves were used as the basis functions with a cutoff energy of 300 eV. Integration in the reciprocal space was performed by the Monkhorst-Pack scheme using the 12×12×12 mesh for perovskite STO, 6×6×6 mesh for cubic arsenolite As_2O_3, and 6×12×4 mesh for monoclinic claudetite As_2O_3.

3.3 Results and Discussion

Figure 3.1(a) and (b) show the high-resolution Z-contrast image of the sample 1 and sample 2. The images were processed with 2D differential filter to filter the noise.

The colored rectangles highlight the individual scan areas. The proposed atomic columns of the interface are shown at the bottom, and the dotted lines mark the interface between

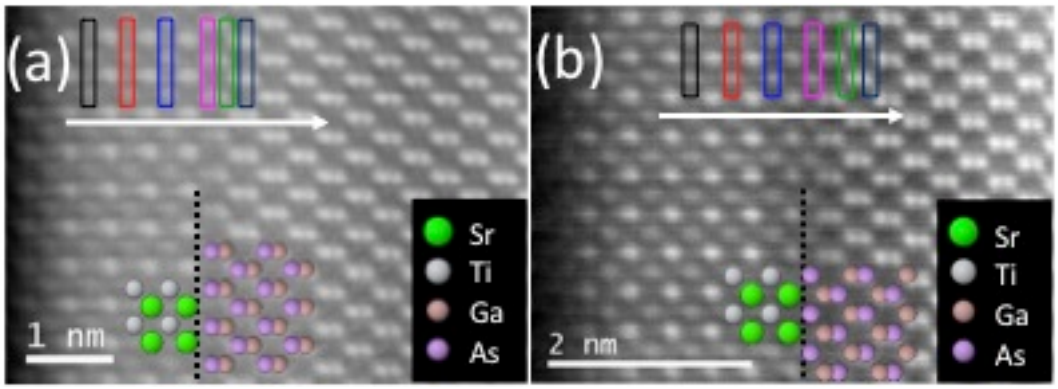

Figure 3.1 High-resolution Z-contrast image of the $SrTiO_3$/GaAs interface of (a) Sample 1 (with Ti pre-layer) and (b) Sample 2 (without Ti pre-layer). The colored rectangles highlight the individual scan areas, the proposed atomic columns of the interface are shown at the bottom, and the dotted lines mark the interface between the thin film and the As terminated substrate

the $SrTiO_3$ thin film and the As terminated GaAs substrate. Figure 3.1(a), with the $SrTiO_3$ [010]||GaAs [110] epitaxy, shows a sharp interface with SrO layer of the thin film in perfect registry with the As terminated substrate, providing no evidence of the Ti pre-layer presence at the interface. It is also interesting to note here that the interface appears abrupt and no surface reconstruction of the GaAs (001) surface is observed. Figure 3.1(b), with the $SrTiO_3$ [100]||GaAs [$1\bar{1}0$] epitaxy, shows the interface of the thin film deposited without Ti pre-treatment, also bearing no mark of any surface reconstruction on the substrate. I find that while several previous studies on bare, As-terminated GaAs (001) surfaces have found the (2×4)-β2 surface reconstruction to be energetically favorable,[41, 43, 44, 55, 135, 136] it appears that the $SrTiO_3$ deposition eliminates this surface reconstruction as inferred from our Z-contrast images.[29] These findings are consistent with a previous Z-contrast imaging study, which showed that the $SrTiO_3$ films with and without the Ti pre-layer appear to be structurally identical.[29] However, in that previous study, Klie et al.[29] were not able to explain the observed differences in the electronic properties of the two samples, since atomic-resolution EELS was not possible at 200 kV.

In this study, using an 80 kV electron beam, I can now explore the interfacial electronic structure using atomic resolution EELS spectrum imaging of the Ti *L*- and O *K*-edges. The acquired Ti *L*-edges of sample 1 (on the left) and sample 2 (on the right) are shown in Figure 3.2(a) and (b), respectively. The uppermost spectrum shows a reference taken from bulk $SrTiO_3$, which provides the near-edge fine structures for Ti 4+. Each of the other colored spectra corresponds to the signal enclosed by the corresponding rectangle superimposed on the image in Figure 3.1(a) and (b), providing the average

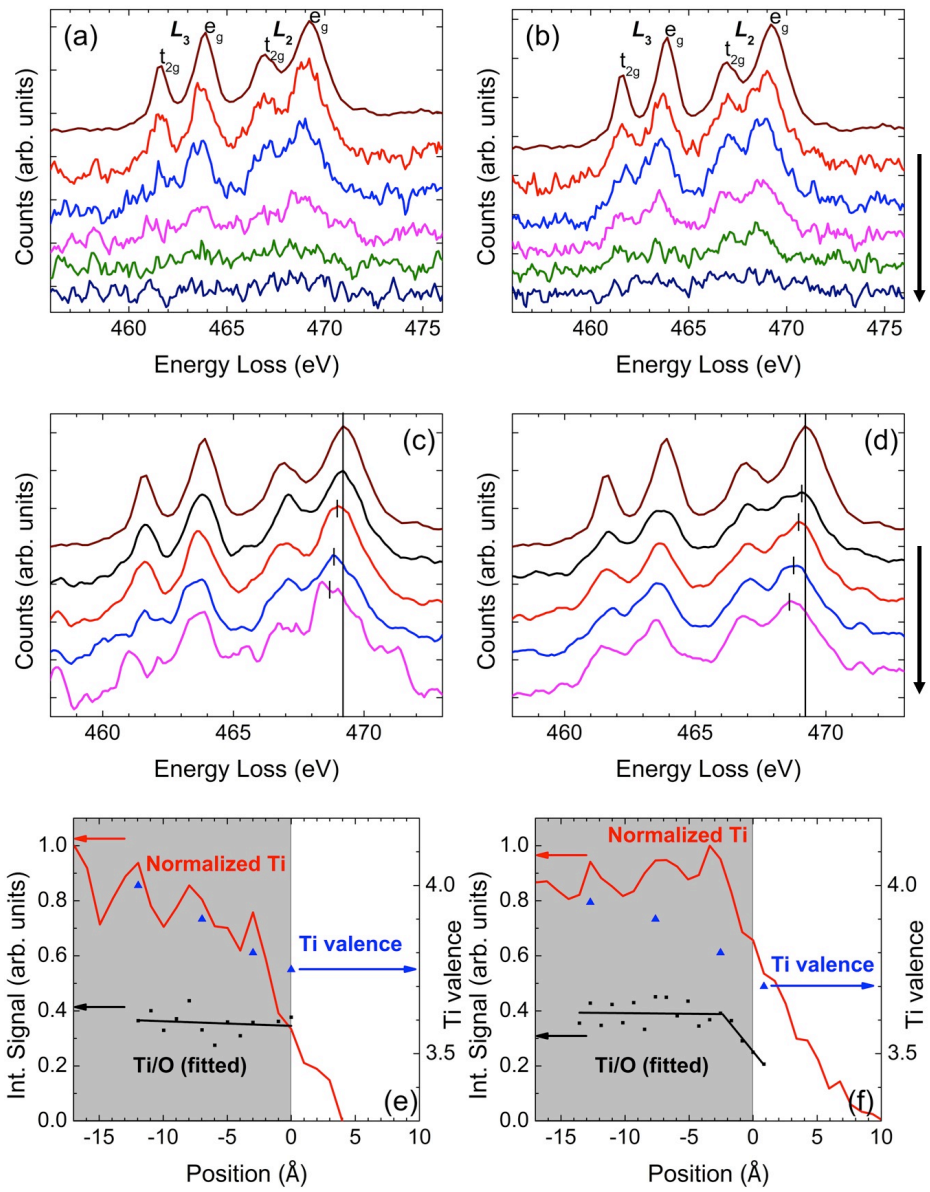

Figure 3.2 Background subtracted Ti *L*-edges of (a) Sample 1 and (b) Sample 2. The top spectrum is taken from bulk $SrTiO_3$, each of the other colored spectra corresponds to the signal enclosed by the corresponding rectangle superimposed on the image in Figure 3.1. Ti *L*-edge fine structure spectra fitted to its second nearest neighbor and normalized for (c) Sample 1 and (d) Sample 2. (e) and (f) show the normalized intensity of Ti signal, the linearly fitted Ti/O ratio, and the quantified Ti valence of Sample 1 and Sample 2, respectively. The shaded area indicates the $SrTiO_3$ film

information of the enclosed area. Figure 3.2(a) and (b) shows the background subtracted Ti *L*-edge fine structure of the $SrTiO_3$/GaAs interface with and without Ti pre-layer, respectively. The crystal field splitting of Ti L_3 and L_2 edges can be resolved, which is similar to the reported Ti^{4+} fine structure.[137] However, it is worth noticing that both the L_3 and L_2 edges are shifted to lower energies. As demonstrated earlier, such a chemical shift indicates a decrease of the Ti valence,[137, 138] in this case toward the interface.

Each of the acquired Ti *L*-edge fine structure spectra is then fitted to its second nearest neighbor and normalized in Figure 3.2(c) for sample 1, and in Figure 3.2(d) for sample 2. I compare the Ti *L*-edge spectra acquired across the interface with the previous result acquired from bulk $SrTiO_3$[92, 139] in order to quantify the Ti valence change at the interface. In Figure 3.2(c), the film deposited with the Ti pre-layer, both the Ti L_3 and L_2-edges shift to lower energies as the electron probe approaches the interface from the $SrTiO_3$ film, indicating a decrease of the Ti valence from 4+ to a mixture of 3+ and 4+.[137] This decrease in Ti valence could be due to either the increased presence of interfacial oxygen vacancies, or because the Ti-O bonding state on the TiO_2 columns in the thin film changes to Ti-As on the surface of the substrate. The chemical shift of Ti L_2-edge is marked in the figure, and quantified assuming a linear relationship between the Ti valence and the L_2-edge chemical shift.[138] The same method is used in the valence quantification for sample 2, where a decrease in the Ti valence is also measured as a function of distance from the hetero-interface.

In Figure 3.2(e) and (f), the normalized intensity of Ti signal are obtained by integrating the background subtracted Ti L_3 and L_2-edges in the energy range of 455-475 eV. The shaded area indicates the $SrTiO_3$ film, while the white area indicates the GaAs

substrate. This Ti intensity oscillates according to the atomic structure of the $SrTiO_3$ film layer-by-layer, but exhibits a reduction at the interface. However, the Ti signal remains detectable ~0.4 nm into the substrate GaAs in sample 1, ~0.7 nm in sample 2. The presence of the Ti signal in the GaAs substrate demonstrates that Ti diffuses into the first few monolayers of GaAs regardless of the thin film growth condition.

The integrated Ti/O-signal ratio is also measured and linearly fitted for both samples, using and energy window between 530 eV and 550 eV for the O *K*-edge. It is interesting to notice that the Ti/O ratio in sample 1 remains steady, but shows a significant decrease at the interface of sample 2. Such a change in sample 2 (i.e. the sample without the Ti prelayer) indicates a reduction of Ti concentration at the interface, which supports the fact that there is no interfacial Ti pre-layer and Ti diffuses further into the subsurface GaAs than in sample 1, thereby leaving behind a Ti poor layer of $SrTiO_3$ at the GaAs interface.

As mentioned above, the Ti valence exhibits a decrease from the film to the interface in both samples, suggesting an increase of oxygen vacancy concentration from the film to the interface, and/or a different bonding state at the $SrTiO_3$/GaAs interface. By comparing the Ti valence at equal distances from the interface for both films, I find that in sample 2 the $SrTiO_3$ film is more oxygen deficient than in sample 1. The fact that sample 2 has more oxygen vacancies in the film, but lower Ti/O-intensity ratio at the interface can be understood if one assumes that O is bonded with As rather than Ti at the interface. This would explain the increased presence of oxygen at the hetero-interface as well as the oxygen deficiency in the $SrTiO_3$ film of sample 2 compared to that of sample. These interpretations are consistent with some of the earlier studies on the oxidation of

GaAs substrates, which attributed Fermi level pinning to arsenic oxides at the interface.[140-142] Moreover, in previous studies, where thermal reactions in the Ti/GaAs system were studied to understand the metallization of the semiconductor surface, it was found that interfacial layers consisting of Ti-Ga and Ti-As are formed on the Ti film surface.[62, 143, 144]

In Figure 3.3(a) and (b), the acquired O *K*-edges (obtained from the same positions as the Ti *L*-edges) are fitted to their 5th nearest neighbors for sample 1 and 2, respectively, and compared with the previous results of bulk $SrTiO_3$. The colored spectra correspond to the colored rectangles in Figure 3.1(a) and (b), while the black arrow indicates the scan direction. In contrast to the Ti-intensity, the oxygen signal becomes undetectable at the interface between the ultrathin film and the substrate, while the Ti signal remains observable, as shown in Figure 3.2(a) and (b). It is clearly noticeable from the O *K*-edge spectra that the electronic structures at the interface in sample 1 and sample 2 are different. More specifically, in sample 1 (with the Ti pre-layer), all three spectra in the film bear the same features, similar to the O signal acquired in bulk $SrTiO_3$, shown on the top of Figure 3.3(a). In sample 2 (without Ti pre-layer), a new peak arises at 536 eV in the O *K*-edge fine structure at the interface, and disappears after two unit cells into the film. This new peak suggests a change in the coordination of O at the interface of sample 2, compared to that in bulk $SrTiO_3$, which I attribute to the formation of As-O bonds. This suggestion is consistent with our observations on O and Ti concentrations, and Ti/O intensity ratios, mentioned earlier. First principles calculations summarized below provide further evidence the validity of this suggestion.

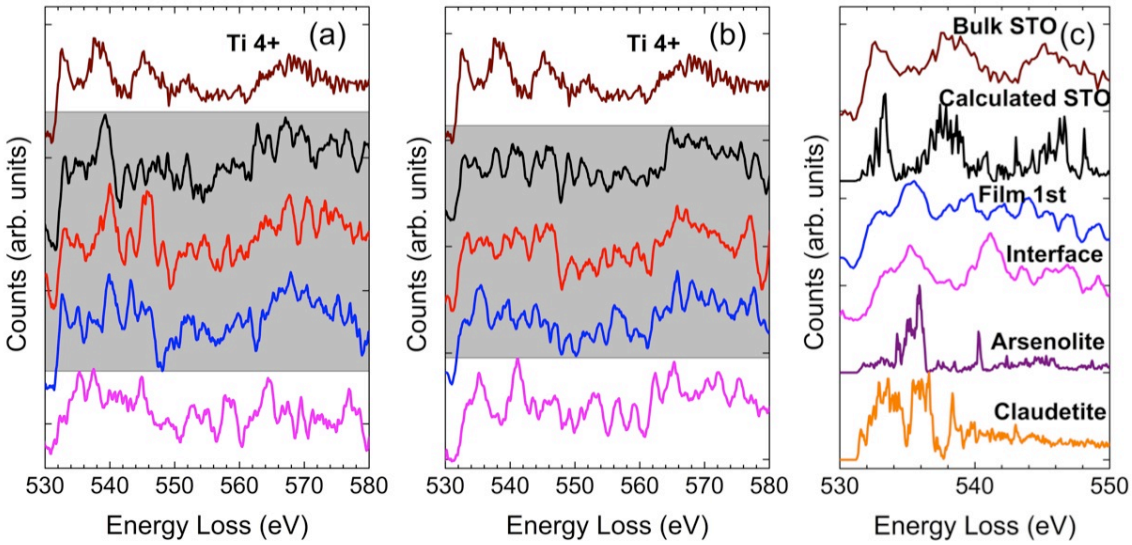

Figure 3.3 O *K*-edges of (a) Sample 1 and (b) Sample 2 (obtained from the same positions as the Ti *L*-edges) fitted to their 5th nearest neighbors and compared with the previous results on bulk $SrTiO_3$. The shaded area indicates the $SrTiO_3$ film. (c) O *K*-edge and O 2p density of states in bulk $SrTiO_3$, O *K*-edges of Sample 2 films and O 2p density of states in As_2O_3

First principles calculations within the frame-work of density function theory (DFT) were performed on bulk $SrTiO_3$ and various As_2O_3 compounds in order to understand the emergence of this peak. The results are shown in Figure 3.3(c), where the computed O *2p* partial densities of unoccupied states are compared with the experimental EELS spectra. I note that the DFT calculations for bulk $SrTiO_3$ successfully capture all the main peaks observed in the experimental spectrum over a 20 eV energy range. Furthermore, the new peak observed at 536 eV in the $SrTiO_3$/GaAs interfacial spectrum agrees very wel with the features observed in As_2O_3, in its arsenolite and claudetite polymorphs. These findings strongly support our hypothesis, that As-oxides form at the interface in sample 2, which is responsible for the measure Fermi-level pinning.

By combining these experimental results with the previous studies on the thermal reactions in the metallization and oxidation of GaAs, a likely scenario of the metal-oxide thin film deposition can be summarized as follows: In sample 1, after the Ti pre-layer deposition at approximately 300 °C, Ti breaks up the As dimers on the GaAs (2×4)-β2 surface,[145] and eliminates the surface reconstruction of the substrate. The resulting Ti-As bonds shift the As 3d core-level position and induce Fermi level pinning. After the oxide growth temperature is increased to 550 °C to improve the crystallinity of the $SrTiO_3$ film, the surface-bonded Ti penetrates into the substrate, which alleviates the Fermi level pinning. In sample 2, without the presence of the Ti pre-layer, the As surface layer gets oxidized when the $SrTiO_3$ deposition begins, and these arsenic oxides at the interface are responsible for the Fermi level pinning. This is also the reason for the observed differences in the O *K*-edge fine structure at the $SrTiO_3$/GaAs interface in sample 2.

3.4 Summary

In summary, I have presented a combination of atomic-resolution Z-contrast imaging, atomic-column resolved EELS at 80 kV, and first-principles DFT studies to examine the atomic and electronic structures of the interface between single crystalline $SrTiO_3$ and semiconducting GaAs. As in previous studies, I have found no evidence of a Ti pre-layer or any reconstruction on the GaAs side of the interface after the thin film deposition using Z-contrast imaging. Our present atomic-resolution EELS studies performed at 80 kV have indicated that Ti diffuses into subsurface GaAs, the extent of which depends on the film growth conditions. Furthermore, our detailed analysis of the near-edge fine structure as a function of position from the interface has revealed a shift toward lower energies in the Ti $L_{2,3}$ edges near the $SrTiO_3$/GaAs interface and different bonding configurations, supported by first-principles DFT calculations, at the interface resulting from different growth methods. Our results strongly suggest that although it does not affect the cationic arrangement at the interface, the Ti pre-layer deposition alleviates the oxidation of the substrate and consequently the Fermi level pinning at the interface, an effect of which will be essential in further improving the performance of single crystal oxides in MOSFET devices.

CHAPTER 4

EFFECT OF STOICHIOMETRY AND IMPURITY ON GAAS: FILM GROWTH AND DEFECT FORMATION

4.1 Introduction

The significance of the stoichiometry has been appreciated in many studies, as it plays an important role in determining the structural stability of many material systems [61, 65, 135, 146, 147]. In bulk STO, it was found that SrO-terminated surface has lower surface energy under most chemical environments [146]. In GaAs, surface reconstructions can be controlled by stoichiometry and temperature, and the existence of different reconstructions and the transitions between them have been predicted theoretically and observed experimentally [38, 41, 43, 53, 60, 136]. Among all the reconstructions of GaAs (100) surfaces, β2-(2x4) and c-(4x4) were reported as the most energetically favorable structures in the As-rich environment, and the transformation between them was observed by controlling As flux [60]. Using GaAs as substrate for growing STO requires As-rich environment to remove native oxide, thus leaving the surface with β2-(2x4) or c-(4x4) reconstruction, depending on the As flux [28, 148]. In addition, earlier studies of the growth of Ti thin film on GaAs shed light on the reaction between Ti and GaAs in forming Ti/Ti_xGa_{1-x}/TiAs/GaAs layered structures where Ti replaces Ga atoms while forming bonds with As atoms [62-64, 143].

In the previous chapter, I showed that (i) STO films grown on GaAs with different growth conditions exhibit identical interfacial structures, (ii) GaAs surface reconstructions were eliminated after film deposition, and (iii) Ti signal was found in subsurface GaAs, indicating reaction with and diffusion into surface GaAs. In this Chapter, I will present and discuss my first principles calculations on several aspects of STO/GaAs system. I will show that stoichiometry of STO film is essential in determining the interfacial atomic structure, and that SrO-terminated film exhibits lowest relative formation energy within a wide range of chemical potential. I will also argue that the removal of GaAs surface reconstruction should be attributed to Ti adatoms, which are adsorbed by the GaAs substrate and diffuse into subsurface. Finally, I will discuss the preferred configurations of GaAs (bulk and surface) with Ti impurities in light of the experimental findings.

4.2 Computational Methods and Parameters

All calculations were performed within the framework of density functional theory (DFT) using the projector augmented wave method as implemented in the Vienna Ab initio Simulation Package (VASP) code with local density approximation [106, 107, 122, 149]. The optimized lattice constant I obtained for bulk GaAs is 5.627 Å, which is used for all the calculations when GaAs is present. The calculated lattice constant of bulk STO is 3.865 Å, but for ultrathin STO film on GaAs, I used 3.979 Å for STO to match the lattice parameter of (substrate) GaAs.

To examine the structural energetic of the STO/GaAs interface, symmetrical slabs with 1x1 surface cells were employed to eliminate the net dipole moment in the supercell. In this symmetrical slab, there are 8 layers of As and 7 layers of Ga, and 4 unit cells of

STO films are in contact with the As-terminated substrate on both interfaces. The vacuum inserted between two unit cells is 8 Å, which is large enough to prevent any interaction between STO films. I used an energy cutoff of 400 eV and an 8x8x1 Monkhorst-Pack grid for **k**-point sampling. In order to check convergence with respect to various parameters, I repeated all the calculations by changing one parameter at a time: The number of STO unit cells was increased to 8; number of As and Ga layers to 13 and 12, respectively; and the vacuum region to 14 Å. No significant changes were observed in the relative energy difference between various structural forms.

For Ti adsorption and diffusion calculations, GaAs (100) β2-(2x4) surface reconstruction was considered with an asymmetric slab in which the bottom layer Ga atoms were passivated by pseudo-hydrogen atoms (of nuclear charge Z=1.25). Due to computational demand, in this case I used an energy cutoff of 250 eV for structural relaxation and total energy calculation. For **k**-point sampling, I used a 4x2x1 Monkhorst-Pack grid for a β2-(2x4) surface and a 2x2x1 grid for a doubled β2-(2x4) surface.

For Ti impurity calculations, I used an energy cutoff of 250 eV in all calculations. For the case of bulk impurities, I used a 3x3x3 supercell (a total of 108 atoms) and a **k**-point grid of 2x2x2. For the case of Ti impurities near the GaAs (100) surface, I used an asymmetric slab (again passivated by pseudo-hydrogens at the bottom layer) with a 2x2 surface unit cell, and a 4x4x1 **k**-point grid.

4.3 Results

4.3.1 STO/GaAs Stoichiometry

In order to understand the interfacial registry, I performed calculations on various interfacial configurations including stoichiometric and nonstoichiometric STO films with

SrO or TiO_2 layer in contact with surface As. Figure 4.1 shows different configurations of 4-unit cell stoichiometric STO film starting with SrO layer. Among these different interfacial configurations, ST3 has the interfacial registry identical to what was observed experimentally [29, 150], and the lowest total energy compared to the other configurations. Figure 4.2 shows different configurations of STO film starting with TiO_2 layer, among which TS1 and TS2 both have interfacial bonding between As and first layer perovskite. Compared to TS2 which only has As-Ti bond, TS1 also has As-O bond and smaller interfacial distance. Nonstoichiometric STO films are plotted in Figure 4.3 with As-SrO interfacial registry and in Figure 4.4 with As-TiO_2 interfacial registry. SS1-SS4 have the same interfacial configuration as ST1-ST4, respectively, but the film ends up with an extra SrO layer. From the relaxed structure, it seems that the stoichiometry of the film does not alter the interfacial structure, but total energy calculations show significant difference between stoichiometric and nonstoichiometric films. Similarly, TT1-TT4 have identical interfacial structure as TS1-TS4 but with an extra TiO_2 layer ending the film, as shown in Figure 4.4.

I then performed first principles total energy calculations on all of these configurations in order to find the most energetically favorable interfacial structure. To obtain the interfacial formation energy, I took into consideration the stoichiometry of the film. The total energy for a given interface configuration can be written as [38]

$$E_{interface} = E_{slab} - n_{Ga}\mu_{Ga} - n_{As}\mu_{As} - n_{SrO}\mu_{SrO} - n_{TiO2}\mu_{TiO2}, \quad (4.1)$$

where E_{slab} is the total energy of the corresponding double slab, n_i is the number of atoms/units of type i in the slab, and μ_i's are the corresponding chemical potentials, which satisfy $\mu_{Ga} + \mu_{As} = \mu_{GaAs}$ and $\mu_{SrO} + \mu_{TiO2} = \mu_{STO,bulk}$. From the upper limits

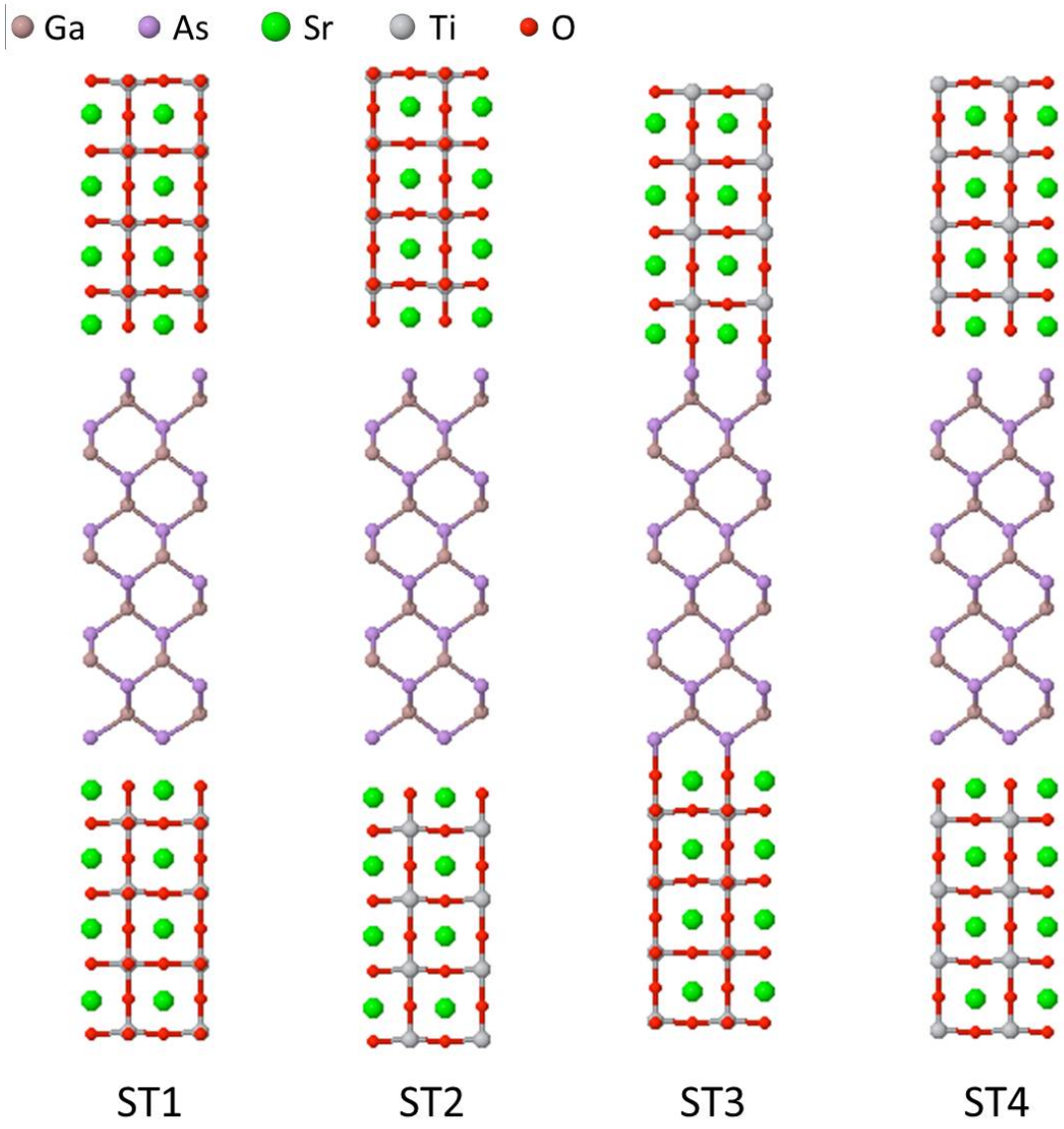

Figure 4.1 STO/GaAs double slab with 4 unit cells of STO on each side, the stoichiometric films start with SrO layer and terminate with TiO_2 layer.

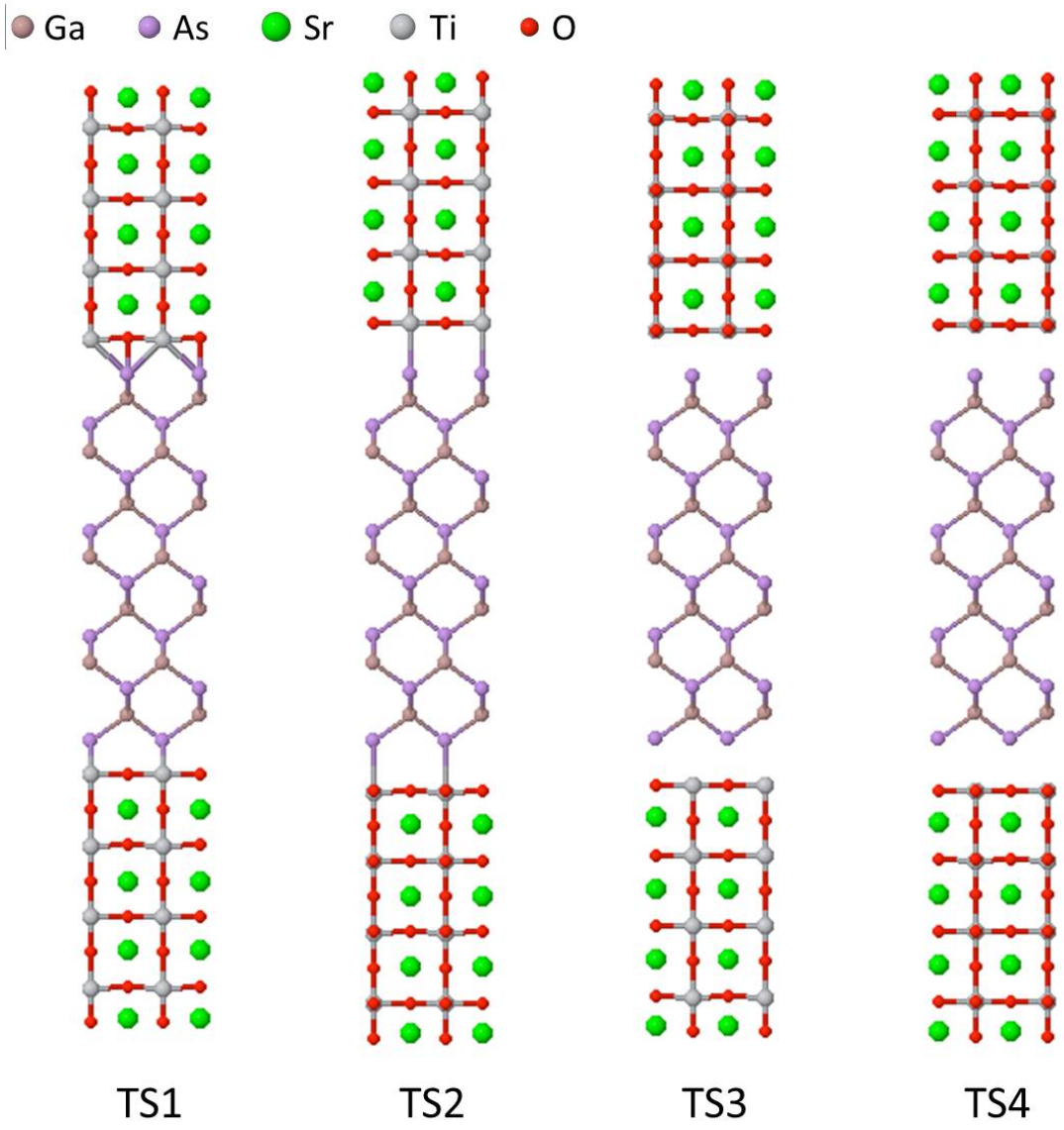

Figure 4.2 STO/GaAs double slab with 4 unit cells of STO on each side, the stoichiometric films start with TiO_2 layer and terminate with SrO layer.

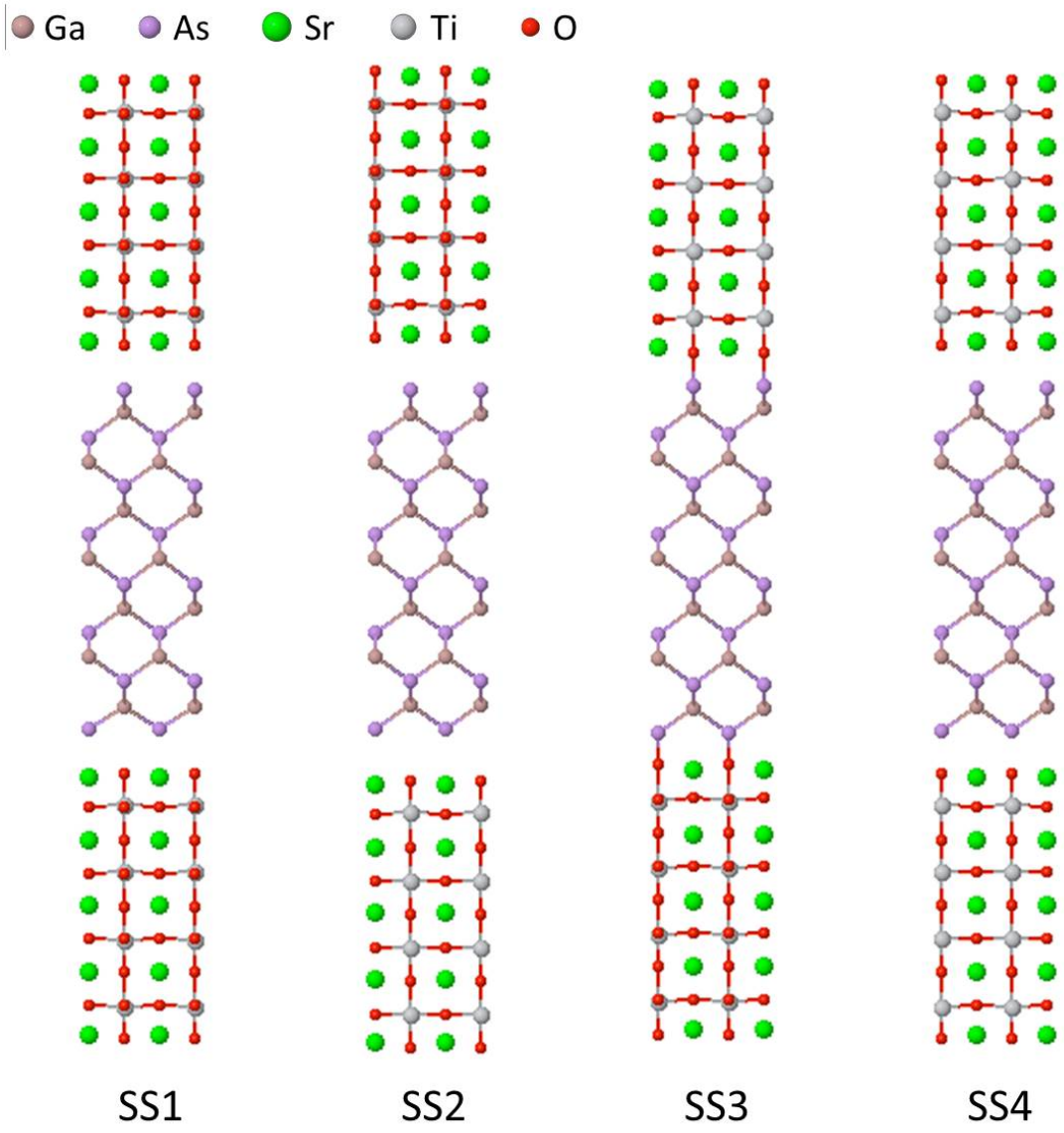

Figure 4.3 STO/GaAs double slab with 4.5 unit cells of STO on each side, the nonstoichiometric films start with SrO layer and terminate with SrO layer.

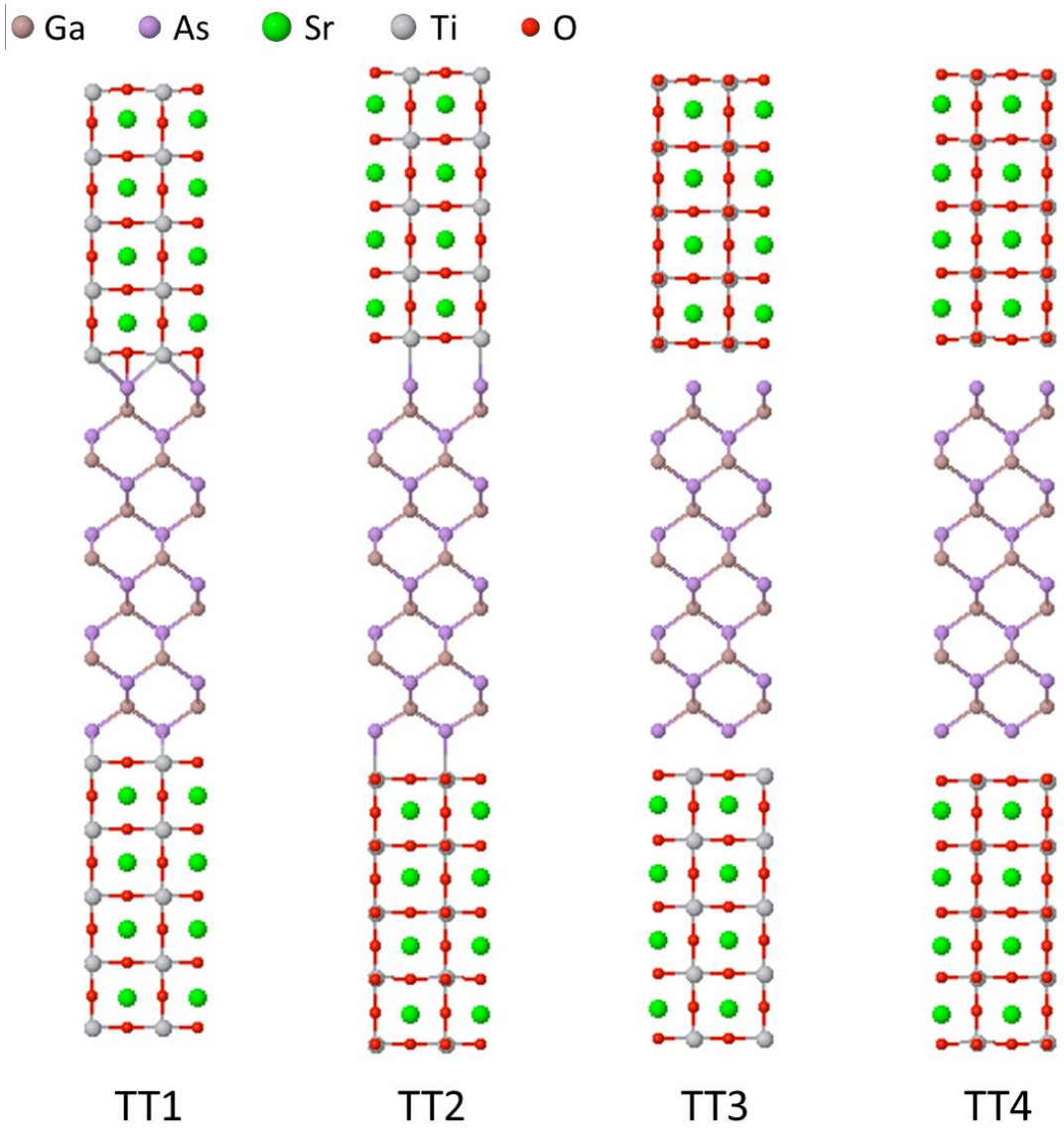

Figure 4.4 STO/GaAs double slab with 4.5 unit cells of STO on each side, the nonstoichiometric films start with TiO_2 layer and terminate with TiO_2 layer.

on the SrO and TiO_2 chemical potentials ($\mu_{SrO} \leq \mu_{SrO,bulk}$ and $\mu_{TiO2} \leq \mu_{TiO2,bulk}$) I find the allowed range of μ_{TiO2} to be $-30.70\ eV \leq \mu_{TiO2} \leq -29.30\ eV$.

Figure 4.5 shows the total energy expressions per (1x1) interface unit cell for all interfacial configurations with different stoichiometry. As-SrO interfaces are plotted in black (ST1 and SS1), red (ST2 and SS2), blue (ST3 and SS3) and olive (ST4 and SS4). As-TiO_2 interfaces are plotted in grey (TS1 and TT1), magenta (TS2 and TT2), cyan (TS3 and TT3) and green (TS4 and TT4), respectively. Due to the presence of extra SrO or TiO_2 layer, nonstoichiometric films render a non-zero slope (+/- 1) in the figure while stoichiometric films have constant energy. The energy of configuration TS2 was set to 0 eV as a reference. One can observe that in the allowed range of TiO_2 chemical potential, stoichiometric As-SrO films (ST1-ST4) have similar energies around 0 eV, while stoichiometric As-TiO_2 films (TS1-TS4) have energies at 0 and ± 0.3 eV. Nonstoichiometric As-TiO_2 films (TT1-TT4) have highest energies in the TiO_2 poor region, although TT1 has the lowest energy in the TiO_2 rich region. When TiO_2 chemical potential starts to decrease, TT1-TT4 systems become overwhelmingly high in energy. Nonstoichiometric As-SrO films (SS1-SS4) are energetically more favorable within a wide range of TiO_2 chemical potential. This figure indicates that STO/GaAs interface stability can be affected by configurations with surface As and different first oxide layers. In addition to the metal oxide – semiconductor interface, STO/vacuum interface plays an important role and determines the STO/GaAs interfacial configuration to be As-SrO, in agreement with the experimental observations.

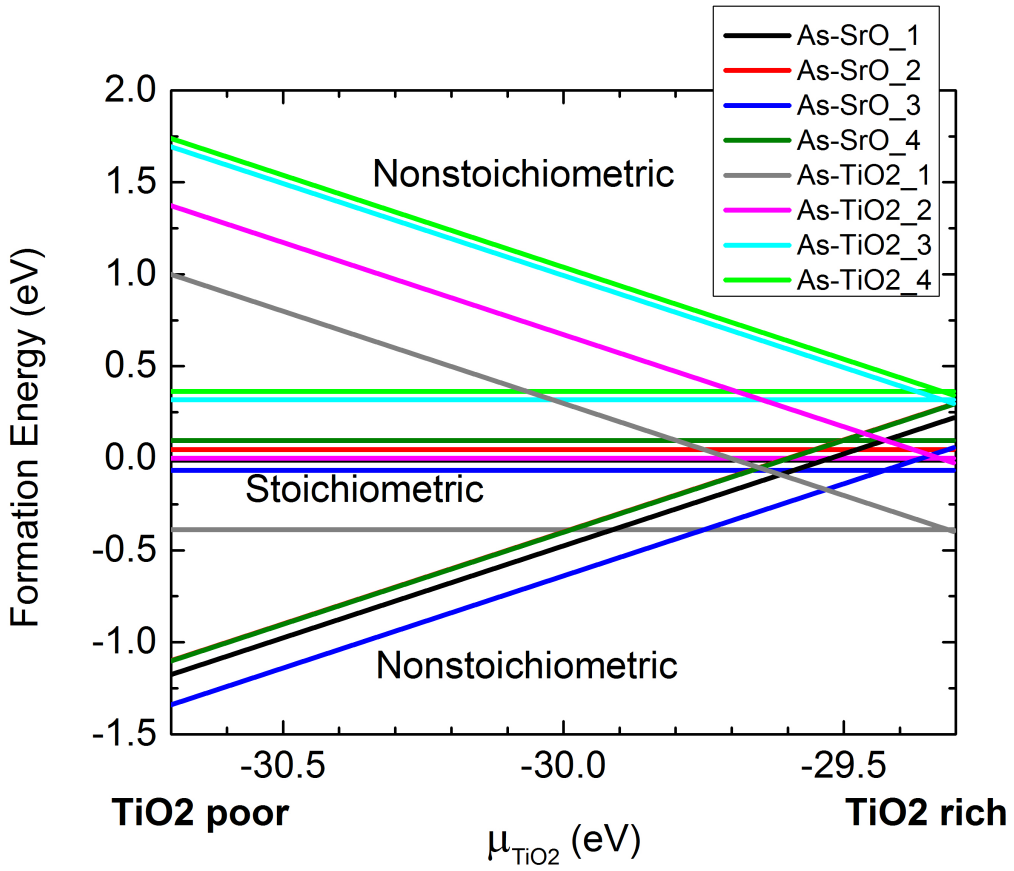

Figure 4.5 Relative interface formation energy as a function of TiO_2 chemical potential in different interfacial configurations. Stoichiometric films have constant formation energy; nonstoichiometric films have slopes of +/-1 with respect to TiO_2 chemical potential. Same interfacial registries are shown in the same color: As-SrO ST1 and SS1 in black; As-SrO ST2 and SS2 in red; As-SrO ST3 and SS3 in blue; As-SrO ST4 and SS4 in olive; As-TiO_2 TS1 and TT1 in grey; As-TiO_2 TS2 and TT2 in magenta; As-TiO_2 TS3 and TT3 in cyan; As-TiO_2 TS4 and TT4 in green.

4.3.2 Potential Energy Profile of Ti Adatoms on GaAs (100) Surface with a β2-(2x4) Reconstruction

In order to understand the effect of Ti pre-layer before STO film deposition, I performed first principles calculations for the structural energetics of a Ti adatom on the GaAs (100) surface with a β2-(2x4) reconstruction. I considered two different concentrations Θ of Ti adatoms Θ = ½ and Θ = 1. Figure 4.6 shows a doubled GaAs β2-(2x4) surface after structural relaxation. In order to get a contour map for the Ti binding energy, I divided the β2-(2x4) surface into a 5x10 grid; a 10x10 grid is shown on the doubled β2-(2x4) surface in Fig. 4.6.

For Θ = ½ coverage, I added one Ti atom onto a doubled β2-(2x4) surface. Due to the periodicity of the surface, the Ti adatom was placed at each of the fifty grid points on the left half of the doubled β2-(2x4) surface, followed by a structural relaxation and total energy calculation. Figure 4.7 shows the contour map for the binding energy of one Ti adatom on a doubled β2-(2x4) surface. The blue area indicates higher binding energy, hence energetically more favorable sites for Ti adatoms. The adsorption simulation was performed by constraining *x* and *y* coordinates of the Ti adatom and allowing *z* coordinate to relax. This was followed by a full structural relaxation starting with Ti atoms at the 8 positions with the highest binding energy in order to find the global minimum and the actual values of the binding energies. The 8 grid points with respect to the original 5x10 grid (shown in Fig. 4.6) have coordinates of (*x,y*) = (3,7), (3,9), (2,1), (2,5), (2,2), (2,4), (1,2), and (1,8). Figure 4.8 shows an 8x8 GaAs surface after structural relaxation where Ti was initially near sites (3,7), (3,9), (2,1) and (2,5). Near sites (3,7) and (3,9), one can notice that the presence of Ti adatom breaks the third-layer As dimer, and Ti bonds with

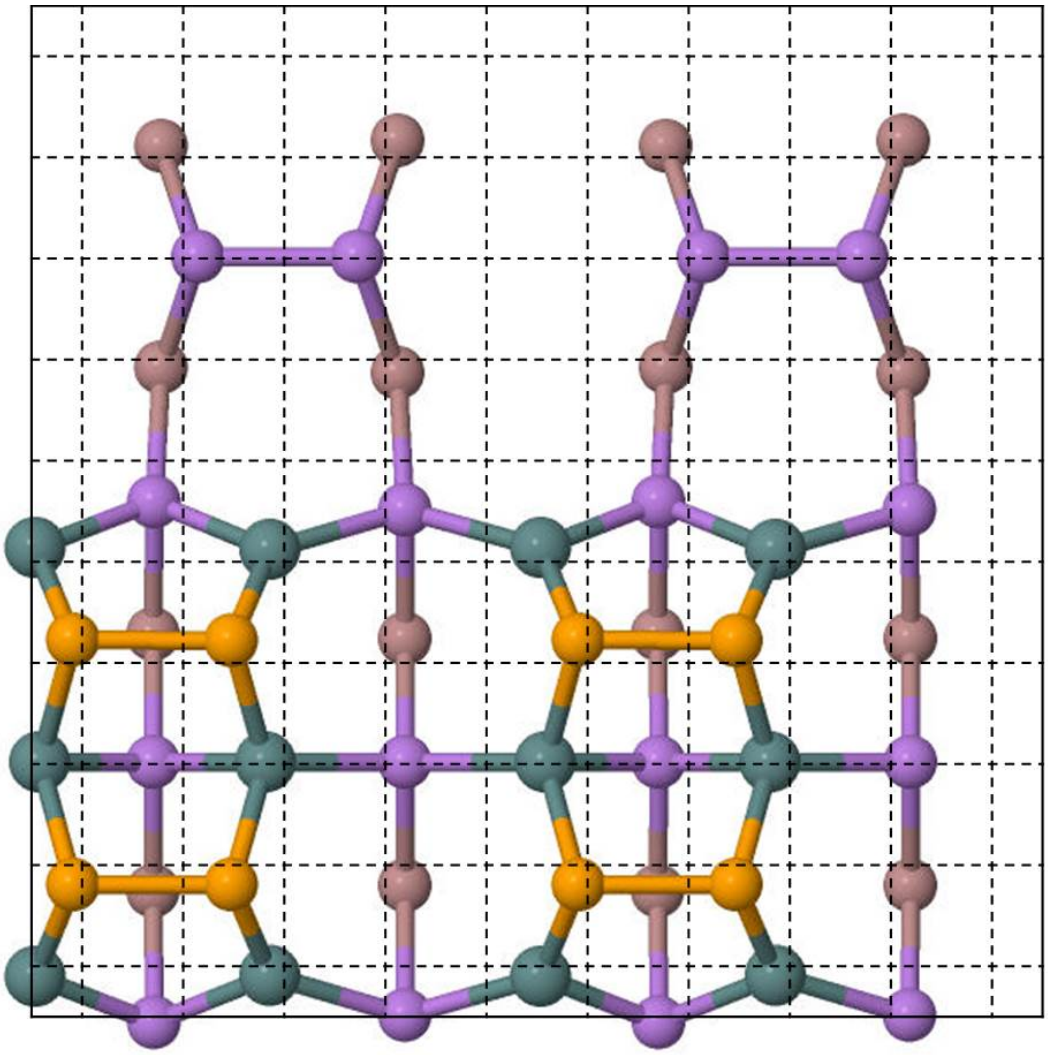

Figure 4.6 GaAs β2-(2x4) surface reconstruction, shown in a 4x4 surface cell. First As layer (yellow) has two As dimers, second Ga layer (green) has two Ga vacancies, third As layer (purple) has one As dimer, fourth Ga layer (beige) has no defects. The 2x4 surface is divided into a 5x10 grid for Ti adsorption calculation

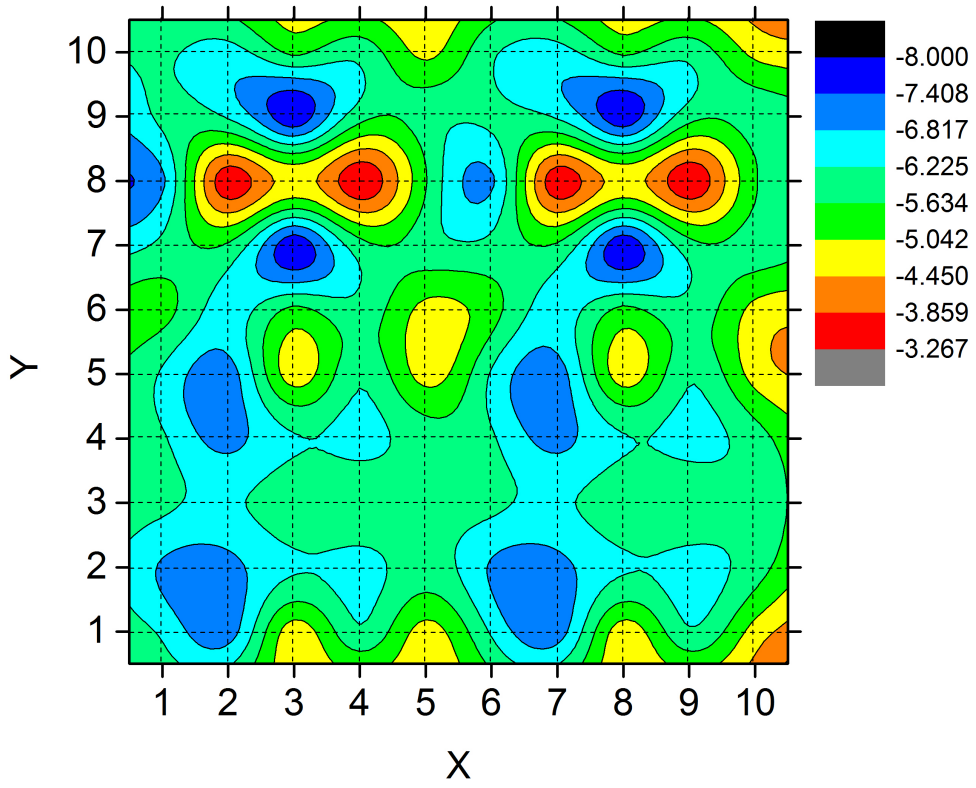

Figure 4.7 Contour map for the binding energy of the Ti adatom on the GaAs (100) surface with a β2-(2x4) surface reconstruction, at a coverage of Θ = ½. A 4x4 surface cell is shown. Highest binding energy is shown in dark blue.

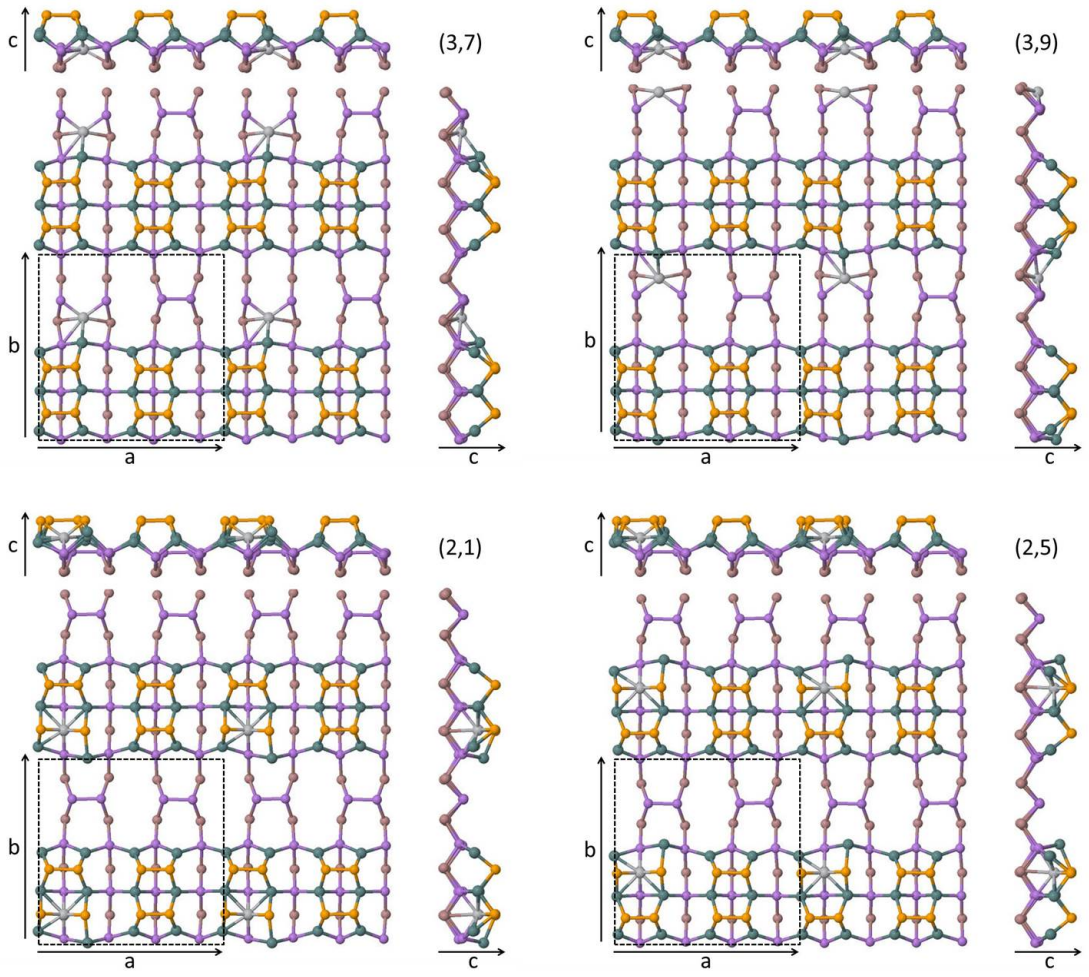

Figure 4.8 GaAs 8x8 surface cell after full structural relaxations starting with Ti adatoms near the given grid points. The 4x4 surface cell of dimension (axb) used in calculation is shown with the dotted line. Cross-sectional views are shown on top and right which denote the diffusion depth.

neighboring third-layer As and fourth-layer Ga atoms. A side view shows that Ti adatoms sinks into third-layer As, as observed experimentally from EELS in the previous Chapter. Near sites (2,1) and (2,5), Ti adatom breaks one top-layer As dimer and stays at the center of the broken dimer. It diffuses into the second layer and bonds with three of the second-layer Ga and two of the top-layer As atoms. Figure 4.9 shows the other four sites after the full structural relaxations. Among these, Ti near site (2,2), (2,4), and (1,2) breaks one top-layer As dimer, and bonds with three top-layer As and one second layer Ga atoms. Near site (1,8), Ti adatom was placed between two of the third-layer As dimers before structural relaxation. After full relaxation, Ti breaks its neighboring As dimers and bonds with two As atoms next to it, and the two As atoms form another dimer to compensate their dangling bonds. It is also interesting to observe that Ti sinks into the fourth layer and bonds with four Ga atoms.

For $\Theta = 1$, I took the β2-(2x4) surface and placed one Ti atom onto each of the 50 grid points. Figure 4.10 shows the contour map for the binding energy of the Ti adatom. The 8 sites with the highest binding energies in this case are (4,2), (4,4), (4,3), (2,3), (3,7), (3,9), (1,7), and (1,9). Starting with the Ti adatom at these high-binding energy sites, I performed a full structural relaxation. The upper panel in Figure 4.11 shows a 4x8 GaAs surface after structural relaxation, with Ti adatom near sites (4,2), (4,4), (4,3) and (2,3). Near the most energetically favorable sites (4,2) and (4,4), Ti breaks its neighboring As dimers and sinks into the second layer, forming bonds with three Ga atoms in the second layer and two As atoms in the top layer. The grid points (4,3) and(2,3) correspond to interstitial sites of the top-layer As atoms, where Ti adatom breaks both dimers and bonds with four surrounding As atoms and one of the Ga atoms in the

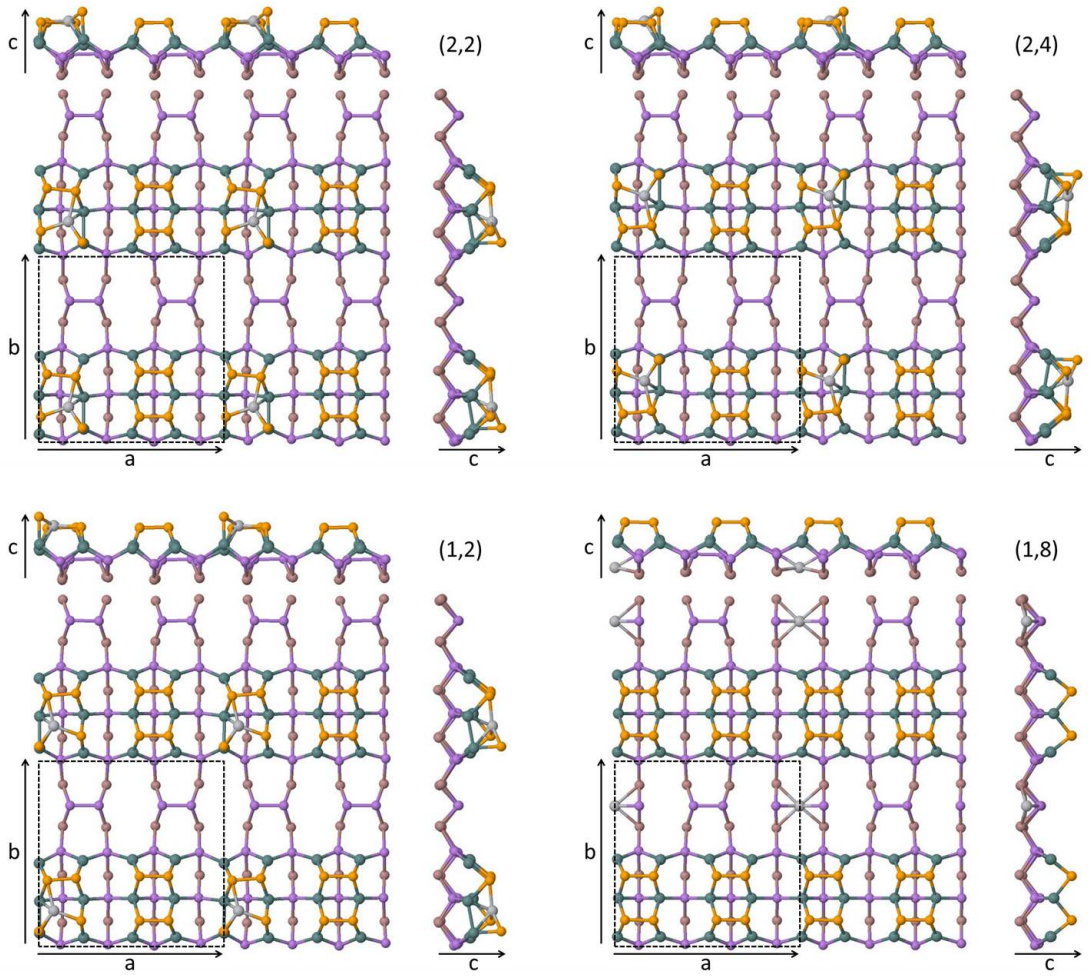

Figure 4.9 GaAs 8x8 surface cell after full structural relaxations starting with Ti adatoms near the given grid points. The 4x4 surface cell of dimension (axb) used in calculation is shown with the dotted lines. Cross-sectional views are shown on top and right which denote the diffusion depth.

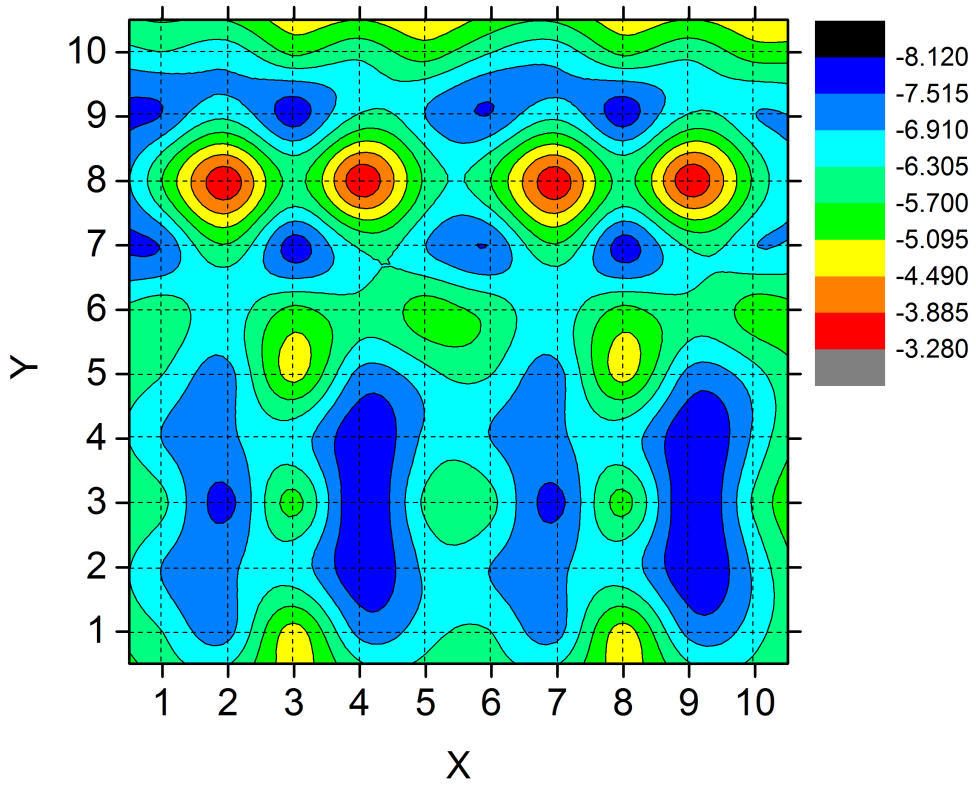

Figure 4.10 Contour map for the binding energy of a Ti adatom on the GaAs (100) surface with a β2-(2x4) surface reconstruction, at a coverage of Θ = 1. A 4x4 surface cell is shown. Highest binding energy is shown in dark blue.

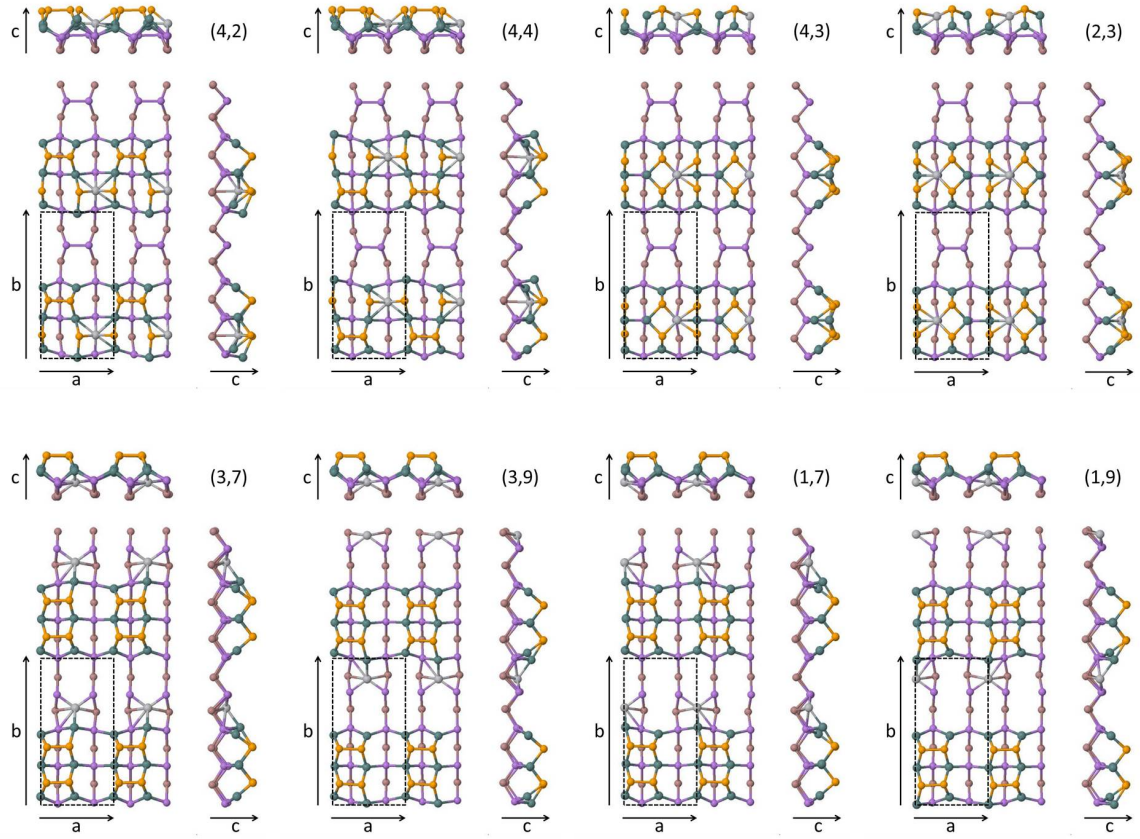

Figure 4.11 GaAs 4x8 surface cell after full structural relaxations starting with Ti adatoms near the given grid points. The 2x4 surface cell of dimension (axb) used in calculation is shown with the dotted lines. Cross-sectional views are shown on top and right which denote the diffusion depth.

second layer. On these interstitial sites, Ti atom stays in the top layer as observed from the side-view model. In the lower panel of Figure 4.11, the relaxed structures near the other four sites are shown. At all these sites, Ti adatom breaks the As dimer in the third layer, bonds with three As atoms in the same layer, two Ga atoms in the fourth layer, one Ga atom in the second layer, and diffuses into the third layer.

Table 4.1 shows the binding energies for the Ti adatom on the GaAs (100) surface with an initial β2-(2x4) surface reconstruction. For $\Theta = ½$, sites near (2,1) and (2,5) have highest binding energies which correspond to the Ti adatom being placed on top of one of the top-layer As dimers. The Ti adatom diffuses into the second layer by breaking the dimer and donating electrons to compensate the dangling bonds. For $\Theta = 1$, sites near (4,2) and (4,4) have highest binding energies which correspond to the Ti adatom being placed in line with two top-layer As dimers. The adatom again diffuses into second layer while breaking its neighboring dimers and donating electrons. It is worth noticing that in both $\Theta = ½$ and $\Theta = 1$ coverage, the highest binding energy configuration results in the Ti adatom breaking the surface As dimers and sinking into second layer which consists of Ga atoms.

4.3.3 Ti Impurity in Bulk GaAs

In order to understand the behavior of Ti impurity in bulk GaAs, I also performed first principles calculations on bulk GaAs with Ti impurity atom at four different sites: Ti at an As site (Ti_{As}), Ti at a Ga site (Ti_{Ga}), Ti interstitial surrounded by 4 As atoms ($Ti_{I\text{-}As}$) and Ti interstitial surrounded by 4 Ga atoms ($Ti_{I\text{-}Ga}$). The Ti impurity concentration I considered here is one Ti atom per GaAs 3x3x3 supercell. The formation energy for a given configuration can be written as [38]

Site	E_{diff} (eV)	Site	E_{diff} (eV)
1,2	-7.18	1,7	-7.90
1,8	-7.72	1,9	-7.90
2,1	-8.16	2,3	-8.13
2,2	-7.22	3,7	-7.90
2,4	-7.22	3,9	-7.90
2,5	-8.16	4,2	-8.29
3,7	-7.99	4,3	-8.13
3,9	-7.99	4,4	-8.29

Table 4.1 Binding energies of the Ti adatom after full relaxations starting from the positions given by (*x,y*) their coordinates with respect to the grid shown in Fig. 4.6. Two coverages with Θ = ½ (left) and Θ = 1 (right) are considered. Eight sites with the highest binding energies are listed.

$$E_{impurity} = E_{supercell} - n_{Ga}\mu_{Ga} - n_{As}\mu_{As} - n_{Ti}\mu_{Ti,} \tag{4.2}$$

where $E_{supercell}$ is the total energy of the GaAs supercell with the Ti impurity, n_i is the number of atoms of type *i* in the slab, and μ_i's are the corresponding chemical potentials, which satisfy $\mu_{Ga} + \mu_{As} = \mu_{GaAs}$. From the upper limits on the Ga, As and Ti chemical potentials ($\mu_{Ga} \leq \mu_{Ga,bulk}$, $\mu_{As} \leq \mu_{As,bulk}$,$\mu_{Ti} \leq \mu_{Ti,bulk}$) I find the allowed range of μ_{Ga} to be $-4.25\ eV \leq \mu_{Ga} \leq -3.60\ eV$. Figure 4.12 shows relative formation energy of Ti impurity in GaAs 3x3x3 bulk. One sees that within the allowed range of μ_{Ga}, Ti at a Ga site (Ti_{Ga}) has significantly lower formation energy than other configurations.

Given that Ti impurity atoms prefer to replace Ga atoms, I then proceeded to study the effect of Ti impurity depth near the (100) surface of GaAs. I considered an As-terminated GaAs (100) surface with a 2x2 surface unit cell, and introduced different concentrations of Ti impurities in the second and fourth (Ga) layers. The concentrations I calculated were $\Theta = 1/4$, $\Theta = 1/2$, $\Theta = 3/4$ and $\Theta = 1$ per 2x2 surface. For $\Theta = 1/4$, one Ti atom was placed in the subsurface GaAs (second or fourth layer) to replace one Ga atom, and two configurations were considered. For $\Theta = 1/2$, two Ti atoms replaced two Ga atoms in the second or fourth layer, which result in seven different configurations of Ti_{Ga}. For $\Theta = 3/4$, there are four configurations, in which three Ga atoms from the second and fourth layers were replaced by Ti impurities. For $\Theta = 1$, four Ti impurities combine in thirteen different ways to replace Ga atoms from the second and fourth layers. I compared the total energy of each of these configurations after structural relaxation, and found that Ti impurities in second layer render the lowest formation energy. The lowest energy configurations are shown in Figure 4.13. These findings are consistent with the Ti potential-energy profiles discussed earlier in the sense that Ti defects find their lowest energy configuration by replacing the Ga atoms closest to the surface.

4.4 Summary

This chapter described the computational results on STO/GaAs interface. Consideration of both film-substrate and film-vacuum interfaces validated the As-SrO interfacial registry, and rendered the lowest interface relative energy. Ti adatom was then added to the GaAs (100) β2-(2x4) reconstructed surface to find the favorable Ti positions and the resulting atomic structures. It was observed that the energetically most favorable configurations correspond to cases where the Ti adatoms break surface As dimers and

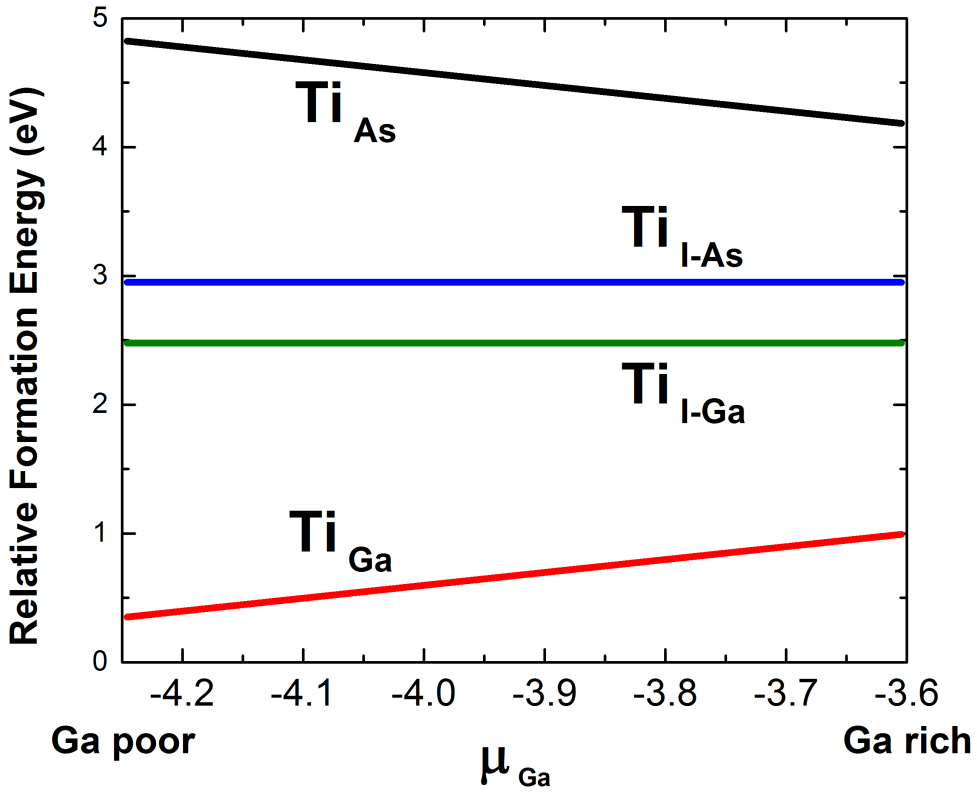

Figure 4.12 Relative formation energies for various Ti impurity configyrations: Ti at an As site (black); Ti at a Ga site (red); Ti interstitial surrounded by 4 As atoms (blue) and Ti interstitial surrounded by 4 Ga atoms (green).

sink into second layer Ga. I further demonstrated using calculations on Ti impurities in bulk GaAs that within the allowed range of Ga and As chemical potentials, Ti replacing Ga is the lowest-energy Ti impurity configuration. I then studied the diffusion depth of Ti impurities, and found the total energy increases when Ti penetrates further into the subsurface GaAs. My experimental findings discussed in the previous Chapter are explained quite well by these computational results, which lead to a fundamental understanding of the STO/GaAs interface.

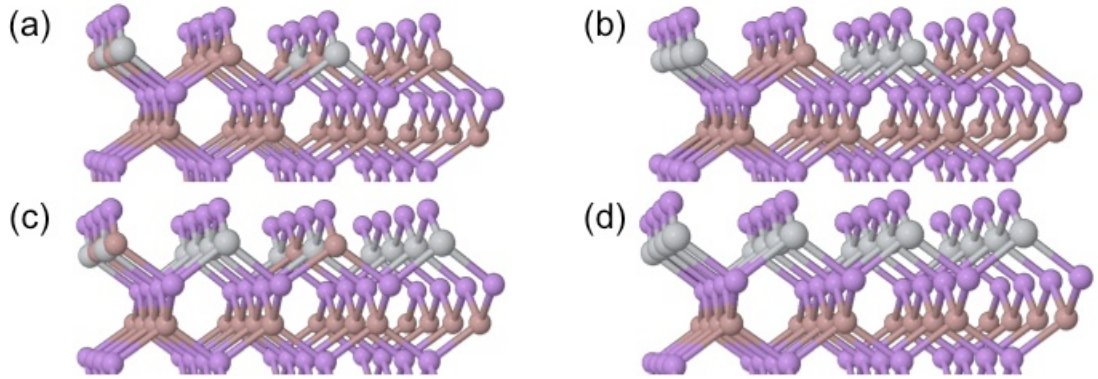

Figure 4.13 Lowest energy configurations of Ti_{Ga} with different Ti impurity concentrations: (a) $\Theta = 1/4$, (b) $\Theta = 1/2$, (c) $\Theta = 3/4$ and (d) $\Theta = 1$

CHAPTER 5

DIRECT OBSERVATION OF OXYGEN VACANCY AND FILM POLARIZATION ON $BaTiO_3/SrTiO_3/GaAs$

5.1 Introduction

Successful integration of perovskite oxide ultrathin film on semiconductor substrate has been achieved using molecular beam epitaxy in order to obtain an atomically sharp interface and novel interfacial properties [8, 151]. Comparing to the currently widely used Si substrate, III-V polar semiconductors exhibit much better electron mobility and velocity and thus can be implemented as a platform to accommodate metal oxide gate dielectric [28]. The metal oxide semiconductor system has also been recognized as a basis to grow functional oxides, producing multifunctional devices that can be carried on the semiconductor based electronic devices [126, 152]. Among the hurdles for such integration are the interfacial strain, oxygen vacancy, and polarity discontinuity which give rise to anomalous phenomena not observed in bulk materials [6, 18, 153].

Growth of epitaxial single-crystalline $BaTiO_3$ film has been successfully conducted on both polar and non-polar semiconductors, and can be a potential candidate for a new kind of nonvolatile transistor if the ferroelectricity is well preserved in the thin film [154]. However, in order to achieve crystallinity, as well as a polar axis normal to the interface, a buffer layer for strain relaxation is needed between the BTO film and GaAs

substrate [148]. Ultrathin $SrTiO_3$ layers grown on GaAs have been reported to be single-crystal, have atomically abrupt interface and appear free of interfacial defects. Furthermore, I have reported earlier that interfacial Fermi level pinning can be relieved with the deposition of 0.5 monolayer Ti pre-deposition, which is now used in the growth of functional oxides, such as BTO [29, 150].

Atomic-resolution high-angle annular dark field (HAADF) imaging has been utilized to study the interfacial structure of many functional oxide materials, however light elements, such as O cannot be routinely resolved using HAADF imaging. Recent instrumental developments have enabled a new imaging approach, called annular bright field (ABF) imaging, which now allows for the direct observation of elements, as light as hydrogen to be visible under the electron beam [94, 95, 155].

In this chapter, I report a detailed study of the atomic and electronic structures of the $BaTiO_3/SrTiO_3/GaAs$ heterostructure using a combined experimental and theoretical approach. More specifically, I use atomic-resolution imaging and spectroscopy in a STEM combined with first principles density functional theory (DFT) calculations to examine the effects of interfacial oxygen vacancies on the BTO film polarization. Our experimental results using both HAADF and ABF imaging clearly show the existence of oxygen vacancies at the interface between the STO buffer layers and the As-terminated GaAs substrate. Polarization in both the STO and BTO oxide layers is observed and quantified, showing an abrupt increase at the STO/BTO interface, but no evidence of ferroelectric domain. Electron energy loss spectroscopy (EELS) provides further support for the oxygen deficient GaAs/STO interface and the observed polarizations of the STO and BTO layers. DFT total energy calculations suggest an energetically favorable

STO/GaAs interfacial configuration with a high oxygen vacancy concentration. The following structural relaxation confirms that a large interfacial polarization is due to the presence of interfacial oxygen vacancies, and that the interface dipole is responsible for the inhibition of polarization switching. Orbital projected density of states (DOS) calculations are also included to help understand the electronic structure at the interface, which generates polarization and metallicity.

5.2 Methods

5.2.1 STEM Imaging and EELS Analysis

Cross-sectional TEM samples were prepared along the GaAs <110> and <100> directions in order to observe the atomic structure along the perovskite BTO/STO <100> and <110> directions. STEM image and EELS data were obtained using the aberration-corrected JEOL JEM-ARM200CF scanning transmission electron microscope. The microscope is equipped with a cold field-emission source, which yields an energy resolution of 0.35 eV; it allows for 78 pm spatial resolution at 200 kV with the probe spherical-aberration corrector. A convergence semi-angle of 22 mrad was used for both imaging and EELS. For HAADF imaging, a 90 mrad collection inner angle was used; for ABF imaging, 11-22 mrad collection semi-angle was used. For EELS, a convergence semi-angle of 45 mrad was used. EELS data in first and second TiO_2 layer were obtained from 2D mapping across the STO/GaAs interface and were integrated parallel to the interface to obtain TiO_2 column signals. EEL spectra in STO bulk and BTO film were obtained by overlapping multiple point scans. The experimental EELS data were then filtered using Multivariate Statistical Analysis to obtain a much better signal to noise ratio.

5.2.2 DFT Calculations

First principles calculations within the local density approximation were performed using the projector augmented wave method implemented in VASP [134]. I used a plane wave cutoff energy of 300 eV. Integrations in reciprocal space were performed by the Monkhorst-Pack scheme with a 4x4x1 mesh for BTO/STO/GaAs total energy calculation and structural relaxation, 8x8x2 mesh for BTO/STO/GaAs self-consistent and non-selfconsistent calculation, 20x20x20 mesh for STO bulk self-consistent and non-selfconsistent calculation. For BTO/STO/GaAs, I considered a 2x2 surface cell in order to include interfacial oxygen vacancy concentration Θ = 0, 0.25, 0.5, 0.75 and 1, with pseudohydrogen atoms to passivate the bottom layer of GaAs. Along the out-of-plane direction, the supercell consists of 6 Ga and 6 As atomic layers, 2 STO layers and 4-9 BTO stoichiometric and nonstoichiometric layers. DOS data were convoluted with Gaussian broadening in order to compare with the experimental spectra.

5.3 Results

5.3.1 Z-contrast and ABF Image

Figures 5.1a) and c) show a pair of simultaneously acquired HAADF and ABF images of BTO[100]/STO[100]/GaAs[110] while Figures 5.1b) and d) show a HAADF and ABF imaging pair of the BTO[110]/STO[110]/GaAs[100] interface. The atomically sharp interface consists of the As-terminated GaAs directly in contact with SrO-terminated STO buffer layer. The 12-fold coordinated cations in the perovskite-structured film changes from Sr to Ba after 2 unit cells and the film shows excellent epitaxy without defects and dislocations. The image intensity corresponding to the atomic number reveals that the substrate has one layer of As on top, while it had c-(4x4) surface reconstruction

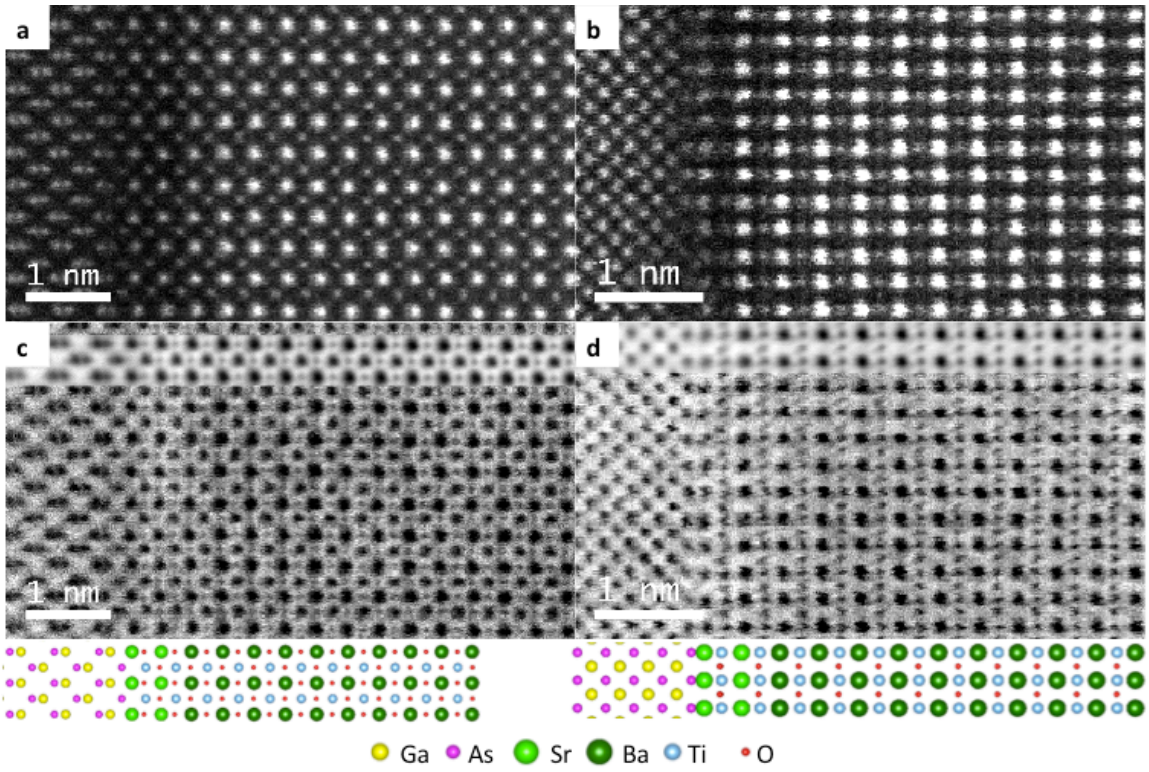

Figure 5.1 (a) HAADF and (c) ABF image of BTO[100]/STO[100]/GaAs[110]; (b) HAADF and (d) ABF image of BTO[110]/STO[110]/GaAs[100]

prior to the oxide film deposition [148]. As has been reported in many other studies, GaAs c-(4x4) surface reconstruction consists of two layers of As atoms on the surface;[54] however, our images shows that the GaAs substrate is terminated with one top layer As. It is not surprising that surface reconstruction disappears after film deposition begins, since the dangling bonds of the As surface are satisfied by adding new elements and breaking surface dimers. However, it remains unknown why only one layer of As atoms is present at the interface and how the As dimers evolve during film growth.

The corresponding ABF image of BTO[100]/STO[100]/GaAs[110] shows that the GaAs substrate is in contact with a highly oxygen deficient SrO layer, while the oxygen atoms are clearly shown in the rest of both the STO and BTO films. The oxygen deficiency in the first SrO layer induces a positive charge sheet, imposing an electric field away from the substrate. Also, from Figure 5.1d) one can observe Ti and O columns separately and notice a visible displacement between the positions of two elements, which should be in the same plane for bulk STO. The STO buffer layer has an out-of-plane lattice constant $a_{\perp}$, measured directly from the HAADF images, smaller than the in-plane lattice constant $a_{\parallel}$ and the tetragonality is attributed to the interfacial strain. By considering the lattice constants of GaAs (5.65 Å) and STO (3.905 Å), the perovskite film should experience a tensile strain when deposited onto the substrate with a 45° in-plane rotation, as observed in the images.

In order to obtain direct information from the ABF image, I took multiple slices from the raw image, cross-correlated and added them to get an averaged signal intensity for the entire image. In the averaged image in Figure 5.1(c), I performed an intensity scan across the interface on the Sr/Ba-O column and Ti-O column, as shown in Figure 5.2. From the

intensity scan one sees an As-terminated substrate in contact with a Sr-terminated STO buffer. The first atomic layer in the buffer is highly oxygen deficient, with no O signal intensity observable after the top layer As. Starting from the next TiO_2 layer, a visible O peak is present between its neighboring cations.

The lattice constant of each layer is measured and plotted in Figure 5.3a), which clearly shows that STO buffer layer undergoes a tensile strain and BTO film has an increased out-of-plane *c* axis. The displacement between Ti and O columns is found to be 0.069 Å in BTO film, with a positive polarization away from the substrate. Whereas in STO buffer layer, as seen in Figure 5.3b), the displacement is significantly larger than in BTO film. Considering the presence of tensile strain, STO is expected to have an in-plane polarization [18]. But the emergence of oxygen vacancies causes an out-of-plane electric potential that attracts the $[TiO_6]^{8-}$ octahedral shifting toward the interface [156]. The observed out-of-plane polarization thus rules out the possibility of strain-induced ferroelectricity in the STO buffer layer.

5.3.2 EELS

The Ti L_3 and L_2 edges were obtained from bulk STO, STO buffer layer and BTO film, as shown in Figure 5.4a). The O *K* edge onset in each spectrum was aligned to 532 eV for fine structure analysis. Ti L_3 and L_2 edges, also called the "white lines", correspond to electron transitions from $2p_{3/2}$ and $2p_{1/2}$ levels, respectively, to unoccupied Ti 3*d* states. The deviation from the 2:1 statistical value expected on the basis of j-j coupling depends on the ratio of the singlet-triplet exchange splitting Δ to the spin-orbit splitting λ. As $\Delta/\lambda \rightarrow \infty$, the L_3/L_2 ratio tends to zero [157]. The octahedral crystal field lifts the degeneracy of the 3*d* states into t_{2g} and e_g components. In STO buffer layer, L_3

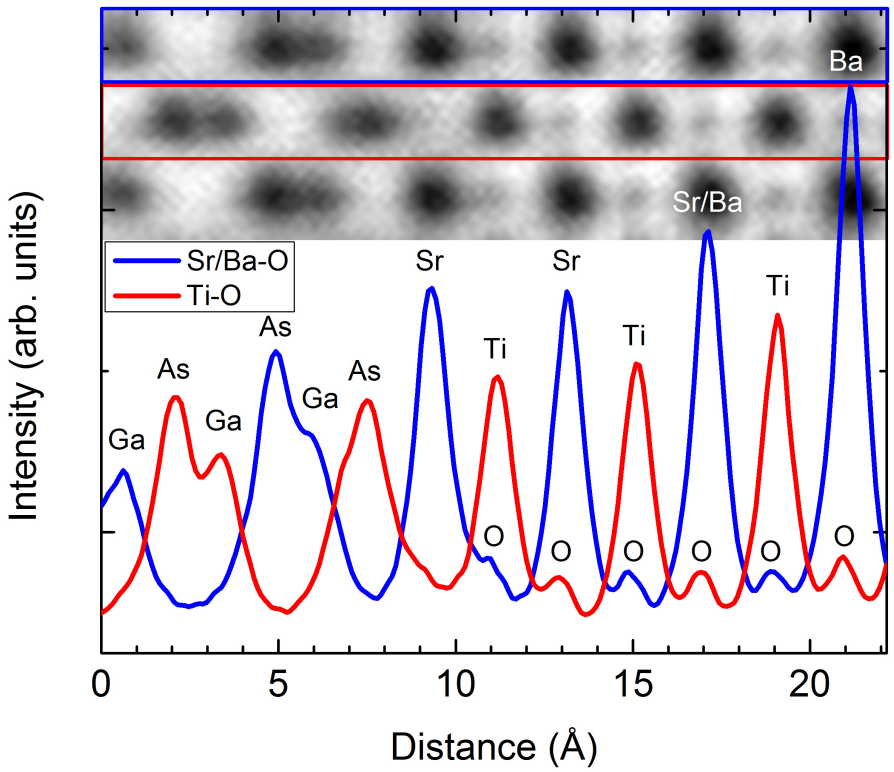

Figure 5.2 Intensity scan of Sr/Ba-O atomic column (blue) and Ti-O column (red). Inserted image is filtered using the radial wanier filter installed within Gatan Digital Micrograph.

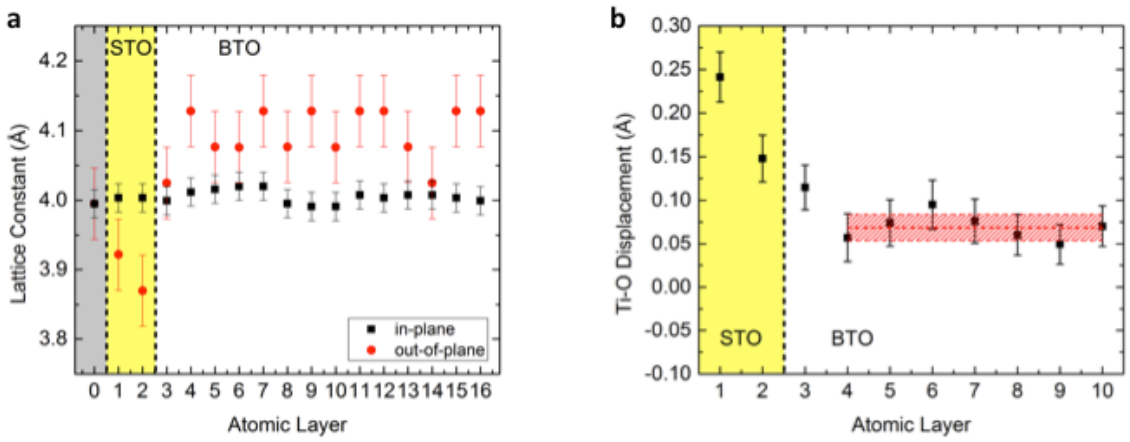

Figure 5.3 (a) in-plane and out-of-plane lattice constant of GaAs, STO, and BTO; (b) Ti-O displacement measured from HAADF image

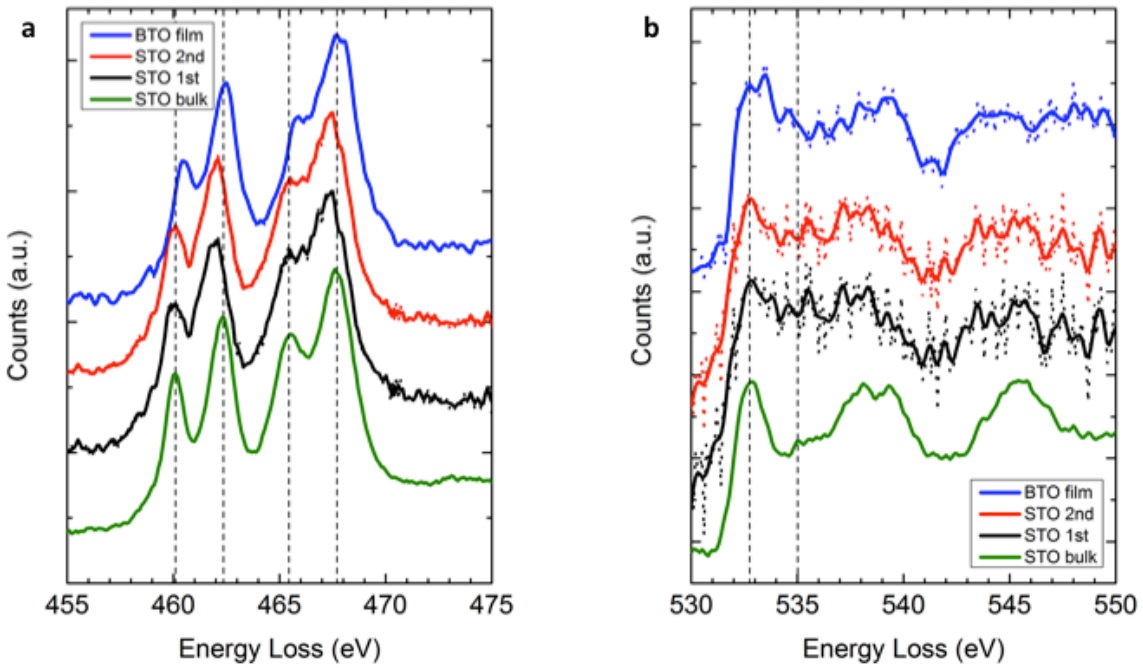

Figure 5.4 EELS spectra of (a) Ti L-edge and (b) O K-edge. Dotted lines are raw data, solid lines are processed after MSA PCA

and L_2 edges both have less crystal field splitting compared to STO bulk, as the gap between t_{2g} and e_g peaks is reduced. This indicates that the TiO_6 octahedra are distorted, along with a further breakdown of t_{2g} and e_g orbital degeneracy. Considering the presence of oxygen vacancies and the shift between positive and negative charge centers, the reduction of crystal field splitting is not unexpected. Similar changes can be found also in BTO film, where ferroelectricity was previously reported by PFM and *c*-oriented lattice constant is measured by XRD [148]. It is worth notice that L_2 e_g peak is broadened in BTO film, which denotes the further splitting of e_g into lower d_{z^2} and higher $d_{x^2-y^2}$ orbitals.

The Ti *L* edge spectra were fitted with Voigt functions (a convolution of Gaussian and Lorentzian function) as shown in Figure 5.5. Each spectrum was fitted with four peaks in the order of Ti L_3 t_{2g}, L_3 e_g, L_2 t_{2g} and L_2 e_g. I took the ratio between integrated intensities of L_3 and integrated intensities of L_2 as shown in Figure 5.6 lower panel. Since higher ratio corresponds to a lower Ti valence [138], I observe a decrease of Ti valence in the STO buffer while Ti remains to be 4+ in BTO film. Crystal field splitting is also used as a means of measuring the TiO_6 octahedra distortion. In the upper panel of Figure 5.6 I measured the L_3 t_{2g} - e_g splitting and found a decrease in both STO buffer and BTO film, comparing to STO bulk. The decrease of crystal field splitting indicates the lowering of e_g orbitals due to the polarization and less orbital overlapping with the ligand orbitals.

The O *K* edge pre-peak stems from O 2*p* - Ti 3*d* hybridization, where the bonding t_{2g}^b and antibonding t_{2g}* are formed by the overlap between O $2p_\pi$ and Ti 3*d* states of t_{2g} symmetry, the overlap between O $2p_\sigma$ and Ti 3*d* states of e_g symmetry leads to the formation of bonding e_g^b and antibonding e_g* molecular orbitals [158]. In Figure 5.4b), I

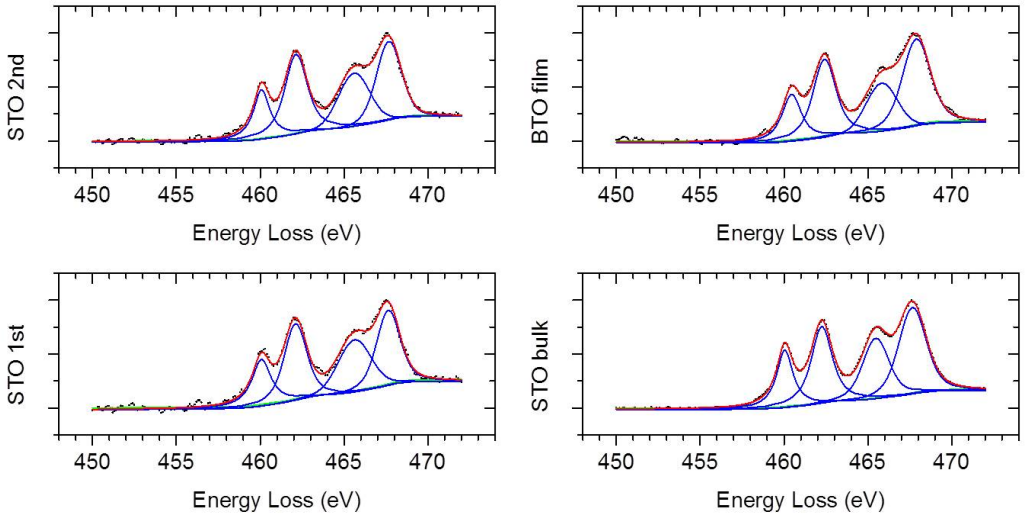

Figure 5.5 Ti *L* edge peak fitting using Voigt function. Dotted line shows original data obtained from EELS, red solid line shows fitted peak using Voigt function, blue line shows each fitted peak, green line (mostly hidden by blue line) shows background fitting.

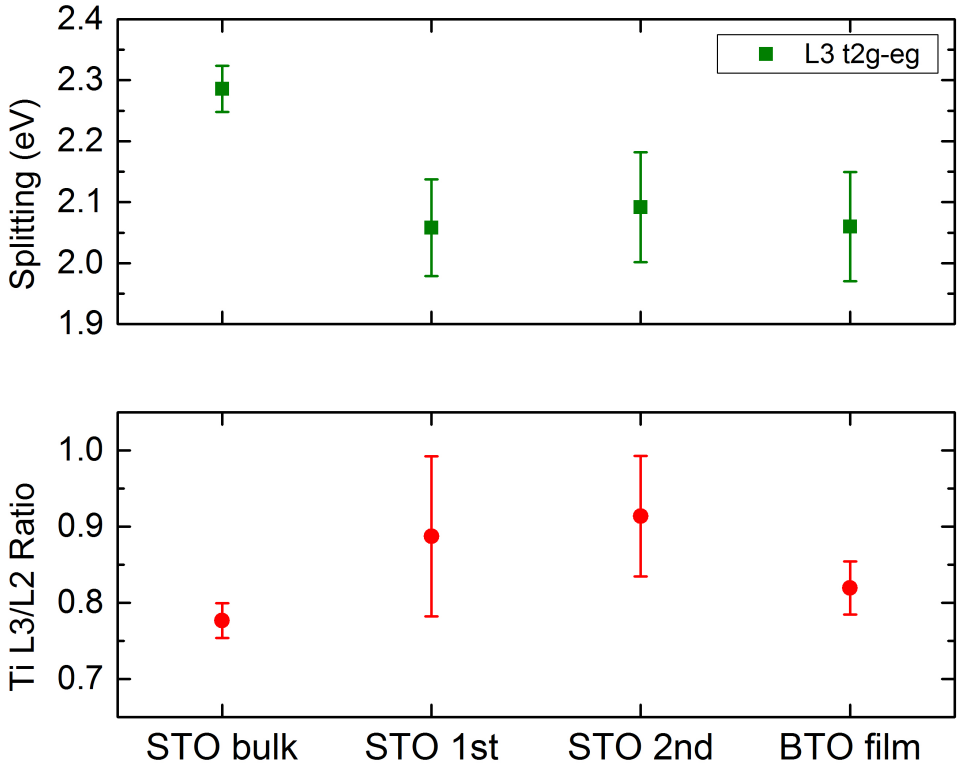

Figure 5.6 Measured Ti L_3 t_{2g} - e_g splitting (upper panel) from EELS data and Ti L_3/L_2 ratio (lower panel) from peak fitting in STO bulk, STO first and second buffer layer, and BTO film, respectively.

see a sharp pre-peak in bulk STO, where electrons transfer to the unoccupied $p_\pi - t_{2g}$* hybrid orbitals. On the TiO_2 columns close to the interface, there is a noticeable shoulder arising before the pre-peak, which denotes the breakdown of the t_{2g} orbital degeneracy. As observed in experiment, the Ti and O columns are displaced in the out-of-plane direction, which reduces the overlapping of in-plane orbitals, thus lowers the d_{xy} and $d_{x^2-y^2}$ orbitals. This brings about another change in the $2p_\sigma - e_g$* hybrid orbitals, but the expected splitting is too small to discern in the "washed out" edges after the pre-peak. In the calculated density of states I show below, the in-plane and out-of-plane orbital splitting is shown in more detail.

5.3.3 Interfacial Energetics

Based on the experimental evidence that the STO buffer layer starts with a highly oxygen deficient SrO layer, I performed first principles DFT calculations to gain a better understanding of the interfacial energetics with respect to the existence of oxygen vacancies. In order to quantitatively address the effect of oxygen vacancies, I considered oxygen vacancy concentration Θ varying from 0 to 1, i.e. from no oxygen vacancy to 4 oxygen vacancies in the first 2x2 SrO layer, as shown in Figure 5.7a). I performed calculation of oxygen chemical potential by assuming the system to be in equilibrium with O_2 in gas phase, with annealing temperature at 1,000 K and O_2 partial pressure at $1x10^{-7}$ mbar [159, 160]. Within a wide range of allowed oxygen chemical potential, higher oxygen vacancy concentrations overwhelmingly decrease the interface energy and are thus more energetically favorable.

5.3.4 Atomic Structure

I studied the polarization observed in STO and BTO film using DFT calculations. In a

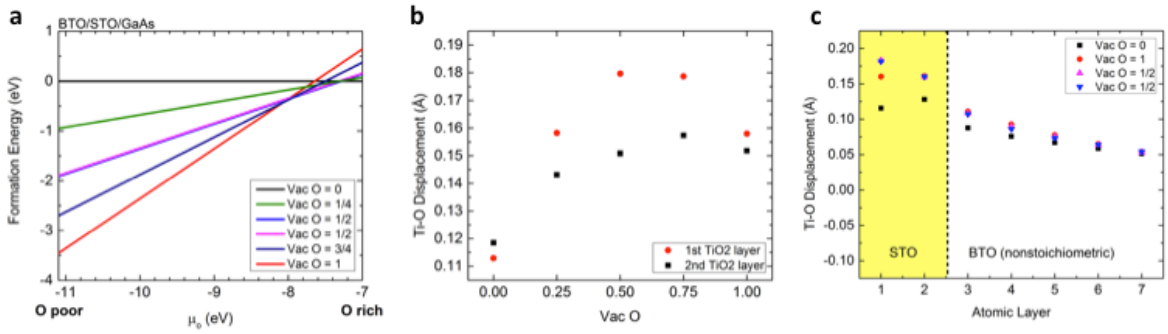

Figure 5.7 (a) DFT interface energy calculation with different oxygen vacancy concentrations. (b) Ti-O displacement in first two TiO_2 columns with different vacancy concentrations. (c) Ti-O displacement in each TiO_2 atomic layer in the calculated supercell

2x2 surface cell BTO/STO/GaAs supercell, I calculated the polarization with various BTO film thickness and oxygen vacancy concentration at STO/GaAs interface. The thickness of STO buffer layer was fixed at 2 unit cells, with BTO varying from 4 to 9 unit cells. Ti-O displacement after structural relaxation was calculated with oxygen vacancy concentration Θ varying from 0 to 1. Figure 5.7b) plots the first two TiO_2 columns in the film, namely the TiO_2 columns in the STO buffer layer. Obviously, the emergence of oxygen vacancy introduces a much larger polarization than in a fully oxygenated buffer layer. Displacement in the other layers are also plotted in Figure 5.7c), and I see a convergence to 0.05 Å regardless of interfacial structure. Comparing the displacement of different BTO thickness, it is noticeable that the Ti-O displacement all converge to a constant positive value at 0.05 Å, and the displacement in the first monolayer does not change with the BTO thickness. To examine the possibility of ferroelectric switching of polarization, I took the nonstoichiometric BTO film and fixed the outmost layer TiO_2 to be poled toward the interface, the film polarization after structural relaxation still behaves to be positive even in the TiO_2 layer next to the fixed negative polarization. I also considered the surface effect, which can alter the top layer polarization in order to provide surface screening charge by including both stoichiometric and nonstoichiometric BTO films. The stoichiometry of the film can induce or cancel surface effects, but will not change the interfacial polarization, and the negative polarization only lasts for one layer at the film/vacuum interface. Detailed results can be found in Figure 5.8. My calculations indicate that the observed polarization in STO and BTO film remains positive and converge to a constant number within a wide range of the film thickness, and can be significantly affected by the interfacial geometry.

5.3.5 Electronic Structure

The electronic structure was also studied using orbital projected density of states (DOS). Figure 5.9 shows the calculated O *p*-orbital DOS from first TiO_2 layer next to the interface and bulk STO, along with the corresponding EELS spectra. In the interfacial TiO_2 layer, the shoulder at 0.8 eV before the O *K* edge pre-peak is found in the DOS with oxygen vacancy concentration $\Theta = 1$ but not so evident in the DOS with $\Theta = 0$. In STO bulk, neither EELS nor DOS has a shoulder before the pre-peak. Another characteristic change is the enhancement at 533.8 and 534.5 eV, as one could also note in the DOS with $\Theta = 1$ but smears out from 534 to 536 eV with $\Theta = 0$. The O *K* edge pre-peak at 532.8 eV is formed by electron transfer to the unoccupied O $2p$ – Ti $3d$ t_{2g} hybrid orbitals, whereas the O $2p$ – Ti $3d$ e_g hybrid orbitals are located at higher energies, around 535 eV as observed in the STO bulk EELS. The shoulder before pre-peak indicates further splitting of Ti $3d$ t_{2g} as a result of the polarization in STO. Oxygen vacancies would reinforce this effect, by generating larger Ti-O displacement as shown in Figure 5.7b). The enhancement of O $2p$ – Ti $3d$ e_g hybrid orbitals serves as another evidence of oxygen vacancies. I studied the orbital projected DOS and found a shoulder around 1 eV after the pre-peak contributed by the oxygen p_z orbital, and an increase at 1.7 eV after the pre-peak in the oxygen p_x and p_y orbitals. According to ligand field theory, introducing oxygen vacancy at interface significantly reduces the $p_z - d_{z^2}$ orbital overlapping, giving rise to a larger electron transfer and a shift to lower energy at 1eV after the pre-peak; the large out-of-plane polarization also reduces the overlapping of p_x p_y – $d_{x^2-y^2}$ orbitals, as one could observe the enhancement at 1.7 eV after the pre-peak.

With oxygen vacancy concentration $\Theta = 0$ and $\Theta = 1$, orbital projected DOS

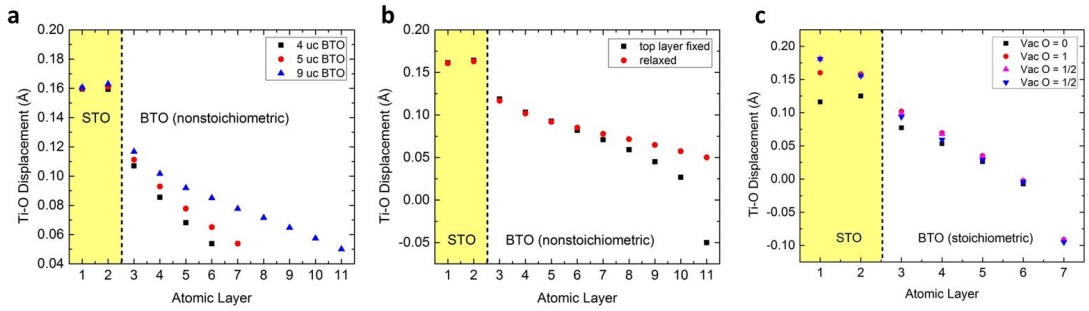

Figure 5.8 Ti-O displacement in each TiO_2 layer (a) with 4, 5, and 9 unit cells of nonstoichiometric BTO film while Θ = 1; (b) with 9 unit cells of nonstoichiometric BTO film by fixing (black) last layer displacement or relaxing all atoms in the film (red) while Θ = 1; (c) with 5 unit cells of stoichiometric BTO film while varying Θ from 0 to 1.

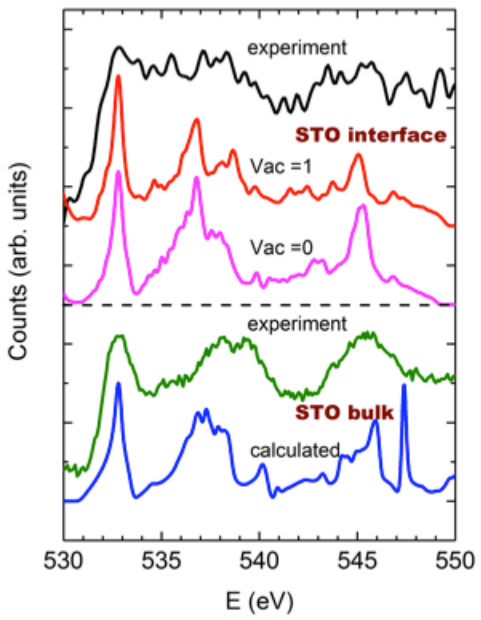

Figure 5.9 experimental O K-edge spectra in comparison with calculated O 2p-orbital projected DOS in STO bulk (lower) and first TiO_2 layer (upper). Calculation is performed on both oxygen sufficient and deficient interfaces

calculations were performed using VASP. Figure 5.10 shows the summed up DOS of O and Ti atoms in the first TiO_2 layer with $\Theta = 0$. The first peak at 1.5 eV is formed by the empty O $2p$ – Ti $3d$ t_{2g} hybrid orbitals, and O atoms exhibit degeneracy in the in-plane p_x p_y orbitals. For the O $2p$ – Ti $3d$ e_g hybrid orbitals, the p_x p_y – $d_{x^2-y^2}$ hybridization smears out from 2.7 eV to 5 eV, p_z – d_{z^2} hybrid orbital shows no enhancement due to little distortion of the TiO_6 octahedra without the presence of oxygen vacancies. In Figure 5.11, corresponding O and Ti orbital projected DOS are shown with $\Theta = 1$, one sees a significant enhancement at 3.2 eV indicating p_x p_y – $d_{x^2-y^2}$ hybridization and at 2.2 eV an increase of p_z – d_{z^2} hybrid orbital can be noticed. As observed from the relaxed structure, oxygen vacancies render larger Ti-O displacement and less overlapping of p_x p_y – $d_{x^2-y^2}$ hybrid orbitals. By missing the interfacial O atoms, energy of the p_z – d_{z^2} hybrid orbital decreases significantly and shows a peak at lower energy compared to the in-plane orbitals. The effect of oxygen vacancies is also noticeable in the O $2p$ – Ti $3d$ t_{2g} hybrid orbitals, as one can see a splitting of Ti d_{yz} and d_{yz} orbitals and their hybridization with O p_x and p_y orbitals causes a shoulder before the first peak at 1.3 eV.

The study of interfacial conductivity indicates a conducting interface in both systems with and without oxygen vacancies. However, the interface states at Fermi level are attributed to the As p_x orbital only with $\Theta = 1$, but a fully oxygenated interface would have As p_x, s, p_z and d_{z^2} orbitals contributing at the Fermi level. The extra orbital contributions are due to the As – O covalence bond and can be found also in the oxygen orbital projected DOS. XPS measurement during the growth procedure shows no evidence of As – O bond, which confirms the existence of oxygen vacancies. In Figure 5.12, the orbital projected DOS of surface As, first layer O and Sr atoms are shown, since

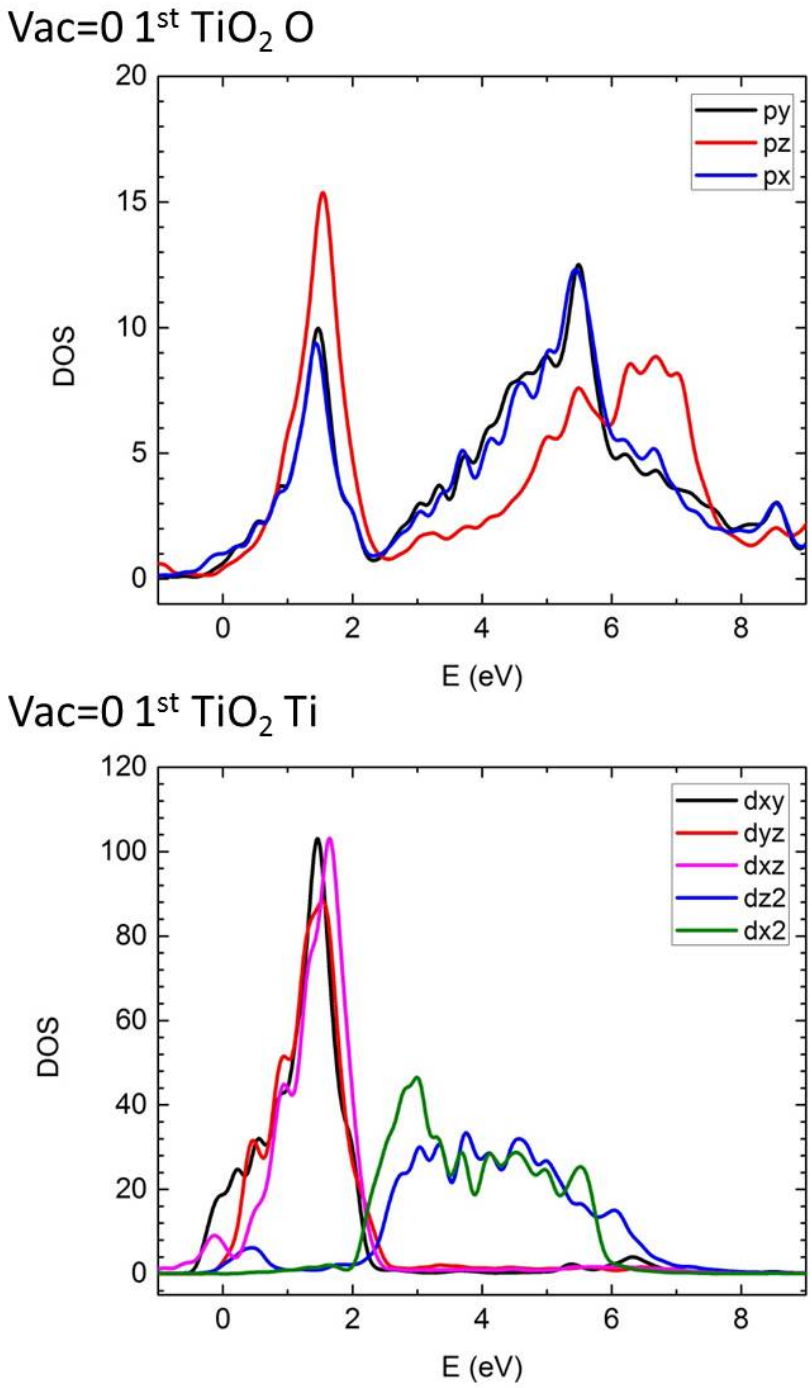

Figure 5.10 Orbital projected O (upper panel) and Ti (lower panel) density of states in first TiO_2 layer with $\Theta = 0$.

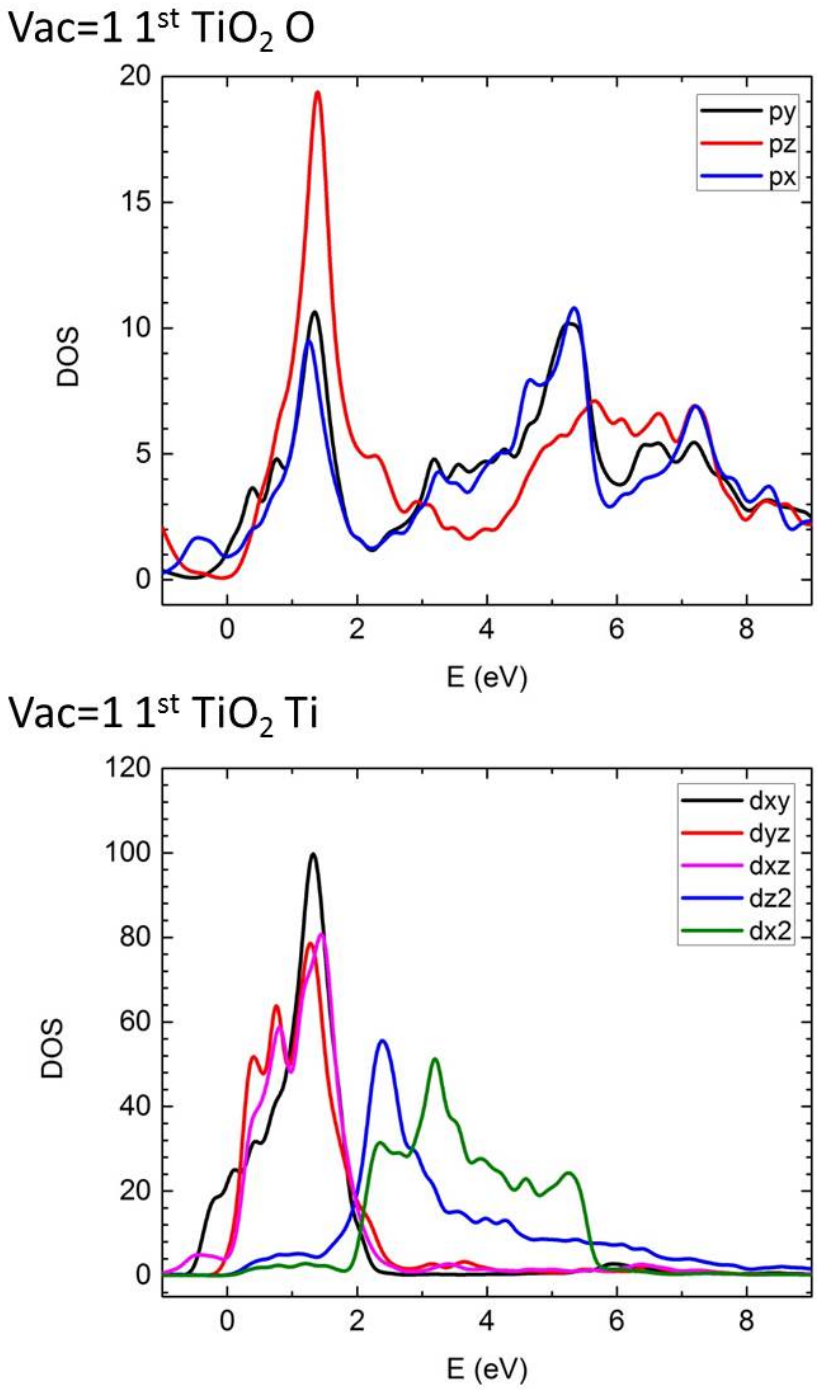

Figure 5.11 Orbital projected O (upper panel) and Ti (lower panel) density of states in first TiO_2 layer with $\Theta = 1$.

these atomic orbitals contribute to the STO/GaAs interfacial states with $\Theta = 0$. At Fermi level (0 eV), both As and O have electron distributions due to the formation of As – O bonds, while Sr atoms do not contribute to the interfacial conductivity. In Figure 5.13 where $\Theta = 1$, only As p_x orbital is contributing to the Fermi level states, thus a much lower conductivity would be expected.

5.4 Discussion

The electron transfer at interface between polar and non-polar oxide has been attributed to the emergence of oxygen vacancy, in order to compensate the excess charge at the interface [31, 137]. In the case of LAO/STO interface, which exhibits a two dimensional electron gas, the $(AlO_2)^{1-}$/(SrO) interface is a hole doped *p*-type interface, which can be compensated by introducing oxygen vacancies in order to avoid polar catastrophe [21]. Similar cases have been reported in the system consisting of polar and non-polar semiconductors [40]. Whereas in our case, each surface As has two dangling bonds, according to the electron counting rule and auto-compensation model [39, 44], each dangling bond has 1.25 electrons, thus requiring 1.5 electrons to compensate two anion-derived dangling bonds. Hence, the As-terminated surface is analogous to the *p*-type $(AlO_2)^{1-}$ surface, and an adjacent SrO layer with oxygen vacancies is expected regardless of the growth condition, since oxygen vacancies are electron donors. However, the *p*-type LAO/STO interface was found to be insulating, and oxygen vacancies play an important role by donating electrons to compensate the surface holes. One could consequently speculate that the As/SrO interface is also insulating, by compensating the dangling bonds with oxygen vacancies. Nevertheless, our results suggest a conducting interface regardless of the oxygen vacancy concentration. In other DFT studies carried on

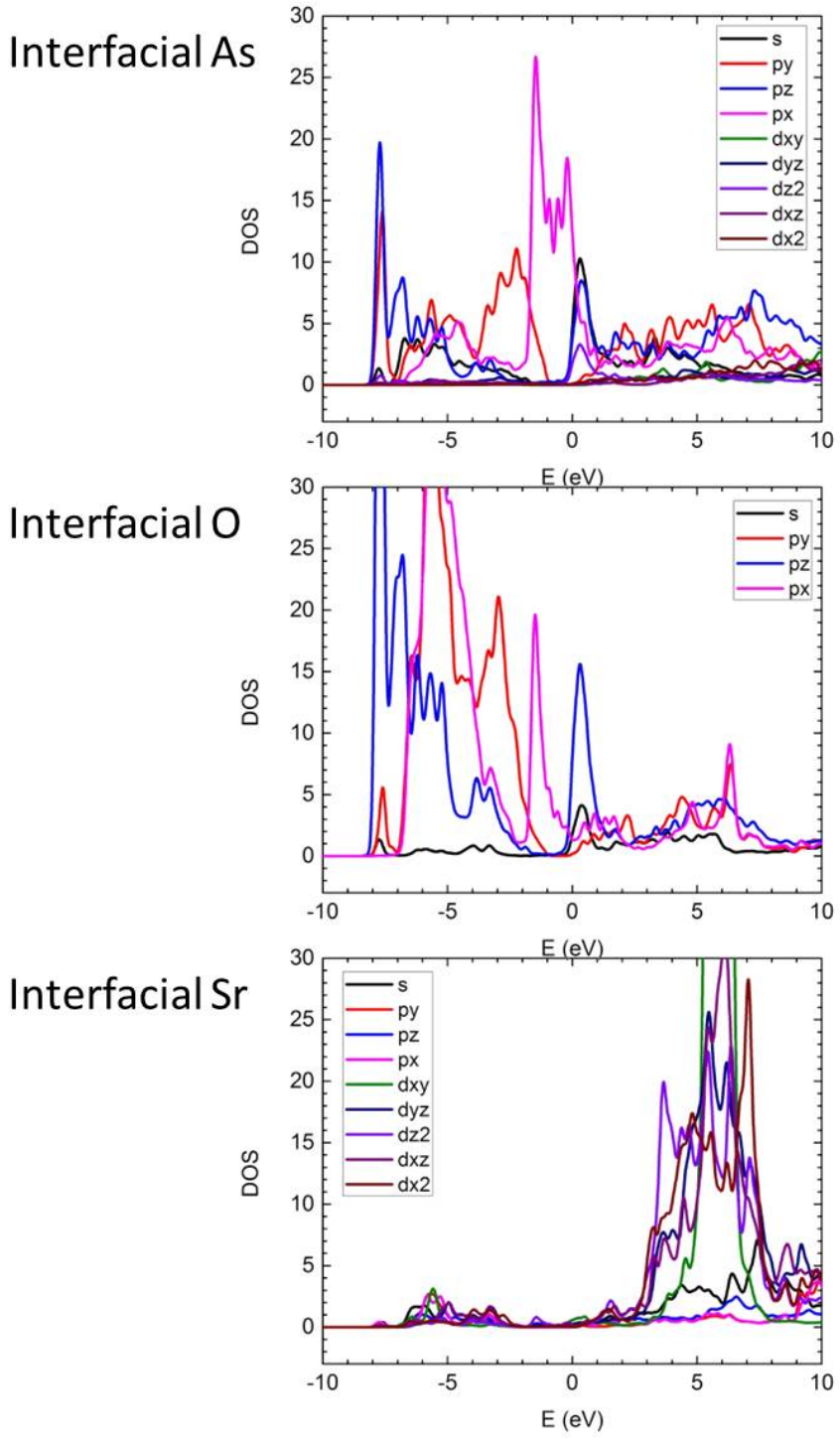

Figure 5.12 Orbital projected As (upper panel), O (middle panel) and Sr (lower panel) density of states at the STO/GaAs interface with Θ = 0.

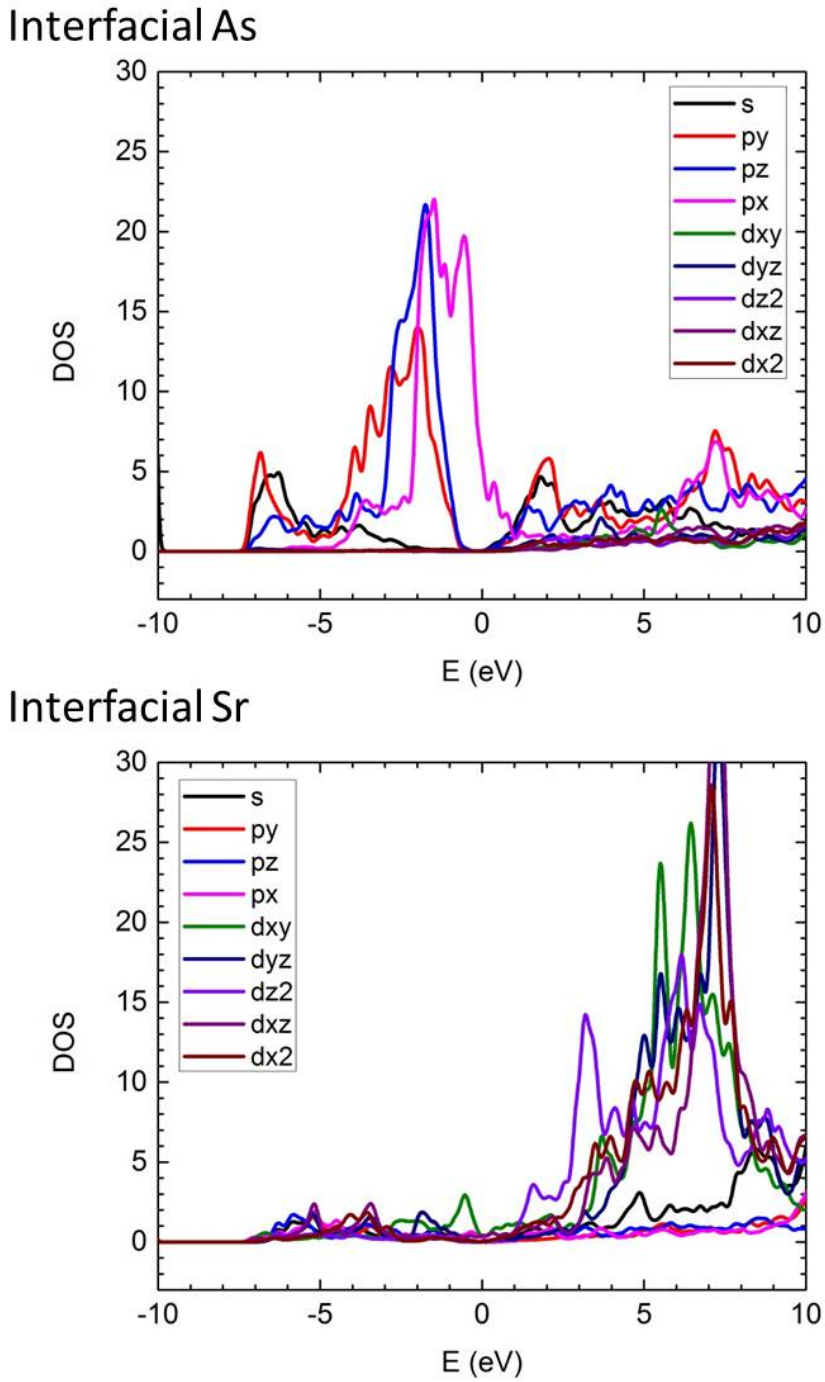

Figure 5.13 Orbital projected As (upper panel) and Sr (lower panel) density of states at the STO/GaAs interface with Θ = 1.

STO/Si interface, it was also reported that a metallic interface is present regardless of oxygen vacancies [61]. It has been pointed out by Noguera that the electron counting rule and auto-compensation model cannot be applied to ternary systems, since such model takes the averaged electrons per bond over Sr-O and Ti-O bonds, instead of considering the electron distribution on each individual bond [17]. According to Kolpak *et al*, the interface Sr always generates an electrical dipole and induces irreversible polarization in the STO film [161]. In our case, the presence of oxygen vacancy compensates the As dangling bonds, leaving the Sr cations forming ionic bonds with the O anions in the first TiO_2 layer, and producing large electrical dipole. When the first SrO layer is fully oxygenated, the dipole between interfacial O anions and first layer Ti cations would offset the dipole between interfacial Sr cations and first layer O anions, but interfacial O also forms covalence bond with surface As, which weakens the O-Ti dipole, as one could see a much lower but still positive polarization in the STO buffer. The ferroelectricity measured by PFM is not reproduced by our calculation, which can be attributed by a reversible generating or annihilation of oxygen vacancies during PFM measurement.

5.5 Summary

In summary, I have performed Z-contrast and ABF imaging to show direct evidence of interfacial oxygen vacancies, as well as a monodomain polarization in the STO buffer layer and BTO film. With the polar axis normal to the interface, I observed out-of-plane tetragonality and polarization in BTO film. A significantly higher polarization was found in the STO buffer, and was attributed to the interfacial dipole reinforced by oxygen vacancies. EELS study suggests distortion of TiO_6 octahedra as a result of polarization and oxygen vacancy. Further, DFT calculations confirm that the energetically preferred

interface is highly oxygen deficient, and the emergence of oxygen vacancy significantly increases interfacial dipole and generating large polarization in the STO layers. The strong interfacial dipole is found to be prohibiting ferroelectric switching. DOS calculations shed light on the cause of changes observed by EELS, and provide supportive information on the existence of oxygen vacancy and film polarization.

CHAPTER 6
CONCLUSIONS AND REMARKS

In this thesis, I have used a combination of STEM and DFT to investigate a number of $SrTiO_3$/GaAs interfaces. Aberration-corrected STEM imaging and EELS were used to provide information on the structure, composition, and bonding characteristics at the interface with a sub-angstrom resolution. The theoretical DFT calculations, on the other hand, served to model the interfacial atomic and electronic structures, focusing on issues including the terminating oxide layer as a function of growing conditions, surface reconstructions evolving during film deposition, and finding most stable configuration of defects at or near the support/oxide interface.

By examining two types of STO/GaAs interfaces with and without half monolayer of Ti pre-deposition with STEM, I have found no evidence of surface reconstructions or any difference in interfacial registry. By lowering the primary electron energy to 80 keV, I was able to perform EELS study on the STO/GaAs interface without introducing noticeable beam damage. The recorded EELS signal indicates diffusion of Ti from the film into subsurface GaAs regardless of growth condition, which turned out to be crucial in understanding the interfacial bonding states that strongly depend on the different pre-layer growth conditions. I performed DFT calculations to unveil different interfacial bonding between the SrO and GaAs layers, and suggested a possible scenario of the

initial stages of the STO film deposition. The Ti pre-layer, although it did not result in any noticeable changes in interfacial atomic structure, indeed prevented the substrate from getting oxidized, hence alleviated the Fermi level pinning.

DFT calculations on STO/GaAs interfaces were performed to help understand interfacial energetics and electronic structures. It was found that, by considering non-stoichiometric STO films starting and ending with the same type of cation-oxygen layer, one could find a lowest energy configuration that stabilizes the relative interface energy, which does not change within the allowed range of chemical potentials. The absence of GaAs surface reconstruction was studied by calculating the formation energy profile of Ti adatoms onto the GaAs(001) β2-(2x4) surface reconstructions. I noticed that Ti adatoms, when taking its lowest formation energy configuration, always break the surface As dimer and sink into subsurface GaAs. These findings were in good agreement with experimental observations, in which the surface reconstructions disappeared after film deposition, and Ti signal penetrated into GaAs substrate for a few angstroms. Guided by these computations, I then performed calculations on Ti impurities in bulk GaAs in order to predict a possible configuration of Ti impurities. Antisites and interstitial sites were considered in the calculations, which indicated that Ti replacing Ga could lead to a lower defect formation energy. The Ti defect penetration depth was also studied, and it clearly showed that deeper penetration would not be energetically favorable.

Using STO/GaAs as a platform for functional oxide growth, I then proceeded to examine the $BaTiO_3/SrTiO_3$/GaAs heterointerfaces. The 20 unit cell BTO film was deposited onto GaAs by inserting 2 unit cells of STO buffer. Z-contrast and ABF imaging showed abrupt STO/GaAs and BTO/STO interfaces without reconstruction or defects. It

was interesting to note that a highly oxygen deficient SrO layer at STO/GaAs was found, followed by a STO buffer undergoing tensile strain and BTO film seeing compressive strain. Using ABF imaging, I measured the in-plane and out-of-plane lattice parameters of STO and BTO, as well as the displacement between Ti and O columns. Surprisingly, STO buffer layer exhibited larger out-of-plane Ti-O displacement than BTO film did, even under an in-plane tensile strain. To address the importance of interfacial dipole that could play a major role in generating out-of-plane polarization, I performed DFT calculations on the BTO/STO/GaAs 2x2 surface cell. Limited by the computation time, I considered supercells with up to 9 unit cells of BTO. I calculated the oxygen vacancy formation energy of STO/GaAs interfaces with various oxygen vacancy concentrations and found that, within the allowed range of O_2 partial pressure and chemical potential, higher oxygen vacancy concentration would lead to lower relative interface energy, hence stabilizing the STO/GaAs interface. I plotted Ti-O polarization in each TiO_2 layer after structural relaxation, and found a significantly larger displacement in STO buffer layer, decreasing gradually into the BTO film and converging to a constant. I did a series of calculations to validate my finding, and it turned out that both STO and BTO films had a non-switchable polarization away from the oxide/semiconductor interface, which could be the consequence of an out-of-plane interfacial dipole. In order to explore the electronic structure at the interface, I performed STEM EELS across the interface along with DFT density of states (DOS) calculations. The experiments and calculations agreed very well, indicating further splitting of the Ti 3*d* t_{2g} and e_g orbitals, which is the result of the presence of interfacial oxygen vacancies and the observed Ti-O displacement. Both are considered to contribute to the distortion of TiO_6 octahedra. The lack of symmetry would

then give rise to further ligand field splitting and therefore extra shoulders or peaks in the DOS, which was measured experimentally using EELS.

In summary, my studies showed that the BTO film polarization is nonswitchable, although previous piezo-force microscopy (PFM) measurements conducted on the same films appear to exhibit ferroelectricity in the BTO film. Guided by the calculations, and considering the PFM mechanism, I speculate that the PFM measurements observe a physical expansion or contraction of BTO film resulting from the introduction or removal of oxygen vacancies during the application of an electric field. In other words, without confirming that the mass of the film (i.e. the stoichiometry) was conserved, it is not proper to conclude that BTO films on GaAs substrates have a switchable polarization. Fortunately, we now have the ability to perform aberration-corrected STEM imaging and EELS, in conjunction with applying an electric bias to the sample *in-situ* to directly test polarization of the BTO and STO films as a function of applied bias. It would also be helpful to examine such interfaces with other exchange correlation functionals such as GGA PBE and GGA PW91 in order to verify the calculations done with LDA, so that a complete and fundamental understanding of the perovskite oxide – compound semiconductor interface can be achieved.

REFERENCES

[1] R. J. W. Hill *et al.*, Ieee Electron Device Letters **28**, 1080 (2007).
[2] R. J. W. Hill *et al.*, Electronics Letters **43**, 543 (2007).
[3] S. Salahuddin, and S. Datta, IEEE International Electron Devices Meeting 2008, 693 (2008).
[4] E. Bousquet *et al.*, Nature **452**, 732 (2008).
[5] C. H. Ahn, K. M. Rabe, and J. M. Triscone, Science **303**, 488 (2004).
[6] A. Ohtomo, and H. Y. Hwang, Nature **427**, 423 (2004).
[7] E. J. Tarsa *et al.*, Journal of Applied Physics **73**, 3276 (1993).
[8] R. A. McKee, F. J. Walker, and M. F. Chisholm, Physical Review Letters **81**, 3014 (1998).
[9] K. Eisenbeiser *et al.*, Applied Physics Letters **76**, 1324 (2000).
[10] X. Liu *et al.*, Journal of Vacuum Science & Technology A: Vacuum, Surfaces, and Films **19**, 391 (2001).
[11] H. Li *et al.*, Journal of Applied Physics **93**, 4521 (2003).
[12] M. Hong *et al.*, Applied Physics Letters **76**, 312 (2000).
[13] G. D. Wilk, R. M. Wallace, and J. M. Anthony, Journal of Applied Physics **89**, 5243 (2001).
[14] J. Lettieri, J. H. Haeni, and D. G. Schlom, Journal of Vacuum Science & Technology A: Vacuum, Surfaces, and Films **20**, 1332 (2002).
[15] J. W. Reiner *et al.*, Advanced Materials **22**, 2919 (2010).
[16] M. Passlack *et al.*, Applied Physics Letters **82**, 1691 (2003).
[17] C. Noguera, J Phys-Condens Mat **12**, R367 (2000).
[18] J. H. Haeni *et al.*, Nature **430**, 758 (2004).
[19] D. Kim *et al.*, Physical Review Letters **95** (2005).
[20] D. G. Schlom *et al.*, Annual Review of Materials Research **37**, 589 (2007).
[21] S. A. Pauli, and P. R. Willmott, Journal of Physics: Condensed Matter **20**, 264012 (2008).
[22] M. F. Chisholm *et al.*, Physical Review Letters **105** (2010).
[23] H. W. Jang *et al.*, Science **331**, 886 (2011).
[24] Z. Yu *et al.*, Journal of Vacuum Science & Technology B **18**, 1653 (2000).
[25] K. Eisenbeiser *et al.*, Applied Physics Letters **76**, 1324 (2000).
[26] J. Wang *et al.*, Applied Physics Letters **85**, 2574 (2004).
[27] Y. Wang *et al.*, Applied Physics Letters **80**, 97 (2002).
[28] Y. Liang *et al.*, Applied Physics Letters **85**, 1217 (2004).
[29] R. F. Klie *et al.*, Applied Physics Letters **87**, 143106 (2005).
[30] Y. Liang, J. Curless, and D. McCready, Applied Physics Letters **86**, 082905 (2005).
[31] A. Ohtomo *et al.*, Nature **419**, 378 (2002).
[32] K. S. Takahashi, M. Kawasaki, and Y. Tokura, Applied Physics Letters **79**, 1324 (2001).
[33] H. Ohta *et al.*, Nature Materials **6**, 129 (2007).
[34] K. Szot *et al.*, Nature Materials **5**, 312 (2006).

[35] J. Mannhart *et al.*, Mrs Bull **33**, 1027 (2008).
[36] W. A. Harrison, J Vac Sci Technol **16**, 1492 (1979).
[37] G. X. Qian, R. M. Martin, and D. J. Chadi, Physical Review Letters **60**, 1962 (1988).
[38] G. X. Qian, R. M. Martin, and D. J. Chadi, Physical Review B **38**, 7649 (1988).
[39] H. H. Farrell, J. P. Harbison, and L. D. Peterson, J Vac Sci Technol B **5**, 1482 (1987).
[40] W. A. Harrison *et al.*, Physical Review B **18**, 4402 (1978).
[41] V. P. LaBella *et al.*, Physical Review Letters **83**, 2989 (1999).
[42] V. P. LaBella *et al.*, Surface Science Reports **60**, 1 (2005).
[43] D. J. Chadi, J Vac Sci Technol A **5**, 834 (1987).
[44] M. D. Pashley, Physical Review B **40**, 10481 (1989).
[45] H. H. Farrell, and C. J. Palmstrom, J Vac Sci Technol B **8**, 903 (1990).
[46] G. R. Bell *et al.*, Physical Review B **59**, 2947 (1999).
[47] V. P. LaBella *et al.*, Int J Mod Phys B **15**, 2301 (2001).
[48] Q. K. Xue, T. Hashizume, and T. Sakurai, Prog Surf Sci **56**, 1 (1997).
[49] A. Ohtake, and N. Koguchi, Applied Physics Letters **83**, 5193 (2003).
[50] A. Ohtake *et al.*, Physical Review Letters **89** (2002).
[51] A. Ohtake *et al.*, Physical Review Letters **92** (2004).
[52] E. Penev, P. Kratzer, and M. Scheffler, Physical Review Letters **93** (2004).
[53] W. G. Schmidt, and F. Bechstedt, Physical Review B **54**, 16742 (1996).
[54] J. G. LePage *et al.*, Physical Review B **58**, 1499 (1998).
[55] T. Ohno, Physical Review Letters **70**, 631 (1993).
[56] C. G. Van de Walle, Journal of Applied Physics **95**, 3851 (2004).
[57] S. B. Zhang, and A. Zunger, Physical Review B **53**, 1343 (1996).
[58] W. G. Schmidt, S. Mirbt, and F. Bechstedt, Physical Review B **62**, 8087 (2000).
[59] S. H. Lee, W. Moritz, and M. Scheffler, Physical Review Letters **85**, 3890 (2000).
[60] F. Bastiman, A. G. Cullis, and M. Hopkinson, Surface Science **603**, 2398 (2009).
[61] I. Yakovkin, and M. Gutowski, Physical Review B **70** (2004).
[62] M. Kniffin, and C. R. Helms, Journal of Vacuum Science & Technology a-Vacuum Surfaces and Films **5**, 1511 (1987).
[63] K. B. Kim *et al.*, J Vac Sci Technol A **6**, 1473 (1988).
[64] C. E. Mccants *et al.*, J Vac Sci Technol A **6**, 1466 (1988).
[65] X. Zhang *et al.*, Physical Review B **68** (2003).
[66] C. J. Forst *et al.*, Nature **427**, 53 (2004).
[67] A. A. Demkov, and X. Zhang, Journal of Applied Physics **103**, 103710 (2008).
[68] A. M. Kolpak, and S. Ismail-Beigi, Physical Review B **83** (2011).
[69] R. Contreras-Guerrero *et al.*, J Cryst Growth **378**, 238 (2013).
[70] R. Erni *et al.*, Physical Review Letters **102** (2009).
[71] O. L. Krivanek *et al.*, Ultramicroscopy **108**, 179 (2008).
[72] O. L. Krivanek *et al.*, Nature **464**, 571 (2010).
[73] O. L. Krivanek *et al.*, Ultramicroscopy **110**, 935 (2010).
[74] N. Browning *et al.*, Reviews on Advanced Materials Science(Russia) **1**, 1 (2000).

[75] R. Klie, Physics **2** (2009).
[76] M. Haider *et al.*, Ultramicroscopy **75**, 53 (1998).
[77] M. Lentzen *et al.*, Ultramicroscopy **92**, 233 (2002).
[78] H. Sawada *et al.*, Journal of Electron Microscopy **54**, 119 (2005).
[79] M. Haider, H. Müller, and S. Uhlemann, **153**, 43 (2008).
[80] M. Haider *et al.*, Philos Trans A Math Phys Eng Sci **367**, 3665 (2009).
[81] H. Muller *et al.*, Microscopy and Microanalysis **12**, 442 (2006).
[82] O. L. Krivanek, N. Dellby, and A. R. Lupini, Ultramicroscopy **78**, 1 (1999).
[83] P. E. Batson, N. Dellby, and O. L. Krivanek, Nature **418**, 617 (2002).
[84] N. Dellby *et al.*, Journal of Electron Microscopy **50**, 177 (2001).
[85] O. L. Krivanek *et al.*, Ultramicroscopy **96**, 229 (2003).
[86] P. D. Nellist, 91 (2011).
[87] O. Scherzer, Journal of Applied Physics **20**, 20 (1949).
[88] D. E. Jesson, and S. J. Pennycook, P R Soc-Math Phys Sc **449**, 273 (1995).
[89] P. D. Nellist, and S. J. Pennycook, Ultramicroscopy **78**, 111 (1999).
[90] R. F. Klie, and N. D. Browning, Journal of Electron Microscopy **51**, S59 (2002).
[91] R. F. Klie *et al.*, Applied Physics Letters **96**, 082510 (2010).
[92] R. F. Klie *et al.*, Journal of Electron Microscopy **58**, 185 (2008).
[93] E. Okunishi *et al.*, Microscopy and Microanalysis **15**, 164 (2009).
[94] P. E. Batson, Nature Materials **10**, 270 (2011).
[95] S. D. Findlay *et al.*, Applied Physics Letters **95**, 191913 (2009).
[96] S. D. Findlay *et al.*, Ultramicroscopy **110**, 903 (2010).
[97] R. Ishikawa *et al.*, Nature Materials **10**, 278 (2011).
[98] E. Okunishi, H. Sawada, and Y. Kondo, Micron **43**, 538 (2012).
[99] R. F. Egerton, 1 (2011).
[100] W. Van den Broek *et al.*, Ultramicroscopy **106**, 269 (2006).
[101] W. Van den Broek *et al.*, Ultramicroscopy **109**, 296 (2009).
[102] M. Watanabe, E. Okunishi, and K. Ishizuka, Microscopy and Analysis-UK, 5 (2009).
[103] E. M. James *et al.*, Journal of Electron Microscopy **47**, 561 (1998).
[104] R. F. Klie, and N. D. Browning, Applied Physics Letters **77**, 3737 (2000).
[105] http://www.rrc.uic.edu/ems.
[106] P. Hohenberg, Physical Review **136**, B864 (1964).
[107] W. Kohn, and L. J. Sham, Physical Review **140**, A1133 (1965).
[108] E. Wigner, Physical Review **46**, 1002 (1934).
[109] W. Kohn, and L. J. Sham, Physical Review **140**, A1133 (1965).
[110] D. M. Ceperley, and B. J. Alder, Physical Review Letters **45**, 566 (1980).
[111] S. H. Vosko, L. Wilk, and M. Nusair, Canadian Journal of Physics **58**, 1200 (1980).
[112] J. P. Perdew, and A. Zunger, Physical Review B **23**, 5048 (1981).
[113] J. Harris, and R. Jones, Journal of Physics F: Metal Physics **4**, 1170 (1974).
[114] O. Gunnarsson, and B. Lundqvist, Physical Review B **13**, 4274 (1976).
[115] D. C. Langreth, and J. P. Perdew, Physical Review B **15**, 2884 (1977).
[116] J. P. Perdew, and Y. Wang, Physical Review B **45**, 13244 (1992).
[117] J. P. Perdew, K. Burke, and M. Ernzerhof, Physical Review Letters **77**, 3865 (1996).

[118] H. J. Monkhorst, and J. D. Pack, Physical Review B **13**, 5188 (1976).
[119] J. Phillips, Physical Review **112**, 685 (1958).
[120] M. C. Payne, T. A. Arias, and J. D. Joannopoulos, Reviews of Modern Physics **64**, 1045 (1992).
[121] M. T. Yin, and M. L. Cohen, Physical Review B **25**, 7403 (1982).
[122] P. E. Blöchl, Physical Review B **50**, 17953 (1994).
[123] M. Hong *et al.*, Science **283**, 1897 (1999).
[124] N. A. Pertsev, A. K. Tagantsev, and N. Setter, Physical Review B **61**, R825 (2000).
[125] J. C. Woicik *et al.*, Physical Review B **73** (2006).
[126] M. P. Warusawithana *et al.*, Science **324**, 367 (2009).
[127] M. G. Blamire *et al.*, Advanced Materials **21**, 3827 (2009).
[128] R. F. Klie *et al.*, in 2006 APS March MeetingBaltimore, MD, 2006).
[129] J. Wang, X. S. Wu, and D. Bai, EPL (Europhysics Letters) **86**, 46008 (2009).
[130] Q. Qiao *et al.*, in APS March Meeting 2010Portland, Oregon, 2010).
[131] O. L. Krivanek *et al.*, Nature **464**, 571 (2010).
[132] O. L. Krivanek *et al.*, Ultramicroscopy **110**, 935 (2010).
[133] T. Isabell *et al.*, Microscopy Today, 8 (2009).
[134] G. Kresse, and J. Furthmuller, Physical Review B **54**, 11169 (1996).
[135] J. E. Northrup, and S. Froyen, Mat Sci Eng B-Solid **30**, 81 (1995).
[136] A. Ohtake *et al.*, Physical Review B **65** (2002).
[137] D. A. Muller *et al.*, Nature **430**, 657 (2004).
[138] M. Sankararaman, and D. Perry, J Mater Sci **27**, 2731 (1992).
[139] R. Klie *et al.*, Physical Review B **68** (2003).
[140] M. M. Frank *et al.*, Applied Physics Letters **86** (2005).
[141] M. L. Huang *et al.*, Applied Physics Letters **87**, 252104 (2005).
[142] D. I. Garcia-Gutierrez *et al.*, Journal of Vacuum Science & Technology B: Microelectronics and Nanometer Structures **27**, 2390 (2009).
[143] O. Wada, S. Yanagisawa, and H. Takanashi, Applied Physics Letters **29**, 263 (1976).
[144] R. Ludeke, and G. Landgren, Physical Review B **33**, 5526 (1986).
[145] Q. Qiao, R. F. Klie, and S. Ogut, (unpublished).
[146] X. Zhang, and A. A. Demkov, Journal of Vacuum Science & Technology B: Microelectronics and Nanometer Structures **20**, 1664 (2002).
[147] P. W. Peacock, and J. Robertson, Applied Physics Letters **83**, 5497 (2003).
[148] R. Contreras-Guerrero *et al.*, Applied Physics Letters **102**, 012907 (2013).
[149] G. Kresse, and J. Hafner, Physical Review B **47**, 558 (1993).
[150] Q. Qiao *et al.*, Physical Review B **85** (2012).
[151] R. A. McKee, F. J. Walker, and M. F. Chisholm, Science **293**, 468 (2001).
[152] V. Vaithyanathan *et al.*, Journal of Applied Physics **100**, 024108 (2006).
[153] A. Y. Borisevich *et al.*, Physical Review B **86** (2012).
[154] C. Merckling *et al.*, Applied Physics Letters **98**, 092901 (2011).
[155] S. D. Findlay *et al.*, Ultramicroscopy **111**, 285 (2011).
[156] A. M. Kolpak *et al.*, Physical Review Letters **105** (2010).
[157] R. Leapman, L. Grunes, and P. Fejes, Physical Review B **26**, 614 (1982).
[158] G. Radtke, and G. A. Botton, 2011), pp. 207.

[159] J. Buban, H. Iddir, and S. Öğüt, Physical Review B **69** (2004).
[160] A. Kuwabara, and I. Tanaka, J Phys Chem B **108**, 9168 (2004).
[161] A. M. Kolpak, and S. Ismail-Beigi, Physical Review B **85** (2012).

VITA

EDUCATION

2009-2013	Ph.D. in Physics, University of Illinois at Chicago, Chicago, IL
2011-2012	M.S. in Statistics, University of Illinois at Chicago, Chicago, IL
2007-2009	M.S. in Physics, University of Illinois at Chicago, Chicago, IL
2002-2006	B.S. in Physics, Nanjing University, Nanjing, China

RESEARCH EXPERIENCE

2012-2013	Molecular beam epitaxial growth and atomic-scale *in-situ* characterization of polarization and charge transfer at ferroelectric $BaTiO_3/SrTiO_3/GaAs$ interfaces, Research Assistant to Dr. Robert F Klie, University of Illinois at Chicago, in collaboration with Dr. Ravi Droopad, Texas State University
2010-2011	Investigating effects of substrate and doping on the crystallography of thermoelectric $Ca_3Co_4O_9$ thin films, Research Assistant to Dr. Robert F Klie, University of Illinois at Chicago
2009-2012	First-principles density functional theory calculations and 80 kV atomic-resolution STEM/EELS study on the $SrTiO_3/GaAs$ hetero-interfaces, Research Assistant to Dr. Robert F Klie and Dr. Serdar Ogut, University of Illinois at Chicago
2005-2007	Numerically studying the magnetization curves of superconducting $SmBa_2Cu_3O_{7-y}$ single crystals and Melt-textured Growth $YBa_2Cu_3O_{7-y}$ bulk based on nonlinear flux creep model simultaneously considering the effects of surface barrier and bulk pinning, Research Assistant to Dr. Shiying Ding, National Laboratory of Solid State Microstructures, Nanjing University

AWARDS

2013	Microscopy & Microanalysis Student Award to attend the Microscopy & Microanalysis Meeting in Indianapolis, IN
2012	M3S Student Travel Award to attend the Microscopy & Microanalysis Meeting in Phoenix, AZ
2011	M3S Student Travel Award to attend the Microscopy & Microanalysis Meeting in Nashville, TN
2010	MSA Student Travel Grant to attend the International Federation of Societies for Microscopy Congress in Rio de Janeiro, Brazil
2009	Scholarship to the 2010 Winter School on High Resolution Electron Microscopy in Tempe, AZ

PUBLICATIONS

- "Dynamical control of orbital ordering and ferroelectric-induced polar state in metallic manganites," H. Chen, Q. Qiao, A. Gulec, P.J. Phillips, R.F. Klie, M.S.J. Marshall, F.J. Walker, C.H. Ahn and S. Ismail-Beigi, *Physical Review Letters* (to be submitted)
- "Epitaxial Ferroelectric Oxides on Semiconductors - A route towards negative capacitance devices," R. Droopad, R. Contreras-Guerrero, Q. Qiao, R.F. Klie, J. Veazey, and J. Levy, *Microelectronic Engineering,* **109**, 290 (2013)
- "Observations of Co^{4+} in a Higher Spin State and the Increase in the Seebeck Coefficient of Thermoelectric $Ca_3Co_4O_9$," R.F. Klie, Q. Qiao, T. Paulauskas, A. Gulec, A. Rebola, S. Öğüt, M.P. Prange, J.C. Idrobo, S.T. Pantelides, S. Kolesnik, B. Dabrowski, M. Ozdemir, C. Boyraz, D. Mazumdar, and A. Gupta, *Physical Review Letters,* **108**, 196601 (2012)
- "Atomic and electronic structures of $SrTiO_3$/GaAs heterointerfaces: An 80-kV atomic-resolution electron energy-loss spectroscopy study," Q. Qiao, R.F. Klie, S. Öğüt, and J.C. Idrobo, *Physical Review B,* **85**, 165406 (2012)
- "Examining the structure and bonding in complex oxides using aberration-corrected imaging and spectroscopy," R.F. Klie, Q. Qiao, T. Paulauskas, Q. Ramasse, M.P. Oxley, and J.C. Idrobo, *Physical Review B,* **85**, 054106 (2012)
- "Effect of substrate on the atomic structure and physical properties of thermoelectric $Ca_3Co_4O_9$ thin films," Q. Qiao, A. Gulec, T. Paulauskas, S. Kolesnik, B. Dabrowski, M. Ozdemi, C. Boyraz, D. Mazumdar, A. Gupta and R.F. Klie, *Journal of Physics: Condensed Matter,* **23**, 305005 (2011)
- "Surface barrier and bulk pinning in MTG YBaCuO," L. Zhang, Q. Qiao, X.B. Xu, Y.L. Jiao, L. Xiao, S.Y. Ding, and X.L. Wang, *Physica C,* **445–448**, 236 (2006)
- "Surface barrier and bulk pinning in a $SmBa_2Cu_3O_{7-y}$ single crystal," L. Zhang, X.B. Xu, Q. Qiao, X. Yao, Q.H. Wang, and S.Y. Ding, *Superconductor Science and Technology,* **19**, S443 (2006)

CONFERENCE PRESENTATIONS

- "Atomic Resolution and First Principles Study of the Electronic Structure at $SrTiO_3$/GaAs Hetero-interfaces," Q. Qiao, R.F. Klie, S. Ogut, R. Droopad, R. Contreras-Guerrero, *APS March Meeting 2013*, Baltimore, MD, 2013
- "80 kV study of the Atomic Structure and Bonding at $SrTiO_3$/GaAs Hetero-interfaces," Q. Qiao, R.F. Klie, R. Contreras-Guerrero, R. Droopad, *Electronic Materials and Applications 2013*, Orlando, FL, 2013
- "Low kV Analysis of the Atomic Structure and Bonding at $SrTiO_3$/GaAs Hetero-interfaces," Q. Qiao, S. Ogut, R.F. Klie, *MRS Fall Meeting 2012*, Boston, MA, 2012 (poster)

- "80 kV Atomic Resolution Study of the Structure and Bonding at $SrTiO_3$/GaAs Hetero-interfaces," Q. Qiao, S. Ogut, R.F. Klie, R. Droopad, *Midwest Microscopy and Microanalysis Society 2012 Meeting*, Chicago, IL, 2012 (invited)
- "Low kV Analysis of the Atomic Structure and Bonding at Complex Oxide - Semiconductor Hetero-interfaces," Q. Qiao, S. Ogut, R.F. Klie, R. Droopad, *Microscopy & Microanalysis 2012 Meeting*, Phoenix, AZ, 2012
- "Low kV Atomic Resolution and First Principles Study of the Structure and Bonding at $SrTiO_3$/GaAs Hetero-interfaces," Q. Qiao, S. Ogut, R.F. Klie, *APS March Meeting 2012*, Boston, MA, 2012
- "Low kV Analysis and First Principles Study of the Structure and Bonding at $SrTiO_3$/GaAs Hetero-interfaces," Q. Qiao, S. Ogut, R.F. Klie, *Microscopy & Microanalysis 2011 Meeting*, Nashville, TN, 2011
- "Atomic Resolution and First Principles Study of the Structure and Bonding at $SrTiO_3$/GaAs Hetero-interfaces," Q. Qiao, J.C. Idrobo, S. Ogut, R.F. Klie, *APS March Meeting 2011*, Dallas, TX, 2011
- "Atomic and electronic structure of $SrTiO_3$/GaAs hetero-interfaces," Q. Qiao, J.C. Idrobo, S. Ogut, R.F. Klie, *MRS Fall Meeting*, Boston, MA, 2010 (poster)
- "Atomic and electronic structure of $SrTiO_3$/GaAs hetero-interfaces," Q. Qiao, J.C. Idrobo, S. Ogut, R.F. Klie, *17th International Microscopy Congress*, Rio de Janeiro, Brazil, 2010
- "Atomic and electronic structure of $SrTiO_3$/GaAs hetero-interfaces," Q. Qiao, W. Walkosz, S. Ogut, R.F. Klie, *Microscopy & Microanalysis 2010 Meeting*, Portland, OR, 2010
- "Atomic and electronic structure of $SrTiO_3$/GaAs hetero-interfaces," Q. Qiao, W. Walkosz, S. Ogut, R.F. Klie, *APS March Meeting 2010*, Portland, OR, 2010